Department of Physics and Astronomy
University of Heidelberg

Master Thesis in Physics
submitted by

Rodrigo Felipe Rosa-Medina Pimentel

born in Lima (Peru)

2018

Probing Long-Time Spin Dynamics in a ^{87}Rb Bose-Einstein Condensate

This master thesis has been carried out by
Rodrigo F. Rosa-Medina Pimentel
at the Kirchhoff-Intitute for Physics in Heidelberg
under the supervision of
Prof. Dr. Markus K. Oberthaler

Abstract

In this thesis we study long-time spin dynamics in the $F = 1$ hyperfine manifold of a ^{87}Rb Bose-Einstein condensate (BEC). The magnetic sub-levels constitute a spin-1 system with ferromagnetic interactions.

We initialize the system out of equilibrium and monitor the subsequent evolution employing a new readout scheme. Thereby we simultaneously measure two orthogonal spin directions and extract the transverse magnetization, which captures coherences between the individual sub-levels. The energy scale of the spin dependent interactions introduces a timescale around 500 ms. At comparable evolution times, we observe coherent oscillations compatible with the corresponding mean field predictions.

Furthermore, we investigate the dynamics for long evolution times up to ~ 15 s. In particular, we examine the impact of controlled heating of the condensate density. For settings with minimal heating, a significant transverse spin survives and the associated fluctuations are captured by Truncated Wigner simulations. In this case, the system retains long-term coherence and is mainly affected by dephasing of the internal dynamics. In contrast, for larger heating the transverse spin significantly decays and the late-time fluctuations are smaller. This indicates a distinct long-term evolution influenced by decoherence and a dissipative relaxation due to finite temperature effects.

Zusammenfassung

In dieser Arbeit untersuchen wir die Langzeitspindynamik innerhalb der $F = 1$ Hyperfeinmannigfaltigkeit eines ^{87}Rb Bose-Einstein-Kondensats. Die magnetischen Niveaus bilden ein Spin-1 System mit ferromagnetischen Wechselwirkungen.

Wir präparieren Nichtgleichgewichtszustände und untersuchen die nachfolgende Spindynamik mithilfe eines neuen Ausleseschemas. Damit messen wir gleichzeitig zwei orthogonale Spinrichtungen und extrahieren die transversale Magnetisierung. Diese beschreibt Kohärenzen zwischen den einzelnen magnetischen Niveaus. Die Energieskala der Spin abhängigen Wechselwirkungen definiert eine interne Zeitskala von ca. 500 ms. Bei vergleichbaren Entwicklungszeiten beobachten wir kohärente Oszillationen, die mit mean field Vorhersagen kompatibel sind.

Wir untersuchen dann die Langzeitdynamik bis ~ 15 s. Insbesondere analysieren wir den Einfluss von kontrolliertem Heizen der Kondensatdichte. Im Fall minimaler Aufheizung überlebt ein signifikanter transversaler Spin und die zugehörigen Fluktuationen sind vergleichbar mit trunkierten Wigner Simulationen. In diesem Fall behält das System Kohärenz und ist hauptsächlich durch Dephasierung der internen Dynamik bestimmt. Im Gegensatz dazu zerfällt im Fall erheblicher Aufheizung die transversale Magnetisierung signifikant schneller und die Fluktuationen sind kleiner. Dies weist auf ein durch Dekohärenz und dissipative Relaxation beeinflusstes Langzeitverhalten hin, welches wir Effekten der endlichen Temperatur zuschreiben.

Contents

Contents

1. Introduction

Quantum many-body systems out of equilibrium can be found over a widespread range of scales, from heavy-ion collisions in the LHC [Ber14] to quenched ultra cold atoms in tabletop experiments [Lan16]. One pivotal challenge is to determine under which conditions these systems can relax to stationary states, where relevant expectation values are captured by thermal ensembles [D'A16]. In this context, it is essential to discern whether the system is truly isolated and relaxes through its own dynamics or instead couples to the environment experiencing additional dissipative processes. Moreover, it is important to identify the relevant timescales for different stages of the evolution: First, the system is expected to evolve coherently. Later, it can start to 'lose memory' of the particulars of the initial configuration and display universal features. At even longer timescales, the system might eventually relax.

Since the first experimental realization of Bose-Einstein condensation [And95], ultra cold atoms have established themselves as a versatile platform to simulate the dynamics of many-body quantum systems, due to the high degree of experimental control and isolation from the environment [Blo12]. Non-equilibrium conditions are routinely accessed by tuning or quenching parameters of the underlying Hamiltonians.

We specifically work with a ^{87}Rb *spinor condensate*, where the internal magnetic sub-levels within the $F = 1$ hyperfine manifold constitute a many-body spin-1 system with ferromagnetic interactions. They introduce an *internal timescale* of $\sim 500\,\text{ms}$ and give rise to spin-mixing dynamics [SK13], which coherently redistribute atomic populations between the magnetic sub-levels.

At comparable times, this process drives non-linear dynamics evidenced by population oscillations [Cha05] for initial conditions prepared out of equilibrium. Moreover, parametric amplifications of quantum fluctuations can also spontaneously produce a macroscopic *transverse magnetization* in the presence of dynamic instabilities [Les09, Sch10]. This quantity captures coherences within the spin-1 BEC. Furthermore, if spatial degrees of freedom are accessible, such as in our quasi-1D condensate, even richer *non-equilibrium dynamics* can emerge after parametric quenches. A system in its ground state becomes dynamically unstable when quenched across a quantum phase transition and spatial spin excitations develop exponentially fast at short times [Prü16]. At *later stages*, correlation functions of the transverse spin are expected to become insensitive of the initial condition and exhibit scaling in time and space [Wil16]. This universal self-similar behavior has been indeed observed in our setup [Prü18] within a transient range of evolution times around $\sim 5\text{-}10\,\text{s}$.

Within similar timescales a significant decay of the transverse spin is appreciable, signalizing the progressive loss of coherences. This in turn limits the range of evolution times where scaling dynamics is experimentally accessible in our system. Hence, it is important to further characterize the late-time spin dynamics and assess whether *dissipative processes* such as atom loss or heating play a significant role.

In this thesis, we concentrate on studying and characterizing the spin dynamics in our BEC at long evolution times. For this purpose, we introduce a newly developed readout scheme which enables direct measurement of the full transverse spin. As a first application, we examine the short-time dynamics of this quantity and observe coherent oscillations reasonably captured by mean field predictions, complementing previous studies focusing on populations dynamics. Afterwards, we shift our focus to longer evolution times and systematically investigate finite temperature effects. In this context, we experimentally control and minimize the heating rate of the atomic density by adjusting the trapping configuration and develop diagnostic tools. We observe a significant impact on the long-term decoherence and overall behavior of the spin dynamics. To this end, we also compare the experimental results with Truncated Wigner simulations incorporating long-term dephasing effects.

Outline of this Thesis

This master thesis is structured in the following way:

- In *Chapter 2*, we introduce the required theoretical framework. We start by reviewing spin-1 systems, interacting spinor BECs and the associated coherent spin dynamics. Moreover, we present expressions for the density distributions of the thermal and condensate fractions at finite temperatures. These are employed later in order to diagnose heating in our system.

- In *Chapter 3*, we present our experimental platform. After providing an overview of the setup and the preparation sequences, we introduce a newly developed readout scheme. Thereby we measure two orthogonal spin directions in a single experimental run and directly extract the transverse magnetization.

- In *Chapter 4*, we study coherent spin dynamics. First, we present Truncated Wigner simulations (TW) incorporating long-term dephasing of the dynamics due to quantum fluctuations. Moreover, we experimentally examine the short-time evolution and observe coherent oscillations of the transverse spin for different initial conditions which are compatible with the theoretical predictions.

- Starting from *Chapter 5*, we focus on the late-time spin dynamics ($\sim 10\,\text{s}$). We observe a decay of the transverse spin indicating the progressive loss of coherences. Moreover, we examine the impact of finite temperature effects. The density heating rate is experimentally controlled by adjusting the trapping configuration and assessed from condensate fraction evolution. We observe a correlation between the heating rate and the late-time decoherence.

- Finally, in *Chapter 6* we further characterize the late-time spin dynamics examining the fluctuations of populations in the $m_F=0$ magnetic sub-level and the associated distributions: For settings with minimal heating, the long-term behavior is qualitatively captured by TW simulations and seems to primarily arise from dephasing of the internal dynamics. By contrast, settings with larger heating rates seem to undergo a diametrically different dissipative relaxation.

2. Spinor Bose-Einstein Condensates

In this introductory chapter we review basic theoretical notions about spin-1 Bose-Einstein condensates (BEC). We start by introducing spin-1 systems and presenting the observables required to characterize the system. Moreover, we discuss the central features of interacting spin-1 condensates and employ the single-mode approximation and a mean field treatment to understand the associated coherent spin dynamics. Finally, we discuss Bose-Einstein condensation at finite temperature and introduce expressions for density distribution of the condensate and thermal fractions. This distributions will be relevant in later chapters in order to characterize heating in our experimental system.

2.1. Spin-1 Systems

In our experiment we work with ^{87}Rb atoms within the hyperfine manifolds of the electronic ground state $5^2S_{1/2}$. The single valence electron of this alkali results in electronic spin $S = 1/2$ and zero orbital angular momentum $L = 0$, while the nuclear spin is $I = 3/2$. At small external magnetic fields, they couple and give rise to two hyperfine manifolds with $F = \{1, 2\}$. Specifically, we concentrate on studying the dynamics within the $F = 1$ manifold. The three magnetic sub-levels $|1, m_F\rangle$ with $m_F \in \{1, 0, -1\}$ constitute a *spin-1 system*. At a single-particle level, we can represent the wave function of such a system by a three component complex vector:

$$\Psi = \begin{pmatrix} \sqrt{\rho_1}e^{i\theta_1} \\ \sqrt{\rho_0}e^{i\theta_0} \\ \sqrt{\rho_{-1}}e^{i\theta_{-1}} \end{pmatrix} = e^{\theta_0} \begin{pmatrix} \sqrt{\rho_1}e^{i(\theta_s/2+\theta_L)} \\ \sqrt{\rho_0} \\ \sqrt{\rho_{-1}}e^{i(\theta_s/2-\theta_L)} \end{pmatrix} \tag{2.1}$$

where ρ_{m_F} and θ_{m_F} are the population and phase of the state $|1, m_F\rangle$. The wave function is further constrained by normalization to $1 = \rho_1 + \rho_0 + \rho_{-1}$. As we see in Eq (2.1), we can factorize θ_0 (global phase) and re-parametrize the state in terms of the so called *Larmor phase* $\theta_L = (\theta_1 - \theta_{-1})/2$ and a *spinor phase* $\theta_s = \theta_1 + \theta_{-1} - 2\theta_0$. While the former corresponds to the phase difference between $|1, 1\rangle$ and $|1, -1\rangle$, the latter captures the relative phase between the so called *side modes* $|1, \pm 1\rangle$ and the *central mode* $|1, 0\rangle$.

2.1.1. The Spin-1 Operators

In the textbook example of spin-$\frac{1}{2}$ systems [Sak95, Nol13] the spin-wave function can be represented by a complex two-component vector $\Psi_{1/2} = (\psi_\uparrow, \psi_\downarrow)^{\mathrm{T}}$. Moreover, the

2. Spinor Bose-Einstein Condensates

set of possible physical transformations acting on these states are contained in the so called SU(2) group. This group comprises the set of 2x2 complex unitary matrices which preserve the spin length and can be generated by the Pauli matrices $\hat{\sigma}_j$ with $j \in \{x, y, z\}$. These matrices can in turn be used to construct the *spin-$\frac{1}{2}$ operators* $\hat{S}_j = \hat{\sigma}_j/2$ which satisfy the commutation relation:

$$[\hat{S}_x, \hat{S}_y] = i\hat{S}_z \tag{2.2}$$

and all cyclic permutations thereof. We set $\hbar = 1$.

Since spin-1 states have an additional degree of freedom, the set of possible physical transformations is larger and contained in the so called SU(3) group comprising 3x3 complex unitary matrices. Here, we want to consider general spin states with N particles and employ the formalism of second quantization in order to introduce spin-1 operators for the $F = 1$ hyperfine manifold of a ^{87}Rb condensate. In this context, we define $\hat{\psi}_{m_{\mathrm{F}}}^\dagger$ ($\hat{\psi}_{m_{\mathrm{F}}}$) as the operator creating (annihilating) a particle in the $|1, m_{\mathrm{F}}\rangle$ mode of our system [1]. In this framework, the *spin-1 dipole operators* or spin directions are given by [Kaw12]:

$$\hat{F}_x = \frac{1}{\sqrt{2}}[\hat{\psi}_1^\dagger\hat{\psi}_0 + \hat{\psi}_0^\dagger\hat{\psi}_{-1}] + \text{h.c.} \tag{2.3}$$

$$\hat{F}_y = -\frac{i}{\sqrt{2}}[\hat{\psi}_1^\dagger\hat{\psi}_0 + \hat{\psi}_0^\dagger\hat{\psi}_{-1}] + \text{h.c.} \tag{2.4}$$

$$\hat{F}_z = \hat{\psi}_1^\dagger\hat{\psi}_1 - \hat{\psi}_{-1}^\dagger\hat{\psi}_{-1} = \hat{N}_1 - \hat{N}_{-1} \tag{2.5}$$

where $\hat{N}_{\pm 1} = \hat{\psi}_{\pm 1}^\dagger\hat{\psi}_{\pm 1}$ is the particle number operator counting the atoms in $|1, \pm 1\rangle$. In contrast to spin-$\frac{1}{2}$ systems, we require additional linearly independent operators to generate all relevant transformations. We can combine the spin dipole operators and obtain also the so called *spin-1 quadrupole operators*:

$$\hat{Q}_{ij} = \hat{F}_i\hat{F}_j + \hat{F}_j\hat{F}_i - \frac{4}{3}\delta_{i,j} \tag{2.6}$$

where $i, j \in \{x, y, z\}$ and $\delta_{j,k}$ is the Kronecker delta symbol. Moreover, we can construct linear combinations of these quadrupole operators as $\hat{Q}_{j^2-k^2} = (\hat{Q}_{ii} - \hat{Q}_{jj})/2$. A common choice of generators of the SU(3) group is given by the spin-dipole operators together with a selection of quadrupole operators and linear combinations thereof $\{\hat{F}_x, \hat{F}_y, \hat{F}_z, \hat{Q}_{xz}, \hat{Q}_{yz}, \hat{Q}_{xy}, \hat{Q}_{zz}, \hat{Q}_{x^2-y^2}, \hat{I}\}$ [Mar16]. Here, $\hat{I}$ is the identity operator. Representing the field operators as $\hat{\psi}_1^\dagger = (1, 0, 0)^T$, $\hat{\psi}_0^\dagger = (0, 1, 0)^T$ and $\hat{\psi}_{-1}^\dagger = (0, 0, 1)^T$, we can cast both the dipole and quadrupole operators:

---

[1] For clarity we implicitly assume the *single-mode approximation* (see subsection 2.2.2) and disregard spatial degrees of freedom. In the general case, the relevant field operators depend explicitly on the position in space, e.g. $\hat{\psi}_{m_{\mathrm{F}}}(\vec{x})$ with $\vec{x} \in \mathbb{R}^3$.

$$\hat{F}_x = \frac{1}{\sqrt{2}} \begin{pmatrix} 0 & 1 & 0 \\ 1 & 0 & 1 \\ 0 & 1 & 0 \end{pmatrix} \qquad \hat{F}_y = \frac{i}{\sqrt{2}} \begin{pmatrix} 0 & -1 & 0 \\ 1 & 0 & -1 \\ 0 & 1 & 0 \end{pmatrix} \qquad \hat{F}_z = \begin{pmatrix} 1 & 0 & 0 \\ 0 & 0 & 0 \\ 0 & 0 & -1 \end{pmatrix} \quad (2.7)$$

$$\hat{Q}_{yz} = \frac{i}{\sqrt{2}} \begin{pmatrix} 0 & -1 & 0 \\ 1 & 0 & 1 \\ 0 & -1 & 0 \end{pmatrix} \quad \hat{Q}_{xz} = \frac{1}{\sqrt{2}} \begin{pmatrix} 0 & 1 & 0 \\ 1 & 0 & -1 \\ 0 & -1 & 0 \end{pmatrix} \quad \hat{Q}_{xy} = \begin{pmatrix} 0 & 0 & -i \\ 0 & 0 & 0 \\ i & 0 & 0 \end{pmatrix} \quad (2.8)$$

$$\hat{Q}_{xx} = \frac{1}{3} \begin{pmatrix} -1 & 0 & 3 \\ 0 & 2 & 0 \\ 3 & 0 & -1 \end{pmatrix} \quad \hat{Q}_{yy} = \frac{1}{3} \begin{pmatrix} -1 & 0 & -3 \\ 0 & 2 & 0 \\ -3 & 0 & -1 \end{pmatrix} \quad \hat{Q}_{zz} = \frac{1}{3} \begin{pmatrix} 2 & 0 & 0 \\ 0 & -4 & 0 \\ 0 & 0 & 2 \end{pmatrix}$$

$$(2.9)$$

which we retrieve from [Hoa13].

2.2. Interacting Spinor Condensates

Spinor Bose-Einstein condensates are characterized by the fact that a group of internal magnetic sub-levels is accessible to the dynamics of the system. At low temperatures such as $T \lesssim 100\,\mathrm{nK}$ in our case and in the absence of permanent dipole moments, we can model the short-ranged interactions by two body s-wave scattering. Within this lowest partial wave approach, the relative orbital angular momentum of a pair of interacting spin-1 atoms vanishes ($L_{\mathrm{pair}} = 0$). Due to the underlying bosonic symmetry, the total spin $\hat{F}_{\mathrm{pair}} = \hat{F}_a + \hat{F}_b$ of a pair of interacting atoms $\{a, b\}$ can assume only even values $F_{\mathrm{pair}} \in \{0, 2\}$. Therefore, the total interaction potential is given as a sum over these two accessible scattering channels [Mar16]:

$$\hat{V}_{\mathrm{int}}(\vec{r}) = \sum_{F=0,2} \frac{4\pi\hbar^2}{m} a_F \hat{P}_F \delta(\vec{r}) = \frac{1}{2} \left[c_0 + c_1 \hat{F}_a \cdot \hat{F}_b \right] \delta(\vec{r}) \qquad (2.10)$$

where m is the mass of a single atom and $\vec{r}$ the relative coordinate between the particles. Here, a_F and $\hat{P}_F = \sum_{m_{\mathrm{F}}} |F, m_{\mathrm{F}},\rangle \langle F, m_{\mathrm{F}}|$ are the scattering length and projection operator in the $F \in \{0, 2\}$ scattering channel respectively. The interaction potential can be grouped in a spin independent term parametrized by $c_0 = \frac{4\pi\hbar^2(a_0+2a_2)}{3m}$ and a spin dependent one with $c_1 = \frac{4\pi\hbar^2(a_2-a_0)}{3m}$. For the $F{=}1$ manifold of ^{87}Rb the scattering lengths are on the order of $(a_0, a_2) \approx (101.8, 100.4)a_{\mathrm{B}}$, with Bohr radius a_{B} [Wid06]. In this case, the spin-spin interaction term is negative $c_1 < 0$ and favors the alignment of the spin of atom pairs (ferromagnetic interactions).

Considering this type of interactions and using the formalism of second quantization, we can write a general form for the Hamiltonian as described in [SK13].

$$\hat{H} = \int d\vec{r} \sum_{j=-1}^{1} \hat{\psi}_j^\dagger(\vec{r}) \left[-\frac{\hbar^2 \nabla^2}{2m} + V_{\mathrm{trap}}(\vec{r}) \right] \hat{\psi}_j(\vec{r}) + \int d\vec{r} : \left[\frac{c_0}{2} \hat{n}^2(\vec{r}) + \frac{c_1}{2} \sum_k \hat{F}_k^2(\vec{r}) \right] :$$

$$(2.11)$$

with $k = \{x, y, z\}$. The first two terms represent single-particle contributions arising from the kinetic energy and the external trapping potential. Meanwhile, the last two terms encode the density-density and spin-spin interactions in the system. The operator $\hat{n}(\vec{r}) = \sum_j \hat{\psi}_j^\dagger(\vec{r})\hat{\psi}_j(\vec{r})$ captures the total density operator at position $\vec{r} \in \mathbb{R}^3$ and $: [\,] :$ denotes normal ordering.

2.2.1. External Magnetic Fields

The experiments presented throughout this thesis are carried out in the presence of external magnetic fields which introduce energy shifts on the magnetic sub-levels $|1, m_F\rangle$. We define our quantization axis in z-direction and consider therefore fields in the form $\vec{B} = (0, 0, B_z)$. To second-order, this modifies the Hamiltonian in Eq.(2.11) by:

$$\hat{H}_B = \int d\vec{r}\, \hbar \left[p\hat{F}_z(\vec{r}) + q\left(1 - \hat{n}_0(\vec{r})\right) \right] \tag{2.12}$$

where the expressions $p = \mu_B g_F B_z/\hbar$ and $q = (g_{JI}\mu_B B_z)^2/(16\hbar E_{HFS})$ correspond to the energy splitting due to the first and second-order Zeeman shift for hyperfine energy spitting E_{HFS}. The constants μ_B, g_F and $g_{JI} = g_J - g_I$ are the Bohr magneton, the total Landé g-factor and the difference between the electronic and nuclear ones.

While the first-order Zeeman shift ($\propto \hat{F}_z$) introduces an energy splitting between the $|1, 1\rangle$ and $|1, -1\rangle$ magnetic sub-levels, the second-order shift ($\propto \hat{n}_0$) symmetrically shifts the central mode $|1, 0\rangle$ with respect to the side modes $|1, \pm 1\rangle$. The corresponding values for ^{87}Rb are introduced later in section 3.1.1.

2.2.2. The Single-Mode Approximation and Spin-Changing Collisions

Within the framework of this thesis, we want to focus on studying the dynamics associated with the internal spin degrees of freedom. The Hamiltonian presented in the previous section can in principle couple motional and spin degrees of freedom. If the spatial extension of the condensate is comparable or smaller than the spin-healing length $\zeta_s = 2\pi\hbar/\sqrt{2m|c_1|\bar{n}}$ [Pit03] (where $\bar{n}$ is the mean particle density), we expect that spatial spin-excitations are suppressed and can employ the *single-mode approximation* [Ham12]:

$$\hat{\psi}_j(\vec{r}) \approx \phi(\vec{r})\hat{\psi}_j \tag{2.13}$$

Here, we assume that all the atoms in the internal state $\hat{\psi}_j$ share the same normalized spatial wave function $\phi(\vec{r})$ with $\int d\vec{r}|\phi|^2 = 1$. Therefore, we can integrate out the motional degrees of freedom in Eqs.(2.11) and (2.12). This simplifies the Hamiltonian to a more compact expression depending exclusively on spin degrees of freedom. The single-mode Hamiltonian commutes with $\hat{F}_z$, such that the latter is a conserved quantity. Specifically, we want to concentrate on studying states with
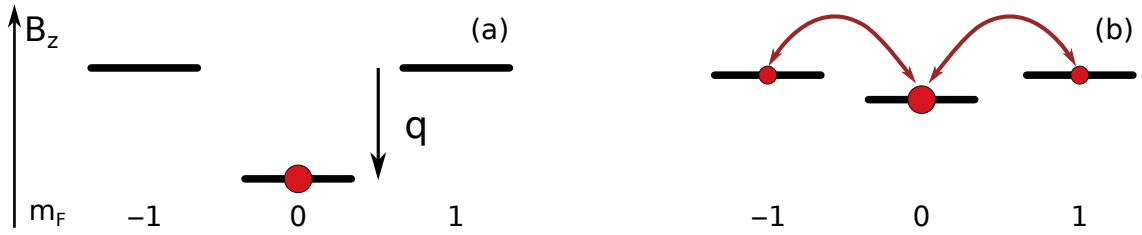
Figure 2.1.: **Internal dynamics in a ferromagnetic spin-1 BEC under an external magnetic field B_z (schematic representation)**. The second-order Zeeman shift introduces an energy shift q of the central mode $|1,0\rangle$ with respect to the side modes $|1, \pm 1\rangle$ **(a)**. If q is reduced and becomes comparable to the spin-spin interactions, *spin-changing collisions* take place **(b)**: Pairs of atoms in $|1,0\rangle$ collide and are coherently scattered into each one of the side modes and vice-versa. This process redistributes populations between the modes and facilitates the build up of a finite transverse magnetization. Since spin-mixing conserves the spin along the z-direction $\langle \hat{F}_z \rangle \propto N_1 - N_{-1} = $ constant, we can work a in a rotating frame and disregard the first-order Zeeman shift.

zero magnetization along the quantization axis $\langle \hat{F}_z \rangle = 0$. To this end, we transform into a *rotating frame* which co-precesses with p and disregard the first-order Zeeman shift [SK13]. The resulting single-mode Hamiltonian for a system with N atoms is:

$$\hat{H}_{\text{SM}} = \hbar \tilde{c}_1 \left[\hat{F}_x^2 + \hat{F}_y^2 \right] + \hbar q(N - \hat{N}_0) = \hbar \tilde{c}_1 \hat{F}_\perp^2 + \hbar q(N - \hat{N}_0) \tag{2.14}$$

where $\tilde{c}_1 = \frac{c_1}{2\hbar} \int d\vec{r} \, |\phi|^4$ is the single-mode spin-spin interaction parameter and $\hat{N}_0$ counts the number of particles in the central mode. We define the *transverse magnetization* as $\hat{F}_\perp^2 = \hat{F}_x^2 + \hat{F}_y^2$.

In the particular case of the ^{87}Rb ground state manifold $F = 1$, the spin-spin interactions are ferromagnetic ($\tilde{c}_1 < 0$) and favor the build up of transverse magnetization $\hat{F}_\perp$. Moreover, this part of the Hamiltonian also contains terms in the form $\hat{H}_{\text{SCC}} \propto \hat{\psi}_1^\dagger \hat{\psi}_{-1}^\dagger \hat{\psi}_0 \hat{\psi}_0 + $ h.c. which give rise to so called *spin-changing collisions* if the *detuning q* is sufficiently small. This is a coherent process by which pairs of atoms in the central mode are scattered into the side modes and vice-versa ($2 \times |1,0\rangle \leftrightarrow |1,1\rangle + |1,-1\rangle$). The relevant contributions and processes governing the internal dynamics in our spin-1 BEC are schematically represented in Fig.2.1.

2.2.3. Mean Field Equations of Motion

In our experiments we typically work withs $N \approx 10^4$ atoms. If the magnetic sublevels are macroscopically occupied, we can use a mean field ansatz. We substitute the field operators with complex order parameters or 'macroscopic wave functions' $\hat{\psi}_j^\dagger \rightarrow \sqrt{N_j} \zeta_j$ and $\hat{\psi}_j \rightarrow \sqrt{N_j} \zeta_j^*$, where N_j is the total number of atoms and $\rho_j = |\zeta_j|^2 = N_j/N$ are the normalized populations in $|1, j\rangle$.

From now on we want to concentrate exclusively on states with zero magnetization

along the z-direction $m = \langle\zeta|\hat{F}_z|\zeta\rangle = \rho_1 - \rho_{-1} = 0$. In this context, we introduce a normalized mean field spinor:

$$\zeta = \begin{pmatrix} \zeta_1 \\ \zeta_0 \\ \zeta_{-1} \end{pmatrix} = \begin{pmatrix} \sqrt{\frac{1-\rho_0}{2}}e^{i(\theta_s/2+\theta_L)} \\ \sqrt{\rho_0} \\ \sqrt{\frac{1-\rho_0}{2}}e^{i(\theta_s/2-\theta_L)} \end{pmatrix} \tag{2.15}$$

which is parametrized in terms of population in the central mode ρ_0, the spinor phase θ_s and the Larmor phase θ_L in resemblance to Eq.(2.1). Within this approximation, we introduce the mean field energy functional $\epsilon(\rho_0, \theta_s)$ which captures the average energy per particle and depends only on the central mode population and the spinor phase [Mar16]:

$$\epsilon(\rho_0, \theta_s) = \hbar\left[\lambda_1\rho_0(1-\rho_0)(1+\cos(\theta_s)) + q(1-\rho_0)\right] \tag{2.16}$$

where $\lambda_1 = 2N\tilde{c}_1$ is the *mean field spin-spin interaction* term. Within the Thomas-Fermi approximation, we expect this term to scale as $\lambda_1 \propto N \int d\vec{r}|\phi|^4 \propto N(n_0/N^{3/5}) = n_0 N^{2/5}$ with total atom number N and peak density of the condensate n_0 [Ham12]. Using standard variational techniques $\hbar\dot{\rho}_0 = -2\frac{d}{d\theta_s}\epsilon$ and $\hbar\dot{\theta}_s = 2\frac{d}{d\rho_0}\epsilon$, we obtain mean field equations of motion [Cha05]:

$$\dot{\rho}_0 = 2\lambda_1\rho_0(1-\rho_0)\sin(\theta_s)$$
$$\dot{\theta}_s = 2\lambda_1(1-2\rho_0)(1+\cos(\theta_s)) - 2q \tag{2.17}$$

For the sake of completeness, we also summarize the equations of motion for the individual components of the mean field spinor which we retrieve from [Hoa13]:

$$i\dot{\zeta_0} = \lambda_1[(\rho_1 + \rho_{-1})\zeta_0 + 2\zeta_1\zeta_{-1}\zeta_0^*] - q\zeta_0$$
$$i\dot{\zeta}_{\pm1} = \lambda_1\left[(\rho_{\pm1} + \rho_0 - \rho_{\mp1})\zeta_{\pm1} + \zeta_0^2\zeta_{\mp1}^*\right] \tag{2.18}$$

2.2.4. Visualizing the Spin Dynamics in Spin-Nematic Space

In this section, we introduce the so called spin-nematic sphere and employ it to graphically represent the internal spin dynamics arising from the non-linear equations of motion presented in Eq.(2.17).

SU(2)-Subspaces of SU(3)

The Bloch sphere constitutes a very useful visualization of the dynamics in spin-$\frac{1}{2}$ systems: Within this framework, one computes the expectation values of the three spin operators $\langle\hat{S}_x\rangle$, $\langle\hat{S}_y\rangle$ and $\langle\hat{S}_z\rangle$ and represents them together on the surface of a sphere, since they fulfill the commutation relation in Eq. $(2.2)^2$.

[2]This commutation relation defines the SU(2) group, which can be mapped into the SO(3) group of rotations in $\mathbb{R}^3$

A complete graphical representation of a spin-1 system is more elusive, since in principle we would need to simultaneously plot the expectation values of the eight spin operators which generate the SU(3) group. However, we can rely on spin-$\frac{1}{2}$ systems and choose triples of spin-1 operators which satisfy the SU(2) commutation relation $[\hat{O}_1, \hat{O}_2] = i\hat{O}_3$ in order to construct subspaces of SU(3).

A typical combination of triples is $\{\hat{F}_x, \hat{F}_y, \hat{F}_z\}$ and defines the so called *spin-1 sphere*. This sphere is suitable for representing spin-rotations induced by Hamiltonians of the form $\hat{H} \propto \hat{F}_j$ as we are going to see in the next chapter.

The so called *spin-nematic spheres* are formally defined by the combinations of operators $\{\hat{F}_y, \hat{Q}_{xz}, \hat{Q}_{xx} - \hat{Q}_{zz}\}$ or $\{\hat{F}_x, \hat{Q}_{yz}, \hat{Q}_{zz} - \hat{Q}_{yy}\}$ and are more relevant to represent the internal spin dynamics. If we consider a mean field spinor ζ with equal populations in each of the side modes and ignore the Larmor phase, we can approximate the expectation values as $\langle\zeta|\hat{Q}_{xx} - \hat{Q}_{zz}|\zeta\rangle \approx 2(2\rho_0 - 1)$ and $\langle\zeta|\hat{Q}_{zz} - \hat{Q}_{yy}|\zeta\rangle \approx -2(2\rho_0 - 1)$. Hence, we can construct two approximate SU(2)-subspaces in a similar fashion as in [Ham12]:

$$\{\hat{F}_x, \hat{Q}_{yz}, -2(2\hat{\rho}_0 - 1)\} \quad \text{and} \quad \{\hat{F}_y, \hat{Q}_{xz}, 2(2\hat{\rho}_0 - 1)\} \tag{2.19}$$

where the operator $\hat{\rho}_0$ yields the population in $|1, 0\rangle$.

A Geometric Spin-Nematic Sphere

Here, we want to combine the two subspaces introduced in Eq. (2.19) in order to construct a more useful geometric representation for the dynamics arising from the mean field equations of motion presented in Eq.(2.17). As previously stated, we restrict ourselves to states with zero magnetization along the quantization axis with $\rho_1 - \rho_{-1} = 0$ and compute the expectation values of the relevant operators:

$$\langle\zeta|\hat{F}_x|\zeta\rangle = 2\sqrt{\rho_0(1 - \rho_0)}\cos(\theta_s/2)\cos(\theta_L) = F_\perp \cos(\theta_L)$$
$$\langle\zeta|\hat{F}_y|\zeta\rangle = -F_\perp \sin(\theta_L)$$
$$\langle\zeta|\hat{Q}_{yz}|\zeta\rangle = -2\sqrt{\rho_0(1 - \rho_0)}\sin(\theta_s/2)\cos(\theta_L) = -Q_\perp \cos(\theta_L)$$
$$\langle\zeta|\hat{Q}_{xz}|\zeta\rangle = -Q_\perp \sin(\theta_L) \tag{2.20}$$

We define the average *transverse magnetization* as $F_\perp = 2\sqrt{\rho_0(1 - \rho_0)}\cos(\theta_s/2)$ and the associated quadrupole operator accordingly $Q_\perp = 2\sqrt{\rho_0(1 - \rho_0)}\sin(\theta_s/2)$. Using this representation, we directly see that $\langle\zeta|\hat{F}_x|\zeta\rangle$ and $\langle\zeta|\hat{F}_y|\zeta\rangle$ only differ by a term depending on the Larmor phase θ_L. Since the mean field energy functional does not depend on θ_L as we see in Eq.(2.16), the two approximate spin-nematic spaces in Eq.(2.19) are degenerate. Hence, we can combine these two subspaces and represent these expectation values together in a 'geometric' *spin-nematic sphere*:

$$\{F_\perp, Q_\perp, 2\rho_0 - 1\}. \tag{2.21}$$

where we closely follow the approach used in [Hoa13]. This particular choice has the practical advantage that the corresponding expectation values can be represented

together on the surface of a unit sphere as $F_\perp^2 + Q_\perp^2 + (2\rho_0 - 1)^2 = 1$. It is especially suitable for visualizing the spin-mixing dynamics in our system since the single-mode Hamiltonian depends explicitly on both the transverse spin $\hat{F}_\perp^2$ and the central mode population $\hat{N}_0$ or ρ_0 in a mean field treatment.

Visualization of the Spin Dynamics

The mean field trajectories on the spin-nematic sphere depend only on the ratio q/λ_1 since the explicit λ_1 dependence can be absorbed by re-parameterizing the time in Eq.(2.17). We solve the mean field equations of motion numerically[3] and obtain $(\rho_0(t), \theta_s(t))$ for different choices of q/λ_1 and initial conditions. We restrict ourselves to $\lambda_1 < 0$ in order to reproduce the ferromagnetic spin-spin interactions in the $F{=}1$ manifold of ^{87}Rb . We extract $\{F_\perp(t), Q_\perp(t), 2\rho_0(t) - 1\}$ following Eqs.(2.20) and plot the trajectories on the spin-nematic spheres in Fig.2.2.

If the second-order Zeeman shift is the dominant energy scale with $q/|\lambda_1| > 2$, the energy functional $\epsilon \approx \hbar q(1 - \rho_0)$ is minimized by a ground state where all atoms populate the $|1, 0\rangle$ mode such that $\rho_0 = 1$. This corresponds to a *fixpoint* of the dynamics at the north pole of the sphere (*polar phase*). If the system is initialized away from its ground state with $\rho_0 < 1$, the second-order Zeeman shift induces rotations around the $2\rho_0$-1 axis resulting in trajectories that explore a wide range of $F_\perp$ and $Q_\perp$ values. This open trajectories are equal energy contours with $\epsilon > 0$ and traverse phase space in mathematical positive direction.

As the second-order Zeeman shift is reduced and becomes comparable to the spin-spin interactions, a phase transition occurs at $q/|\lambda_1| = 2$. For $q/|\lambda_1| < 2$ the competition between these two terms gives rise to a mean field ground state with finite transverse magnetization $F_\perp \neq 0$ (*easy-plane ferromagnetic phase*). If the system is initialized close to the fixpoint it displays oscillations around this value which explore a limited range of phase space parameters. Moreover, a separatrix emerges in the system distinguishing between closed ($\epsilon < 0$) and open trajectories ($\epsilon > 0$). The latter are again dominated by a rotation around the $2\rho_0$-1 axis.

In the special case of $q = 0$, the dynamics is uniquely determined by the ferromagnetic spin-spin interactions. The Hamiltonian $\hat{H}_{SM} = \hbar\tilde{c}_1\hat{F}_\perp^2$ in Eq.(2.14) favors a fully magnetized ground state with $F_\perp = 1$ and $\rho_0 = 1/2$. This corresponds to a fixpoint on the equator of the spin-nematic sphere. Moreover, if the system is initialized away from the ground state the Hamiltonian gives rise only to closed trajectories circling the $F_\perp$-axis with $\epsilon < 0$.

---

[3]We use a MATLAB solver for ordinary differential equations ode45, which relies on a 5th order Runge-Kutta method.
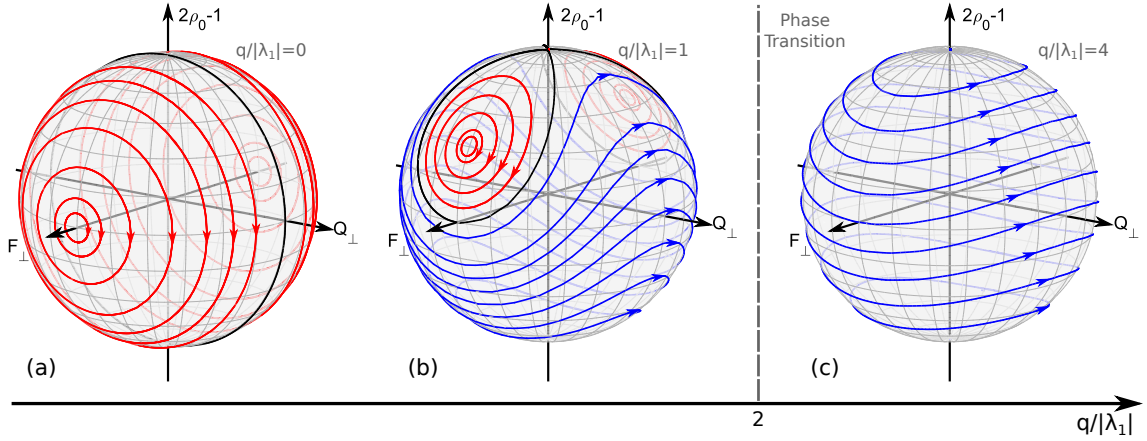
Figure 2.2.: **Mean field trajectories on the spin-nematic sphere for different ratios $q/|\lambda_1| = \{0, 1, 4\}$.** We consider ferromagnetic interactions $\lambda_1 < 0$ and plot the trajectories on the spin-nematic sphere. If the second-order Zeeman shift q is the dominant energy scale **(c)**, the ground state is located at the north pole of the sphere with $\rho_0 = 1$. Away from this fixpoint of the dynamics, the second-order Zeeman shift gives rise to rotations around the $2\rho_0$-1 axis resulting in positive energy contours $\epsilon > 0$ (blue curves), which explore a wide range of $F_\perp$ values. As q becomes comparable to $|\lambda_1|$, a phase transition occurs at $q/|\lambda_1| = 2$. For smaller ratios, a separatrix appears in the system (black line) distinguishing between closed (red) and open trajectories (blue curves) as shown in **(b)**. The direct competition between q and λ_1 results in a fixpoint with $F_\perp \neq 0$. In the limiting case of $q = 0$ **(a)**, the dynamics is solely determined by the spin-spin interactions which favor a fully magnetized ground state with $F_\perp{=}1$. When initialized away from this fixpoint, there are only closed trajectories with $\epsilon < 0$ (red curves) circling the $F_\perp$ axis.

2.3. Condensates at Finite Temperatures

So far, we have implicitly assumed zero temperature when discussing the coherent spin dynamics. As we want to study spin-mixing for $q/|\lambda_1| \sim 1$ and $|\lambda_1| \approx 2\pi \times 2\,\text{Hz}$ in our system, the relevant experimental timescales can extend up to few seconds. Within these long evolution times the system might be significantly affected by dissipative processes such as atom loss and heating. In this section, we discuss finite temperature effects and how they affect the density distribution of a condensate. Specifically, we present functional forms for the condensate and thermal fractions of an interacting BEC at finite temperatures. These are employed in later chapters to assess heating in our system.

2.3.1. Density Distribution of the Thermal and Condensate Fractions

In the $F{=}1$ manifold of ^{87}Rb , the density-density interactions are significantly larger than the spin-spin interactions with $|c_0/c_1| \approx 200$. Thus, we expect the former ones to primarily determine the density distribution of the atomic cloud. Throughout this section we consider therefore only the theoretical framework for a single component Bose gas without internal degrees of freedom. The repulsive interactions of the system are modeled via s-wave scattering with coupling constant $g = \frac{4\pi\hbar^2 a}{m}$ and scattering length $a > 0$. This approximation is justified, since our condensate is a dilute gas with diluteness parameter $na^3 \approx 10^{-5} \ll 1$. In accordance to our experimental setup, we consider radially symmetric harmonic confinement with frequencies $\omega_{||} = \omega_x$ and $\omega_\perp = \omega_z = \omega_y$. Using the Thomas-Fermi approximation, which neglects the kinetic energy of the condensate, one obtains the following expression for the density distribution of condensate n_{C} at $T = 0$ [Dal99, Pit03]:

$$
n_{\text{C}}(\vec{r}) = \left\{
\begin{array}{ll}
\frac{1}{g}\left[\mu - V_{\text{trap}}(\vec{r})\right] & \text{, for } V_{\text{trap}} < \mu \\
0 & \text{, otherwise}
\end{array}
\right.
\tag{2.22}
$$

where $V_{\text{trap}}(\vec{r}) = \frac{1}{2}m\omega_{||}^2 x^2 + \frac{1}{2}m\omega_\perp^2 r^2$ $(r^2 = y^2 + z^2)$ is the trapping potential of the system. The chemical potential μ is fixed by the total atom number N to:

$$
N = \int d\vec{r}\, n_{\text{C}}(\vec{r}) \;\Rightarrow\; \mu = \frac{\hbar\omega_{\text{HO}}}{2}\left(\frac{15Na}{a_{\text{HO}}}\right)^{2/5}
\tag{2.23}
$$

where $\omega_{\text{HO}} = (\omega_{||}\omega_\perp^2)^{1/3}$ is the geometric mean of the trapping frequencies and $a_{\text{HO}} = [\hbar/(m\omega_{\text{HO}})]^{1/2}$ is the harmonic oscillator length. We directly see in Eq.(2.22) that the condensate mimics the shape of the trapping potential and exhibits an inverted parabola extending in every spatial direction up to $\mu = \frac{1}{2}m\omega_\perp^2 R_\perp^2 = \frac{1}{2}m\omega_{||}^2 R_{||}^2$. This relation defines the *Thomas-Fermi radii* in longitudinal $R_{||}$ and transverse $R_\perp$ direction, which capture the spatial extension of the condensate. While the Thomas-Fermi approximation is strictly valid only at $T = 0$, it provides a good estimate at finite temperatures for macroscopic condensates with $N_{\text{C}}(T)a/a_{\text{HO}} >> 1$.

For finite temperatures T below the critical temperature T_C the condensate coexists with a cloud of non-condensed *thermal atoms*. The thermal atoms are effectively displaced towards outer trap regions due to the repulsive interactions with the significantly denser condensate which fills the central region of the trap. This behavior can be modeled by introducing an effective potential experienced by the thermal atoms [Dal99].

$$V_{\text{eff}}(\vec{r}) = \begin{cases} V_{\text{trap}}(\vec{r}) + 2gn_{\text{C}}(\vec{r}) & \text{, if } \frac{1}{2}m\omega_{\perp}^2 r^2 + \frac{1}{2}m\omega_{\|}^2 x^2 < \mu \\ V_{\text{trap}}(\vec{r}) & \text{, otherwise} \end{cases} \tag{2.24}$$

where the harmonic trapping potential V_{trap} is modified by a mean field term $2gn_{\text{C}}(\vec{r})$ inside the region shared with the condensate and the factor 2 accounts for the bosonic symmetry of the system. This approach disregards interactions between pairs of thermal atoms and the back-action of the thermal cloud on the condensate.

Using this effective potential and a standard grand-canonical approach we can write an expression for the density distribution of thermal atoms in real space:

$$n_{\text{T}}(\vec{r}) = \frac{1}{(2\pi\hbar)^3} \int d\vec{p} \frac{1}{e^{\beta(p^2/2m + V_{\text{eff}}(\vec{r}) - \mu)} - 1} = \lambda_T^{-3} g_{3/2}(e^{-\beta(V_{\text{eff}}(\vec{r}) - \mu)}) \tag{2.25}$$

where the integrand in the first term corresponds to the Bose-Einstein distribution and $\beta = 1/(k_B T)$ and k_B are the Boltzmann factor and constant respectively. The real space density distribution in the final term is obtained after integrating out the momentum coordinates and the thermal wavelength is defined as $\lambda_T = \sqrt{2\pi\hbar^2/(mk_B T)}$. The $g_{3/2}(z)$ function belongs to the class of generalized Riemann zeta functions $g_\gamma(z) = \sum_{k=1}^{\infty} z^k/k^\gamma$.

For an ideal Bose gas in the presence of harmonic trapping potentials, the critical temperature T_C and the condensate fraction N_C/N at finite temperature $T < T_C$ are given by [Ket99]:

$$T_C = \frac{\hbar\omega_{\text{HO}}}{k_B}\left(\frac{N}{\zeta(3)}\right)^{1/3} \approx 0.94\frac{\hbar\omega_{\text{HO}}}{k_B}N^{1/3} \tag{2.26}$$

$$\frac{N_C}{N} = 1 - \left(\frac{T}{T_C}\right)^3 \tag{2.27}$$

First-order corrections to the critical temperature due to interactions are given by $\Delta T_C/T_C = -1.3(a/a_{\text{HO}})N^{1/6}$ [Gio96]. For typical experimental parameters $N \approx 12000$ atoms, $(\omega_{\perp}, \omega_{\|}) \approx 2\pi \times (220, 46)\text{Hz}$ and $a \approx 100 a_B$ the relative correction is on the order of few percent $\Delta T_C/T_C \approx -0.033 = -3.3\%$ and therefore ignored within the scope of this thesis.

2.3.2. 1D Integrated Thermal and Condensate Profiles

In the experiment, we work with 1D density profiles which are integrated along the two directions (y, z) of tight confinement $\omega_{\perp}$. Therefore, we also need to integrate out

2. Spinor Bose-Einstein Condensates

the radial dependency of the condensate and thermal profiles to obtain distributions which we can compare to our experimental observations.

We consider first the *condensate profile* in Eq.(2.22) and introduce cylindric coordinates $(x, r) = (x, \sqrt{y^2 + z^2})$ to exploit the symmetry of the problem. Taking into account that the spatial extension of the condensate is fixed by the chemical potential $\frac{1}{2}m\omega_\perp^2 r^2 + \frac{1}{2}m\omega_\parallel^2 x^2 < \mu$, we can integrate out the radial dependence:

$$n_C^{1D}(x) = 2\pi \int_0^{R(x)} dr \, r \frac{1}{g}\left[\mu - \frac{1}{2}m\omega_\perp^2 r^2 - \frac{1}{2}m\omega_\parallel^2 x^2\right] = \frac{\pi}{gm\omega_\perp^2}\left[\mu - \frac{1}{2}m\omega_\parallel^2 x^2\right]^2$$

(2.28)

where $R(x) = \left[\frac{2\mu}{m\omega_\perp^2} - \frac{\omega_\parallel^2}{\omega_\perp^2}x^2\right]^{1/2}$ is the radial extension of the condensate at position x. We directly see that the 1D integrated profile of the condensate is captured by a fourth-oder polynomial instead of the inverted parabola in the 3D case.

For the computation of the 1D *thermal profiles*, we need to consider different functional forms for regions with and without overlap with the condensate cloud. Taking this into account, we integrate Eq.(2.25) and derive the final expression:

$$n_T^{1D}(x) = \frac{2\pi}{\lambda_T^3 m\beta\omega_\perp^2} \begin{cases} g_{5/2}\left(e^{-\beta(\frac{1}{2}m\omega_\parallel^2 x^2 - \mu)}\right) & , \text{if } x > R_\parallel = \sqrt{\frac{2\mu}{m\omega_\parallel^2}} \\ g_{5/2}\left(2 - e^{-\beta(\mu - \frac{1}{2}m\omega_\parallel^2 x^2)}\right) & , \text{otherwise} \end{cases}$$

(2.29)

with $g_{5/2}(z) = \sum_{k=1}^{\infty} z^k/k^{5/2}$. While outside the condensate region $(x > R_\parallel)$ the thermal atoms follow the trapping potential and exhibit a Gaussian profile $\propto \exp(-\beta(\frac{1}{2}m\omega_\parallel^2 x^2))$ to first-order, the repulsive interactions with the condensate result in an effective depletion of the thermal fraction when overlapping with the BEC as the leading term is $\propto 2 - \exp(-\beta(\mu - \frac{1}{2}m\omega_\parallel^2 x^2))$.

In order improve our intuitive understanding of these profiles, we plot them for representative experimental parameters $N = 12000$ atoms and trapping frequencies $(\omega_\perp, \omega_\parallel) = 2\pi \times (220, 46)$Hz in Fig.2.3. We choose temperatures $\{40, 60, 90, 110\}$nK below the critical temperature $T_C \approx 135$ nK and plot also the distribution of both the condensate and thermal components (dashed lines). We additionally integrate the density profiles within regions of $0.42\,\mu$m in longitudinal direction corresponding to the effective pixel size of our CCD camera, in order to have better comparability with the experiment. As we can directly see in the profiles, the Thomas-Fermi radius in longitudinal direction is on the order of $R_\parallel \approx 10\,\mu$m. For the two lowest temperatures displayed, the condensate fraction is large $N_C/N > 90\%$ and the profiles are dominated by the Thomas-Fermi shape of the BEC. As we increase the temperature and approach T_C, thermal wings become more predominant resulting in significantly reduced condensate fractions such as $N_C/N \approx 45\%$ for $T = 110$ nK.
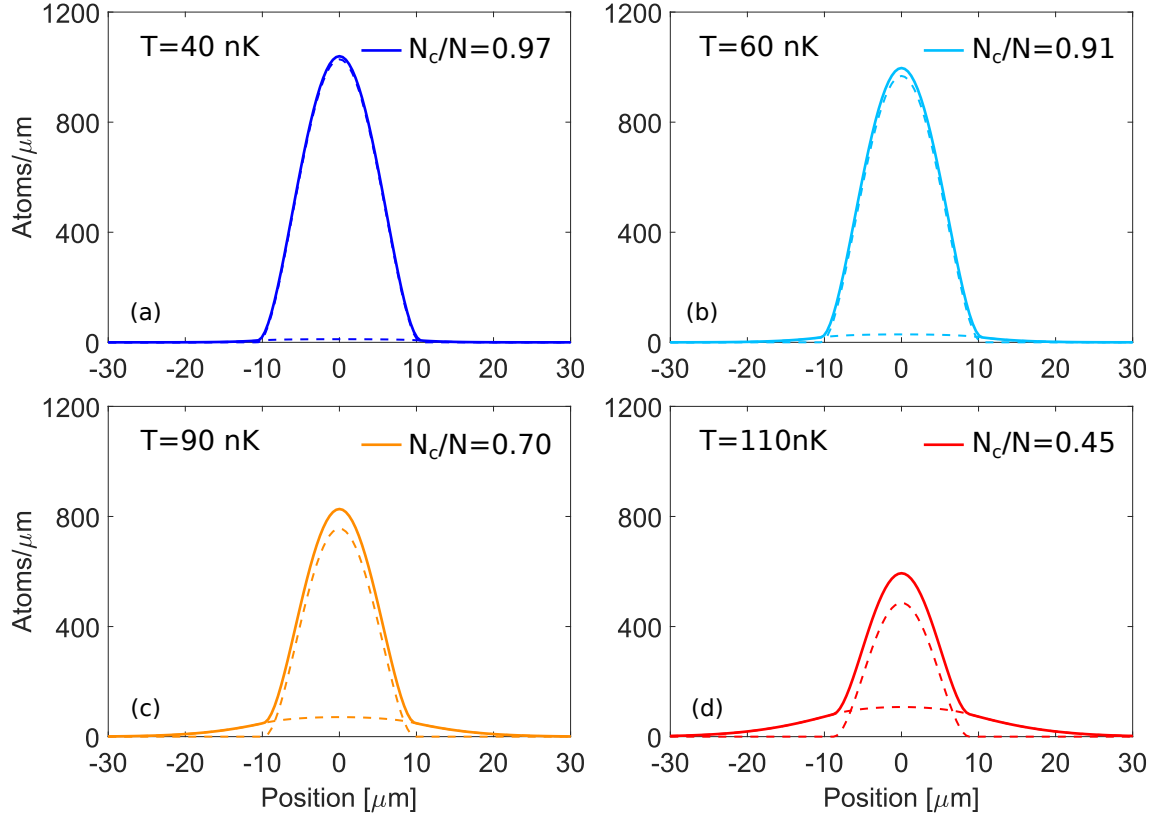
Figure 2.3.: **1D integrated profiles for different temperatures and experimental parameters N=12000 atoms, $(\omega_\perp, \omega_{||}) = 2\pi \times (220, 46)$Hz and critical temperature $T_C \approx 135$ nK.** We plot the 1D integrated profiles (solid lines) together with the thermal and condensate ones (dashed lines) for representative temperatures 40 nK **(a)**, 60 nK **(b)**, 90 nK **(c)** and 110 nK **(d)**. The Thomas-Fermi radius in longitudinal direction is around $R_{||} \approx 10$ µm. We clearly see that for low temperatures $T \leq 60$ nK the density profile is dominated by the condensate fraction as $N_C/N > 0.9$, while the thermal wings start to gain importance as the temperature is increased and approaches T_C.

3. Preparing and Probing a Spinor Condensate

In this chapter we present our experimental system. We start by providing a brief overview of the setup and discussing the level scheme of ^{87}Rb . Moreover, we also present a technique which we employ to prepare initial states with tunable transverse magnetization $F_\perp$. Afterwards, we describe in more detail a newly developed readout scheme which allows us to extract the two orthogonal directions of the transverse magnetization F_x and F_y in a single experimental run.

3.1. Overview of the Experimental System

3.1.1. Level Structure of ^{87}Rb

As previously stated, we perform experiments with ^{87}Rb atoms within the hyperfine manifolds of the electronic ground state. In the limit of small external fields, two manifolds $F = \{1, 2\}$ are in principle available and separated by the hyperfine splitting $E_{\text{HFS}} \approx h \times 6.835\,\text{GHz}$. In the presence of an external magnetic field $\vec{B} = (0, 0, B_z)$, the magnetic sub-levels $|F, m_F\rangle$ exhibit a first-order Zeeman splitting given by $p = g_F \mu_B m_F B_z / \hbar$ where μ_B is the Bohr magneton and $g_F \approx \{-\frac{1}{2}, \frac{1}{2}\}$ are the approximate Landé g-factors in $F = \{1, 2\}$. The splittings in the two manifolds $p_1/B_z \approx -2\pi \times 702.4\,\frac{\text{kHz}}{\text{G}}$ ($F{=}1$) and $p_2/B_z \approx 2\pi \times 699.6\,\frac{\text{kHz}}{\text{G}}$ ($F = 2$) are similar in magnitude but have opposite signs as we see in the sketch in Fig.3.1. This is going to be crucial to selectively address only the atoms in $F{=}1$ with radio frequency rotations and will enable our F_x-F_y readout scheme (see section 3.3.2).

As we know from the previous chapter, the second-order Zeeman shift directly determines the detuning of the spin-mixing dynamics in $F{=}1$ since we can transform into a rotating frame and disregard the first-order splitting. As also represented in Fig.3.1, it symmetrically shifts the central mode $|1, 0\rangle$ with respect to the side modes $|1, \pm 1\rangle$ by $q = (g_J - g_I)^2 \mu_B^2 B_z^2 / (16\hbar E_{\text{HFS}}) \approx 2\pi \times 72\,\frac{\text{Hz}}{\text{G}^2} B_z^2$. Here, $g_J \approx 2$ and $g_I \approx -0.001$ are the fine structure and nuclear g-factors [Ste01].

3.1.2. Experimental Setup

We start our experimental sequence by loading a ^{87}Rb atomic sample in a 3D magneto-optical trap (MOT) from a 2D MOT. Afterwards, the atoms are optically pumped to the $F{=}1$ manifold and transfered to a magnetic trap which only confines atoms in the $|1, -1\rangle$ internal state. When the radius of this time-orbiting potential is reduced, the hotter atoms at the edge of the trap can escape resulting in a first stage of forced evaporation. The atoms are then transfered to a crossed beam optical

dipole trap derived form a Yb:YAG laser with wavelength $\lambda \approx 1030\,\mathrm{nm}$, which is far red-detuned with respect to the $^{87}\mathrm{Rb}$ $D_{1,2}$-doublet at $\lambda \approx (795, 780)\mathrm{nm}$. As the optical trapping depth is reduced, a second stage of evaporative cooling takes place. We thereby reduce the temperature of atomic cloud below the critical temperature and obtain a spin polarized Bose-Einstein condensate of $\sim 10^4$ atoms in the $|1, -1\rangle$ magnetic sub-level. The duty cycle of the experiment is on the order of $\sim 40\,\mathrm{s}$.

We can carry out experiments with two different trapping configurations: We can work in a *crossed beam dipole trap* (see Fig.3.2(a)), which gives rise to tightly confined condensates and harmonic trapping frequencies on the order of $(\omega_\perp, \omega_{||}) \approx 2\pi \times (220, 46)\mathrm{Hz}$ with $\omega_\perp = \omega_{y,z}$ and $\omega_{||} = \omega_x$. As we are going to see in later chapters, this trapping configuration is suitable to study spin dynamics within the single-mode approximation. Alternatively, we can adiabatically switch-off the vertical trap arm and allow the atoms to expand in the remaining *waveguide trap* (see Fig.3.2(b)). This results in an elongated condensate with trapping frequencies $(\omega_\perp, \omega_{||}) \approx 2\pi \times (220, 2.2)\mathrm{Hz}$, suitable for investigating 1D spin dynamics [Prü18].

Experimental Control of q

As discussed before, spin-mixing is controlled by the energy difference between the central and side modes. We work at fixed magnetic offset field $B_z = 0.884\,\mathrm{G}$ which results in a second-order Zeeman shift around $q_\mathrm{B} \approx 2\pi \times 56.2\,\mathrm{Hz}$. We tune q by applying microwave radiation blue-detuned with respect to the $|1, 0\rangle \leftrightarrow |2, 0\rangle$ transition. The induced AC-Stark shift shifts $|1, 0\rangle$ by $q_\mathrm{AC} = -\frac{\Omega^2}{4\delta}$ [Ger06], such that:

$$q = q_\mathrm{B} + q_\mathrm{AC} = 2\pi \times 56.2\mathrm{Hz} - \frac{\Omega^2}{4\delta} \tag{3.1}$$

The Rabi frequency is around $\Omega \approx 2\pi \times 6\,\mathrm{kHz}$. We adjust the detuning δ in order to experimentally control q. The employed detuning values are substantially larger than the Rabi frequency with $\delta \approx 2\pi \times 150\,\mathrm{kHz}$, such that population transfer to $|2, 0\rangle$ is suppressed. Due to power stabilization of the microwave dressing, the relative fluctuations of q are small and on the order of $\Delta q / q_B \approx 0.4\%$ [Kun18b].

State Selective Imaging

After a period of evolution t_evo, the atomic sample is destructively probed by means of high-intensity absorption imaging. A Stern-Gerlach pulse along the z-direction is applied beforehand in order to spatially separate the different hyperfine components $|F, m_F\rangle$ after a short free time of flight expansion $\sim 1\mathrm{ms}$. The populations in the $F{=}1$ and $F{=}2$ manifolds can be distinguished in a two-step process: First, only the imaging beam in switched on for about $15\,\mathrm{\mu s}$ ($\lambda = 780.2\mathrm{nm}$). This resonantly addresses the $^2S_{\frac{1}{2}}$ $F{=}2 \rightarrow {}^2P_{\frac{3}{2}}$ $F'{=}3$ transition, images the atoms in $F{=}2$ and displaces them out of the trap. Afterwards, the re-pumper laser is combined with the imaging beam in order to resonantly address the atoms in the $F{=}1$ manifold ($F{=}1 \rightarrow F'{=}2$). After recording reference and dark pictures, we can extract the atom number per pixel in each of the $|F, m_F\rangle$ sub-levels of both manifolds [Mü14].

More details concerning the experimental setup can be found in the supplementary materials of [Kun18b, Prü18] as well as in [Str16, Lin17].
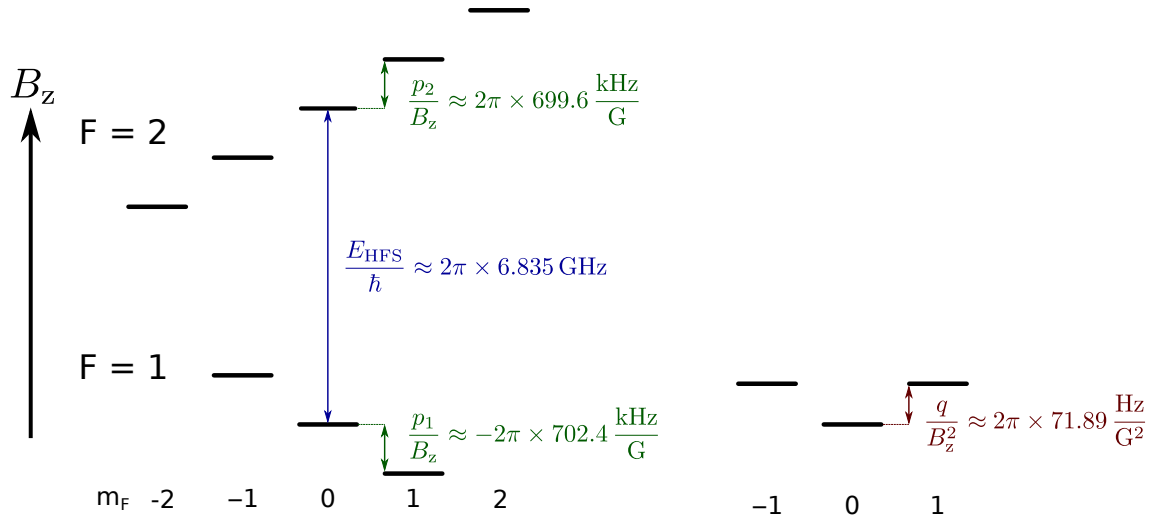
Figure 3.1.: **^{87}Rb level scheme.** At low external fields B_z, the electronic ground state of ^{87}Rb consists of two hyperfine manifolds $F = \{1, 2\}$ separated by E_{HFS} **(left)**. The first-order Zeeman splitting is on the order of $\sim 2\pi \times 700 \frac{\text{Hz}}{\text{G}} B_z$ but in opposite direction for $F = \{1, 2\}$ due to the different sign of the Landé g-factors $g \approx \{-\frac{1}{2}, \frac{1}{2}\}$. The second-order Zeeman splitting in $F = 1$ **(right)** introduces a shift between $|1, 0\rangle$ and the side modes $|1, \pm 1\rangle$. The values are retrieved from [Ste01].
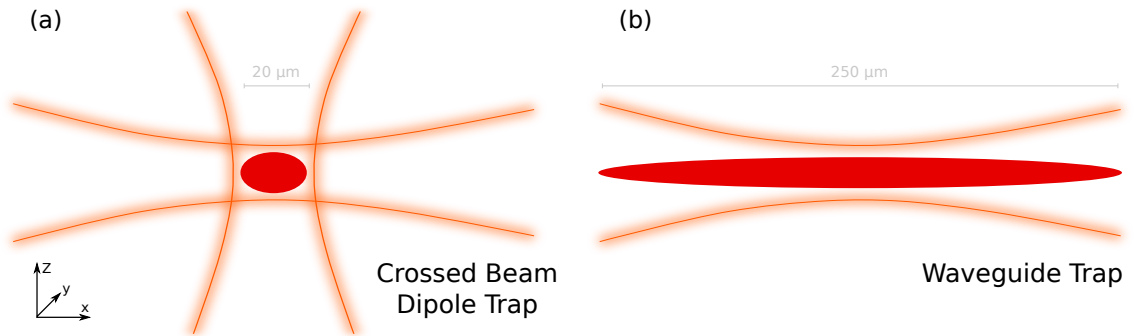
Figure 3.2.: **Trapping configurations**. We can perform experiments directly in a *crossed beam dipole trap* **(a)** and work with tightly confined condensates experiencing trapping frequencies around $(\omega_\perp, \omega_{||}) \approx 2\pi \times (220, 46)$ Hz with $\omega_\perp = \omega_{y,z}$. This configuration is suitable to study single-mode spin dynamics. Alternatively, we can adiabatically switch-off the vertical trapping arm and let the atoms expand in the remaining *waveguide trap* **(b)**. The resulting elongated BEC with $(\omega_\perp, \omega_{||}) \approx 2\pi \times (220, 2.2)$ Hz is appropriate for investigating 1D spin-1 physics.

3.2. Preparation of Initial States with Tunable $F_\perp$

In this section, we present a procedure to prepare initial states with tunable transverse magnetization $F_\perp$. A detailed discussion of the preparation of different initial conditions in our spin-1 ^{87}Rb condensate can be found in [Lan18].

We start by applying two successive resonant microwave (MW) π-pulses in order to transfer all the atomic population to the polar state $|1, -1\rangle \rightarrow |2, 0\rangle \rightarrow |1, 0\rangle$. The resulting state can be represented by the normalized spinor $\psi = (0, 1, 0)^T$. Afterwards, we apply a radio frequency (RF) pulse resonant with the first-order Zeeman splitting in $F = 1$, which couples the individual magnetic sub-levels. The action of the RF pulse can be modeled by the Hamiltonian $\hat{H}_{\mathrm{RF}} = \hbar\Omega_{\mathrm{RF}}\hat{F}_x$, with Rabi frequency around $\Omega_{\mathrm{RF}} \approx 2\pi \times 3\,\mathrm{kHz}$. The employed ϕ_{RF}-pulse transfers atomic populations to the side modes and rotates the polar to a 'tilted polar'. The phase $\phi_{\mathrm{RF}} = \Omega_{\mathrm{RF}}t_{\mathrm{RF}}$ is controlled by the pulse time t_{RF}.

The resulting state evolves then for t_s under the influence of the second-order Zeeman shift $q = q_{\mathrm{B}} = 2\pi \times 56.2\,\mathrm{Hz}$. This process is captured by the Hamiltonian $\hat{H}_s = \hbar\frac{q}{2}\hat{Q}_{\mathrm{zz}} = \hbar q(\frac{1}{3} - \hat{\rho}_0)$, where the operator $\hat{\rho}_0 = \frac{1}{N}\hat{\psi}_0^\dagger\hat{\psi}_0$ counts the population in $|1, 0\rangle$ [Lan18]. This Hamiltonian introduces a relative phase between central mode and the side modes $\Delta\theta = -qt_s$ and modifies thereby also the spinor phase $\theta_s = \frac{\pi}{2} - 2\Delta\theta = \frac{\pi}{2} - 2qt_s$. We choose $t_s = \frac{\pi}{4q} \approx 4.4\,\mathrm{ms}$ of evolution to enforce $\theta_s = 0$ spinor phase, such that $F_\perp$ becomes maximal for the corresponding central mode population ρ_0 as we see in Eq.(2.20). We obtain the following expectation values for the two directions of the transverse spin while tuning the duration of the RF-pulse:

$$\langle\psi'|\hat{F}_x|\psi'\rangle = -\sin(2\phi_{\mathrm{RF}}) \quad \mathrm{and} \quad \langle\psi'|\hat{F}_y|\psi'\rangle = 0 \tag{3.2}$$

with $|\psi'\rangle = \exp(-i\frac{\pi}{4}\hat{Q}_{\mathrm{zz}})\exp(-i\phi_{\mathrm{RF}}\hat{F}_{\mathrm{x}})|\psi\rangle$. Hence, the magnitude of the initial transverse spin can be adjusted by controlling the duration of the initial RF-pulse and is $|F_\perp| = |\sin(2\Omega_{\mathrm{RF}}t_{\mathrm{RF}})|$.

3.3. Simultaneous Readout of F_x and F_y

In this section, we present a newly developed readout scheme which allows us to extract two orthogonal directions of the transverse magnetization F_x and F_y in a single experimental run. In contrast to other existing techniques such as 'absorptive spin-sensitive in-situ imaging' (ASSISI) [Mar16] which employ multiple imaging pulses, we rely on state selective radio frequency rotations and on using the $F = 2$ manifold as a storage platform for one of the probed spin directions.

3.3.1. F_x-F_y Readout Scheme: Motivation and Description

Throughout this section, we consider a normalized mean field spinor:

$$\psi = \frac{1}{\sqrt{N}}(\sqrt{N_1}e^{i\theta_1}, \sqrt{N_0}e^{i\theta_0}, \sqrt{N_{-1}}e^{i\theta_{-1}})^T \tag{3.3}$$

where N_{m_F} and θ_{m_F} are the number of atoms and phases of the $|1, m_F\rangle$ magnetic sub-level. As discussed in the previous section, we can extract the atomic population in the individual sub-levels by applying a Stern-Gerlach pulse before imaging. In this way, we can readily extract the magnetization along the quantization axis using Eq.(2.9):

$$\langle \hat{F}_z \rangle = \langle \psi | \hat{F}_z | \psi \rangle = \frac{1}{N} \left[N_1 - N_{-1} \right] \tag{3.4}$$

This observable is directly accessible by measuring populations and computing the particle number imbalance between atoms in the side modes $\propto N_1 - N_{-1}$. However, we are rather interested in studying spin-mixing dynamics for states with $\langle \hat{F}_z \rangle = 0$ but finite transverse magnetization $F_\perp$. In order to obtain this quantity, we want to measure the spin along the x and y-directions which are given by:

$$\langle \hat{F}_x \rangle = \frac{\sqrt{2}}{N} \left[\sqrt{N_1 N_0} \cos(\Delta\theta_1) + \sqrt{N_{-1} N_0} \cos(\Delta\theta_{-1}) \right]$$
$$\langle \hat{F}_y \rangle = -\frac{\sqrt{2}}{N} \left[\sqrt{N_1 N_0} \sin(\Delta\theta_1) - \sqrt{N_{-1} N_0} \sin(\Delta\theta_{-1}) \right] \tag{3.5}$$

with relative phases $\Delta\theta_{\pm 1} = \theta_{\pm 1} - \theta_0$. Hence, these quantities capture phase *coherences* between the central mode and the side modes of the system and are not directly experimentally accessible by measuring atom numbers in the hyperfine manifolds. We will employ radio frequency pulses to map F_x and F_y into the accessible readout axis F_z. The employed radio frequency pulses are generated by time dependent B-fields which oscillate in the x-y plane with phase ϕ. We choose the oscillation frequency $\omega = |p| \approx 2\pi \times 621\,\text{kHz}$ to match the first-order Zeeman splitting in $F{=}1$ and resonantly address the atoms. Transforming into the rotating frame of the atoms, we obtain the effective Hamiltonian [Per13]:

$$\hat{H}_{\text{RF}} = -\hbar\Omega_{\text{RF}} \left[\cos(\phi)\hat{F}_x - \sin(\phi)\hat{F}_y \right] \tag{3.6}$$

with Rabi frequency $\Omega_{\text{RF}} = |g_1|\mu_{\text{B}}B/\hbar$. Its effect on spin-1 states can be graphically represented on the *spin-1 sphere*, where we represent the expectation values of the three spin directions $\{F_x = \langle \hat{F}_x \rangle, F_y = \langle \hat{F}_y \rangle, F_z = \langle \hat{F}_z \rangle\}$. On this sphere, the RF-pulses generate rotations around the $F_x \cos(\phi) + F_y \sin(\phi)$ axis where the phase ϕ corresponds to the polar angle in the spin-1 sphere. Experimentally, we adjust only relative phases between the different RF pulses and are free to define F_y as the axis for the first RF-rotation.

The Readout Scheme

We start by applying a first $\frac{\pi}{2}$-RF pulse in order to rotate the spin state around the F_y-axis and effectively map $\langle \hat{F}_x \rangle$ into the F_z-axis:

3. Preparing and Probing a Spinor Condensate

$$\langle\psi|\hat{F}_x|\psi\rangle = \langle\exp\left(-i\frac{\pi}{2}\hat{F}_y\right)\psi|\hat{F}_z|\exp\left(-i\frac{\pi}{2}\hat{F}_x\right)\psi\rangle = \frac{1}{N}\left[N_1' - N_{-1}'\right] \qquad (3.7)$$

where we define the phase of the first pulse to be $\phi_1 = \frac{\pi}{2}$ in order to enforce rotations with the Hamiltonian $\hat{H}_{\mathrm{RF},1} = \Omega_{\mathrm{RF}}\hat{F}_y$. We can extract then $\langle\hat{F}_x\rangle$ by measuring population differences between the side modes $N_1' - N_{-1}'$ after the RF-rotation.

Afterwards, we transfer half of the atomic populations to different magnetic sublevels of the $F=2$ manifold by applying three successive resonant microwave $\frac{\pi}{2}$-pulses $|1,-1\rangle \rightarrow |2,-2\rangle$, $|1,0\rangle \rightarrow |2,0\rangle$ and $|1,1\rangle \rightarrow |2,2\rangle$. This allows us to use the $F=2$ manifold as a storage platform for shelving $\langle\hat{F}_x\rangle$.

Finally, we apply a second $\frac{\pi}{2}$-RF pulse phase shifted by $\frac{\pi}{2}$ with respect to the first one ($\phi_2 = \phi_1 + \frac{\pi}{2}$). The resulting Hamiltonian $\hat{H}_{\mathrm{RF},2} = \Omega_{\mathrm{RF}}\hat{F}_x$ generates rotations around the F_x-axis in the spin-1 sphere. We selectively address only the atoms in $F = 1$ with an RF $\frac{\pi}{2}$-pulse leaving the atoms in $F = 2$ unaffected (see section 3.3.2). Thereby we effectively map $\langle\hat{F}_y\rangle$ into the $\hat{F}_z$-axis:

$$\langle\psi|\hat{F}_y|\psi\rangle = \langle\exp\left(-i\frac{\pi}{2}\hat{F}_x\right)\exp\left(-i\frac{\pi}{2}\hat{F}_y\right)\psi|\hat{F}_z|\exp\left(-i\frac{\pi}{2}\hat{F}_x\right)\exp\left(-i\frac{\pi}{2}\hat{F}_y\right)\psi\rangle$$
$$= \frac{1}{N}\left[N_1'' - N_{-1}''\right] \qquad (3.8)$$

and can extract this quantity from imbalance between the side modes after the two RF-rotations $N_1'' - N_{-1}''$.

Hence, we can extract $\langle\hat{F}_x\rangle$ and $\langle\hat{F}_y\rangle$ in a single experimental run by measuring normalized atom number differences in the side modes of $F = 2$ and $F = 1$ respectively after the corresponding RF-rotations. These quantities can be obtained employing our state selective absorption imaging setup.

The employed pulse sequence is represented in Fig.3.3(a) together with a schematic visualization of the readout scheme using spin-1 spheres in Fig.3.3(b).

3.3.2. Selective Rotations in F=1

So far we have presented the F_x-F_y readout schematically and assumed that we can address the atoms in $F = 1$ without inducing RF-rotations on the state stored in $F = 2$. This is a priori not trivial, since for $B_z = 0.884\,\mathrm{G}$ the difference between the first-order Zeeman splittings in the two manifolds $\delta = |p_2| - |p_1| \approx -2\pi \times 2.5\,\mathrm{kHz}$ is smaller than the typical values for the RF-Rabi frequency $\Omega_{\mathrm{RF}} \approx 2\pi \times 10\,\mathrm{kHz}$.

Selective rotations in $F = 1$ are indeed possible by combining the time-dependent magnetic fields of *two orthogonal coils* which are sketched in Fig.3.4(a). For illustrative purposes, we assume that the Zeeman splitting in $F = \{1, 2\}$ is equal in magnitude $\delta = 0$ and that the fields are homogeneous within the spatial extension of the BEC. Moreover, we assume that the coils produce two perfectly orthogonal linearly polarized fields in the x-y plane which oscillate with $\omega = |p_1| \approx 2\pi \times 621\,\mathrm{kHz}$, equal maximal amplitude B and relative phase ϕ_{c}. Considering also the offset field $B_z = 0.884\,\mathrm{G}$, the total magnetic field is given by:
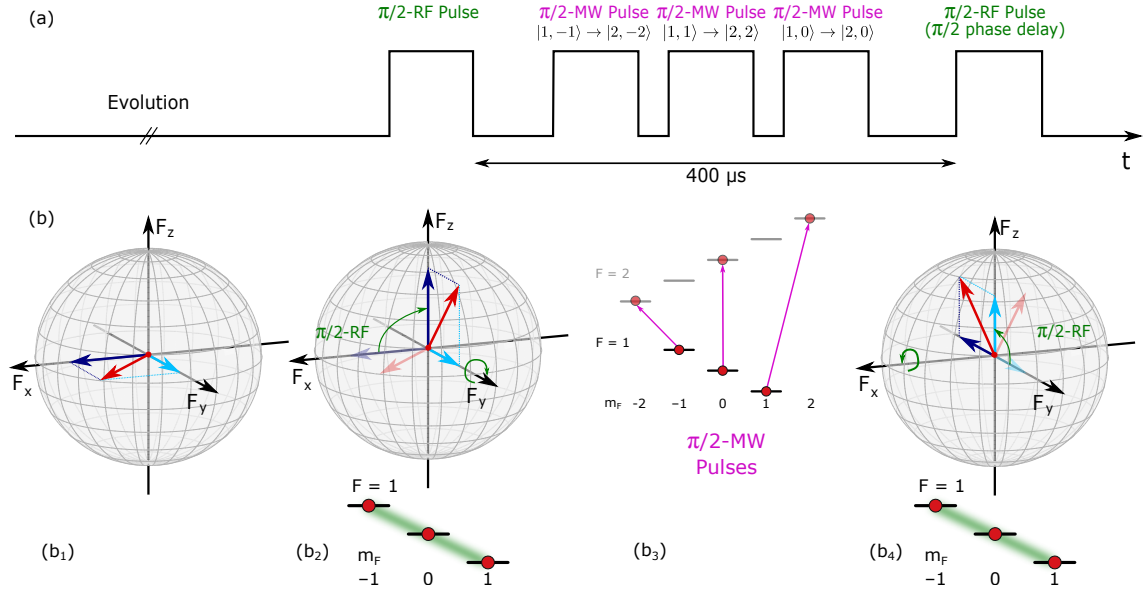
Figure 3.3.: **Pulse sequence (a) and schematic representation (b) of F_x-F_y readout scheme.** We extract two orthogonal directions F_x (blue) and F_y (light blue) of the transverse spin (red arrow) in a single experimental run and employ spin-1 spheres for visualization (b_1). We start the sequence by applying a first RF $\frac{\pi}{2}$-pulse (green arrow) which couples the magnetic sub-levels in $F = 1$ and maps F_x into F_z (b_2). Afterwards, we apply three successive resonant microwave $\frac{\pi}{2}$-pulses in order to transfer half of the atomic populations to different magnetic sub-levels in $F = 2$ (b_3). Thereby, we shelve F_x in $F = 2$. Finally, we apply a second RF $\frac{\pi}{2}$-pulse which is phase shifted by $\frac{\pi}{2}$ with respect to the first one and address the atoms in $F = 1$ selectively (b_4). This rotates the state around the F_x-axis and maps F_y into the readout axis F_z. Thus, we extract $\{F_y, F_x\}$ in $F = \{1, 2\}$ as population differences between the side modes.

3. Preparing and Probing a Spinor Condensate

$$\vec{B} = (B\cos(\omega t), B\cos(\omega t + \phi_c), B_z) \tag{3.9}$$

We represent this field in a spherical basis with $\vec{e}_\pm = \frac{1}{\sqrt{2}}(\mp\vec{e}_x + i\vec{e}_y)$, where $\{\vec{e}_x, \vec{e}_y, \vec{e}_z\}$ are the basis vector of a Cartesian coordinate system:

$$\langle\vec{e}_\pm|\vec{B}\rangle = \frac{B}{2\sqrt{2}}\left(\mp 1 + ie^{-i\phi_c}\right)e^{-i\omega t} + \text{c.c.} = B_\pm e^{-i\omega t} + \text{c.c.}$$

$$\Rightarrow \vec{B} = \left(B_+ e^{-i\omega t}\vec{e}_+ + B_- e^{-i\omega t}\vec{e}_- + \text{c.c.}\right) + B_z\vec{e}_z \tag{3.10}$$

The corresponding complex field amplitudes are defined as $B_\pm = \frac{B}{2\sqrt{2}}\left(\mp 1 + ie^{-i\phi_c}\right)$. We can now proceed to write the Hamiltonian associated to the total magnetic field using the corresponding spin-1 operators $\{\hat{F}_+, \hat{F}_-, \hat{F}_z\}$ with $\hat{F}_\pm = \hat{F}_x \pm i\hat{F}_y$. Here, we distinguish the fact that the Landé g-factors in $F = 1$ and $F = 2$ have different signs, giving rise to Larmor precessions in opposite directions. We write this as $g_F = \alpha|g_F|$ with $\alpha = \{-1, 1\}$ for $F = \{1, 2\}$ and cast the Hamiltonian to:

$$\hat{H} = \alpha|p_F|\hat{F}_z + \frac{\alpha|g_F|\mu_B}{\sqrt{2}}\left[-B_+ e^{-i\omega t}\hat{F}_+ + B_- e^{-i\omega t}\hat{F}_- + \text{h.c.}\right] \tag{3.11}$$

where we use the identity $\hat{\vec{F}}\vec{e}_\pm = \mp\frac{1}{\sqrt{2}}\hat{F}_\pm$ [Per13]. We go into the *rotating frame* of the F manifold which co-precesses with p_F and transform the operators accordingly $\hat{F}_\pm \to e^{\pm i\omega t}\hat{F}_\pm$ and $\hat{F}_z \to 0$ since we assume $\omega = |p_F|$ and $\delta = 0$. Thereby we obtain the effective Hamiltonian:

$$\hat{H}_{\text{eff}} = \frac{\alpha|g_F|\mu_B}{\sqrt{2}}\left[-B_+ e^{-i(1-\alpha)\omega t}\hat{F}_+ + B_- e^{-i(1+\alpha)\omega t}\hat{F}_- + \text{h.c.}\right] \tag{3.12}$$

We employ the *rotating wave approximation*, neglect the terms oscillating with 2ω in $\hat{H}_{\text{eff}}$ as they averaged out and consider only the static ones in the corresponding rotating frames:

$$\hat{H}_{\text{eff}} = \begin{cases} -\frac{|g_2|\mu_B}{\sqrt{2}}\left(B_+\hat{F}_+ + \text{h.c.}\right) & \text{, for } F = 2 \\ -\frac{|g_1|\mu_B}{\sqrt{2}}\left(B_-\hat{F}_- + \text{h.c.}\right) & \text{, for } F = 1 \end{cases} \tag{3.13}$$

From this effective Hamiltonian, it becomes clear that the atoms in $F = \{1, 2\}$ are only addressed by the *circularly polarized* $\sigma_{-,+}$ components of the RF-field with complex amplitudes $B_{-,+}$. This is due to the opposite direction of the Larmor precession in the two manifolds and is schematically represented in Fig.3.4(b). Taking this into account, we choose the relative phase between the RF-fields of the coils to be $\phi_c = \frac{\pi}{2}$. Thereby we generate a σ_--field which selectively addresses the atoms in $F = 1$:

$$\hat{H}_{\text{eff}}\left(\phi_c = \frac{\pi}{2}\right) = \begin{cases} 0 & \text{, for } F = 2 \\ -|g_1|\mu_B B\hat{F}_x & \text{, for } F = 1 \end{cases} \tag{3.14}$$

where we use $B_\pm\left(\phi_c = \frac{\pi}{2}\right) = \frac{1}{2\sqrt{2}}[\mp 1 + 1]$.
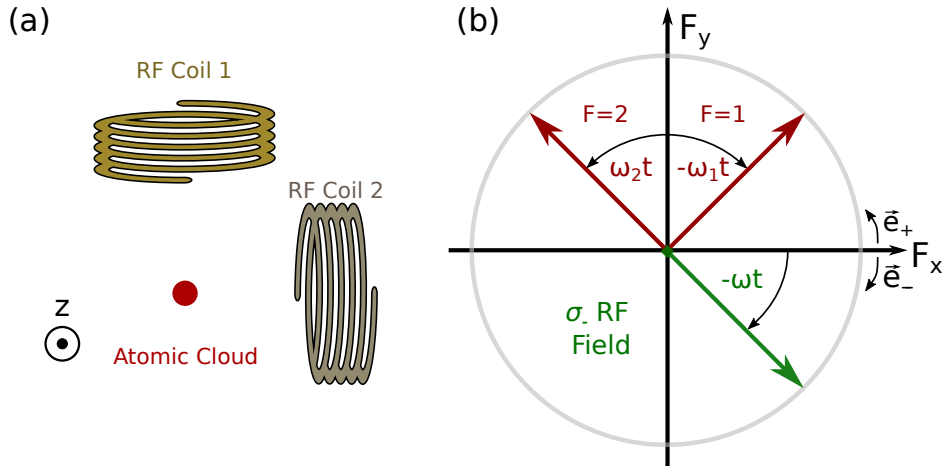
Figure 3.4.: **Selective addressing of atoms F=1 using a two coil RF setup .**
We employ two orthogonal coils **(a)** to produce linearly polarized RF-
fields in the x-y plane which can be superimposed to generate circularly
polarized fields $\sigma_\pm$. Due to the opposite sign of the Landé g-factors
in F=1 and F=2, the Larmor precession **(b)** takes place in opposite
directions (red arrows). A σ_- RF-field oscillating with the same frequency
$\omega = \omega_1$ (green arrow) selectively addresses the atoms in F=1. This can
be explained after transforming into the rotating frame of the atoms in
the different manifolds, since the RF field is only static in the $F = 1$
frame of reference.

Calibration of Selective Addressing of Atoms in $F = 1$

We experimentally verify whether we can selectively address the atoms in $F = 1$ with
RF-pulses and experimentally calibrate the phase ϕ_c. For this purpose, we prepare
balanced superpositions $|1, -1\rangle + |2, -2\rangle$ of $N \approx 35000$ atoms in the waveguide
trap using a resonant MW $\frac{\pi}{2}$-pulse to transfer half of the atomic populations to
$|2, -2\rangle$. We address this state for $t_{\text{Rabi}} \leq 2\,\text{ms}$ with RF-fields resonant to the first-
order Zeeman splitting in $F = 1$ and tune the relative phase of the two coils ϕ_c.
We probe the induced Rabi oscillations by examining the magnetization in the
z-direction which we extract as $\langle \hat{F}_z \rangle_1 = \frac{1}{N_1} [N_{1,1} - N_{1,-1}]$ in $F = 1$ and $\langle \hat{F}_z \rangle_2 =
\frac{1}{N_2} [2N_{2,2} + N_{2,1} - N_{2,-1} - 2N_{2,-2}]$ in $F = 2$, where N_F and N_{F,m_F} are the atom
numbers in the F manifold and the in magnetic sub-level $|F, m_F\rangle$. Exemplary Rabi
oscillations in $F = 1$ and $F = 2$ for different relative phases ϕ_c are plotted in Fig.A.1
and A.2 in the appendix.

We fit the oscillations of the magnetization with sinusoidal functions and estimate
thereby the Rabi frequency $\Omega_{\text{RF}}/(2\pi)$. We plot the Rabi frequencies in $F = 1$ and
$F = 2$ for different values of ϕ_c in Fig.3.5. The detuning $\delta \approx 2\pi \times 2.5\,\text{kHz}$ of the
RF-Rabi in $F = 2$ is corrected using the formula $\Omega_{\text{RF}} = \sqrt{\Omega_{\text{RF,fit}}^2 - \delta^2}$.

We clearly see that the Rabi frequencies in $F = 1$ and $F = 2$ are anti-correlated
as we adjust ϕ_c, which is consistent with the theoretical expectations discussed
before. The RF-Rabi frequency in $F = 1$ and $F = 2$ are minimized for the phases
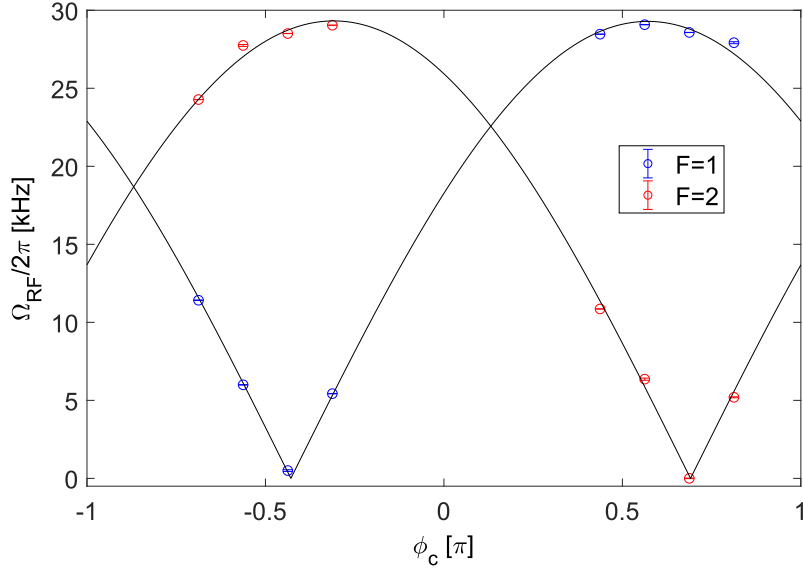
Figure 3.5.: **Calibration of selective RF-rotations in F=1 and F=2 .** We prepare balanced superpositions $|2, -2\rangle + |1, -1\rangle$ and address them with RF-fields from the two coil setup sketched in Fig.3.4(a). The Rabi frequency Ω_{RF} is estimated by fitting $\langle F_z \rangle$ with a sine. We plot Ω_{RF} vs. the relative phase of the fields originating from the two coils ϕ_{c} for $F = 1$ (blue) and $F = 2$ (red circles). The small error bars correspond to the 1σ fitting error. We clearly see an anti-correlated trend of the Rabi frequencies in the two manifolds when adjusting ϕ_{c}, which is expected since thereby we generate $\sigma_{-,+}$ RF-fields which address only the atoms in $F = \{1, 2\}$. Fitting $\frac{\Omega_{\mathrm{RF}}}{2\pi} = A \left| \sin \left(\phi_c - \phi_{c,F} \right) \right|$ (solid black line) we can estimate the phases minimizing the Rabi frequency in $F = \{1, 2\}$ and obtain $\phi_{\mathrm{c},1} = -0.43\pi$ and $\phi_{\mathrm{c},2} = 0.69\pi$. We choose $\phi_{\mathrm{c},2}$ to selectively address the atoms in $F = 1$ during the F_x-F_y readout.

$\phi_{\mathrm{c},1} \approx -0.43\pi$ and $\phi_{\mathrm{c},2} \approx 0.69\pi$ which we extract by fitting $\frac{\Omega_{\mathrm{RF}}}{2\pi} = A \left| \sin \left(\phi_c - \phi_{c,F} \right) \right|$. The discrepancy between the experimental $\Delta\phi_c = \phi_{\mathrm{c},1} - \phi_{\mathrm{c},2} = 1.12\pi$ and theoretical phase difference $\Delta\phi_{\mathrm{c,theo}} = \pi$ is most likely due to the fact that the two coils do not generate perfectly orthogonal fields. Hence, we choose $\phi_{\mathrm{c}} = 0.69\pi$ from now on in order to address only the atoms in $F = 1$ during F_x-F_y readout.

3.3.3. Error Characterization of the F_x - F_y Readout

In order to quantify the systematic error of the readout and understand the underlying causes we perform *control measurements*. We prepare an initial polar state $|\psi_0\rangle = (0, 1, 0)^T$ and let it evolve for variable long evolution times $t_{\mathrm{evo}} \leq 15\,\mathrm{s}$ and suppressed spin-mixing. We examine these states using the F_x-F_y readout scheme. Ideally, the RF-rotated polars in $F = 1$ and $F = 2$ are expected to have populations only in the side modes:

$$|\psi(F=2)\rangle = \exp\left(-i\frac{\pi}{2}\hat{F}_y\right)\begin{pmatrix}0\\1\\0\end{pmatrix} = \begin{pmatrix}\frac{1}{\sqrt{2}}\\0\\-\frac{1}{\sqrt{2}}\end{pmatrix}$$

$$|\psi(F=1)\rangle = \exp\left(-i\frac{\pi}{2}\hat{F}_x\right)\exp\left(-i\frac{\pi}{2}\hat{F}_y\right)\begin{pmatrix}0\\1\\0\end{pmatrix} = \begin{pmatrix}\frac{1}{\sqrt{2}}\\0\\-\frac{1}{\sqrt{2}}\end{pmatrix} \qquad (3.15)$$

While this is indeed the case for the atoms in $F=2$ as we see in Fig.3.6(a), we observe that the normalized population in $|1,0\rangle$ after the readout pulses growths up to $\rho_0 \approx 0.17$ within $t_{\text{evo}} \leq 15\,\text{s}$ accompanied also by increasingly larger fluctuations.

This is most likely due to drifts and increasingly large fluctuations of the bias field ΔB_z for longer duty cycles. As we see in the pulse sequence in Fig.3.3(a), there is a finite waiting time $t_w = 400\,\mu\text{s}$ between the two RF-readout pulses required to shelve atoms in the $F=2$ manifold. During this time the system precesses under the influence of the first-order Zeeman shift $\hat{H} = g_F\mu_B B_z$ with $B_z = 0.884\,\text{G}$. Thus, an error ΔB_z of the bias field gives rise to an additional Larmor phase error $\Delta\phi$:

$$|\psi(F=1)\rangle = \exp\left(-i\frac{\pi}{2}\hat{F}_x\right)\exp\left(i\Delta\phi\hat{F}_z\right)\exp\left(-i\frac{\pi}{2}\hat{F}_y\right)|\psi_0\rangle \qquad (3.16)$$

with $\Delta\phi = \frac{|g_1|\mu_B\Delta B_z}{\hbar}$. The expected Larmor phase accumulated during t_w is compensated by adding $\frac{|g_1|\mu_B B_z}{\hbar}$ to the relative phase of the second RF-pulse.

We evaluate the expression in Eq.(3.16) numerically to obtain $\Delta\phi$ as a function of the population in $|1,0\rangle$ and plot $\Delta\phi(t_{\text{evo}})$ together with its standard deviation in Fig.3.3(b). While the Larmor phase error is initially small $\Delta\phi(0) = (0.05 \pm 0.02)\pi$, both the average and fluctuations of the error constantly increase with the evolution time reaching $\Delta\phi(15\,\text{s}) = (0.13 \pm 0.06)\pi$.

This Larmor phase uncertainty directly corresponds to an *error in the angle of second RF-rotation* when represented in the spin-1 sphere. Thus, the second readout axis is not orthogonal to the first one but rather displaced by $\Delta\phi \lesssim 0.14\pi = 25°$ at late times, moderately affecting the experimentally extracted transverse spin length: For states with $\langle\hat{F}_z\rangle = 0$ this introduces a maximal *systematic error* on the order of $\Delta F_\perp/F_\perp = [1 - \cos(\Delta\phi)] \lesssim 0.1$ for evolution times $t_{\text{evo}} \leq 15\,\text{s}$.

As previously stated, this readout error probably originates from fluctuations and drifts of the bias field ΔB_z which seem to increase with the duration of the duty cycle (evolution time). We can estimate them via $\Delta\phi = |g_1|\mu_B\Delta B_z/\hbar$ and plot $\Delta B_z(t_{\text{evo}})$ in Fig.3.3(c). At small times the inferred B-Field fluctuations $\Delta B_z(0) = (100 \pm 24)\mu\text{G}$ are comparable with the typical B-field stability $\sim 40\,\mu\text{G}$. The latter was obtained from a direct characterization of the active magnetic field control setup in [Str16]. Meanwhile, at lager times both the average and standard deviation of the magnetic field error increase reaching values around $\Delta B_z(15\text{s}) = (270 \pm 120)\mu\text{G}$. The inferred magnetic field drift for long t_{evo} and can be due to the fact that the active B-field control is optimized for $t_{\text{evo}} < 1\,\text{s}$. Moreover, the increasing fluctuations also suggest that the experiment is more susceptible to external noise for longer duty cycles such as for instance the 50 Hz noise from the power grid.
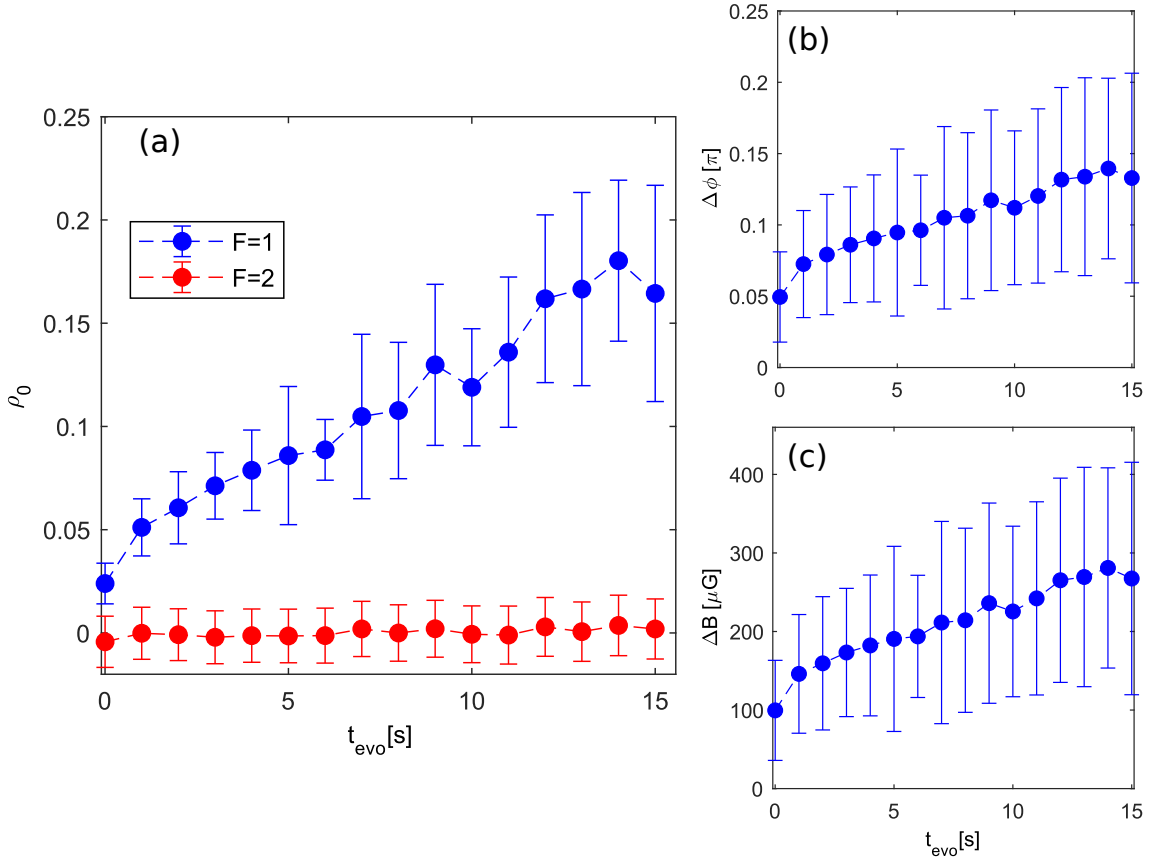
Figure 3.6.: **Systematic error of the F_x - F_y readout.** We examine a polar state after variable evolution and suppressed spin-mixing with the F_x-F_y readout. We plot the mean and standard deviation (error bars) of the central mode population ρ_0 in $F = \{1, 2\}$ after the corresponding RF-rotations **(a)**. While in F=2 we consistently obtain $\rho_0 \approx 0$ as expected, the mean and fluctuations of the population in $|1,0\rangle$ steadily increase. This trend is numerically related to a Larmor phase error $\Delta\phi$ plotted in **(b)**. The mean and standard deviation (error bars) significantly increase for longer duty cycles. They directly correspond to an increasing error in the angle of the second RF-rotation and affect the extracted $F_\perp$ value. This most likely originates from errors of offset bias field ΔB_z **(c)** which we estimate from $\Delta\phi$. The inferred initial error is comparable within 3σ's to the $\sim 40\,\mu G$ active B-field stabilization [Str16], whereas it significantly drifts at longer evolution times. Together with the increasing fluctuations (error bars), this trend suggests that the experiment is increasingly more susceptible to technical noise for longer duty cycles.

4. Coherent Spin Dynamics

After discussing the theoretical background and the relevant experimental techniques, we can experimentally study coherent spin dynamics in our system. We introduce a Truncated Wigner simulation beforehand, which allows us to model the spin dynamics in our system taking into account the dephasing due to intrinsic quantum fluctuations. Afterwards, we present first experimental results for the short-time dynamics of the transverse spin $F_\perp$ examining evolution times up to $t_{\rm evo} \leq 1\,{\rm s}$. A direct comparison shows that the experimental observations are compatible with the predictions arising from the mean field equations of motion.

4.1. Simulating Spin Dynamics with Quantum Fluctuations

4.1.1. Motivation: The Role of Quantum Fluctuations

So far we have modeled the evolution of single-mode spin-1 system using the mean field equations of motion listed in Eq.(2.17). By construction, this approach disregards the effect of *quantum fluctuations* on the dynamics.

If we consider a *coherent spin-1 state* consisting of N uncorrelated particles, the intrinsic fluctuations of an observable $\hat{O}$ such as a spin direction are expected to scale as $\Delta \hat{O} \propto \sqrt{N}$ [Kit93]. However, since expectation values linearly increase with the system size $\langle \hat{O} \rangle \propto N$ the relative uncertainty scales as $\Delta \hat{O} / \langle \hat{O} \rangle \propto 1/\sqrt{N}$ and is neglected for macroscopic systems within mean field approaches. Attempting to consider the impact of fluctuations on the dynamics and simulate the full quantum mechanical evolution of the system is a difficult task, even within the single-mode approximation: The complexity of typical sparse matrix algorithms required to diagonalize the Hamiltonian in Eq.(2.14) increases exponentially with the number of atoms $O(2^N)$ [Hal12], since the size of the Hilbert space grows as $\propto N$ in a Fock state representation [Ger13]. Thus, a full quantum computation for typical experimental atom numbers $N \sim 10^4$ is time intensive and beyond the scope of this thesis.

Here, we resort instead to a *Truncated Wigner* approach in order to simulate the spin dynamics in our system. This semi-classical method relies on stochastically sampling the fluctuations of the initial state and evolving the system afterwards using classical mean field equations of motion. These methods are commonly used to simulate the dynamics of interacting Bose gases [Bla08, Sin02]. More details concerning their applicability to our experimental system can be found in [Lin17].

4.1.2. Implementation of the Simulation

In order to reproduce the experimental preparation, we start the simulation with a polar state $(0, \sqrt{N}, 0)^T$ with N particles and consider the associated fluctuations. We record S samples of the initial state and introduce complex 'quantum $\frac{1}{2}$ noise' in the empty modes of the polar state in each realization $s \in S$ of the simulation:

$$|\psi_s\rangle = (\frac{1}{2}[\alpha_1 + i\beta_1], \quad \sqrt{N}, \quad \frac{1}{2}[\alpha_{-1} + i\beta_{-1}])^T \tag{4.1}$$

where the $\alpha_{\pm 1}$ and $\beta_{\pm 1}$ are random numbers drawn from a normal distribution with mean and standard deviation $(\mu, \sigma) = (0, 1)$. The factor $\frac{1}{2}$ effectively enforces half a particle on average in the empty side modes of the polar state.

We normalize $|\psi_s\rangle$ and prepare an initial state with finite transverse magnetization by applying a ϕ_{RF}-rotation around $\hat{F}_x$ in order to transfer populations to the side modes. We enforce a subsequent spinor phase evolution, mimicking thereby the experimental preparation sequence:

$$|\psi\rangle = \exp\left(-i\frac{\pi}{4}\hat{Q}_{zz}\right) \exp\left(-i\phi_{\mathrm{RF}}\hat{F}_x\right) \frac{1}{\bar{N}} |\psi_s\rangle \tag{4.2}$$

with inner product $\bar{N} = \langle\psi_s|\psi_s\rangle$. This particular noise sampling procedure ensures *coherent state fluctuations*: We assess this by examining not-normalized initial states $\bar{N}|\psi\rangle$ and computing the variances of the atom numbers in the individual modes N_j within the sample set S, with $j \in \{-1, 0, 1\}$. We observe coherent state fluctuations compatible with a multinomial distribution $\sigma_{N_j}^2 \approx p_j(1 - p_j)N_j$, with occupation probabilities $p_j = N_j/N$.

Afterwards, we evolve the individual samples $|\psi_s\rangle$ numerically using the coupled mean field equations of motion for the individual components of a spinor presented in Eq.(2.18). We estimate the expectation values of spin-1 observables such as $\hat{F}_{x,y}$ by computing the mean over all the samples $s \in S$ at fixed evolution times:

$$\langle\hat{O}(t_{\mathrm{evo}})\rangle = \langle\hat{O}(t_{\mathrm{evo}})\rangle_{\mathrm{S}} \tag{4.3}$$

where $\langle\rangle_{\mathrm{S}}$ denotes an average over the sample set S. The fluctuations can be extracted accordingly. We typically employ samples of $S \approx 1000$ runs in order to ensure that the computed averages and variances are numerically stable. A key advantage of this method is that the complexity scales only linearly with the sample size $O(S)$, but is independent of the particle number N allowing us to simulate the dynamics [1] for typical experimental atom numbers $N \sim 10^4$.

4.1.3. Simulation for typical Experimental Parameters

In order to examine impact of quantum fluctuations on the dynamics, we use this Truncated Wigner method and simulate the dynamics for typical experimental

---

[1]A direct comparison of this method to a full numerical quantum computation for $N \leq 1000$ atoms has been carried out in our group by Martin Gärttner and shows reasonable agreement between expectation values (e.g. $F_\perp$ and ρ_0) even after long evolution times $t_{\mathrm{evo}} \sim 10\,\mathrm{s}$.

parameters $N = 10000$ atoms and $(q, \lambda_1) = 2\pi \times (1.25, -2)$Hz. We use $S = 1000$ samples and enforce a $\phi_{\mathrm{RF}} = \frac{\pi}{4}$ rotation around $\hat{F}_x$ in order to produce an initial state with maximal transverse spin $\langle F_\perp \rangle = 1$.

We present the expectation values of $F_\perp$ and $2\rho_0 - 1$ in Fig.4.1 (a) and (b) respectively covering evolution times up to $t_{\mathrm{evo}} \leq 18$ s. At small times, we observe oscillations with moderate amplitude (e.g. ~ 0.2 peak to peak for $F_\perp$) and frequency $f \approx 3.5$ Hz which are only minimally damped within the first few seconds of evolution. Moreover, these two observables oscillate in an anti-correlated fashion which is expected from the form of the mean field trajectories in the spin-nematic sphere. As t_{evo} is increased, the oscillations damp towards stationary values $\langle F_\perp \rangle_{\mathrm{st}} \approx 0.88$ and $\langle 2\rho_0 - 1 \rangle_{\mathrm{st}} \approx 0.32$ within a rather long timescale of ~ 15 s.

In order to understand the underlying mechanism leading to this damping, we plot the individual samples in spin-nematic spheres (orange points) for representative evolution times $\{0, 0.8, 5.1, 18\}$s in Fig.4.1(c). We also plot the corresponding phase-space trajectories for $q/\lambda_1 = -0.625$ as a guide to the eye. The initial fluctuations are small and compatible with the coherent state expectations of a fully elongated spin in the transverse plane $\Delta\rho_0 \approx 1/\sqrt{N}$ and $\Delta F_\perp \approx 0$. As the evolution time is increased, the individual realizations traverse the phase space and start to shear along the associated trajectories: Because of the introduced quantum noise, the individual samples are initialized in slightly different positions of the phase space and anharmonically oscillate with different frequencies due to the non-linear mean field equations of motion. As the evolution time is further increased (~ 18 s), the individual samples are governed by *dephasing* and fully delocalize around the corresponding mean field trajectory. Since the associated spin-1 state is then equally likely to be measured in each point of the trajectory, the expectation values damp and become stationary. Moreover, the late-time fluctuations of the system are expected to saturate and be commensurate with the region of the spin-nematic sphere sampled by the initial dynamics or equivalently with the amplitude of the initial oscillations. This distinctive trend of the fluctuations is employed later in chapter 6, in order to diagnose late-time dephasing in our system.
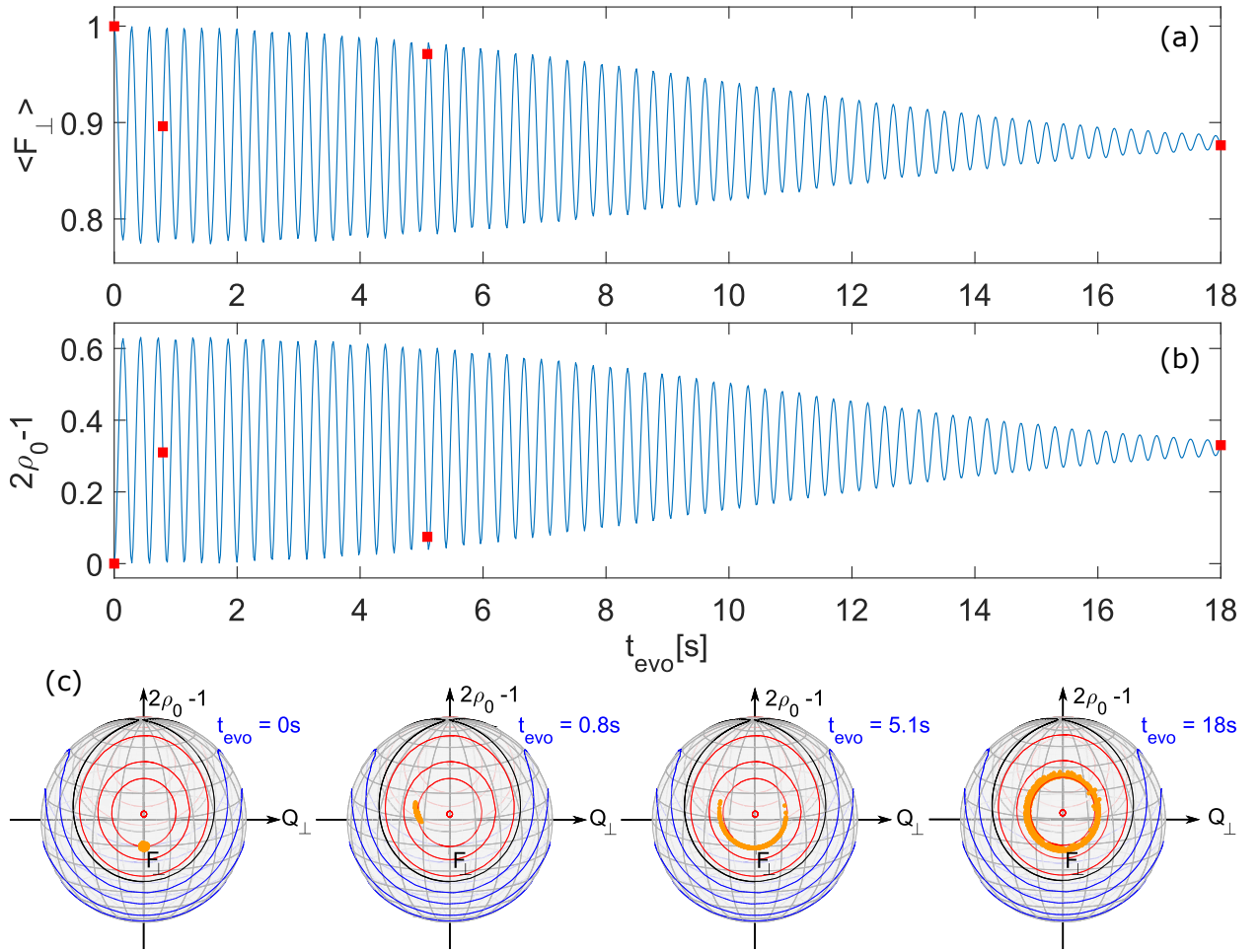
Figure 4.1.: **Truncated Wigner simulations for typical experimental parameters.** We employ $N = 10000$ atoms, $(q, \lambda_1) = 2\pi \times (1.25, -2)$Hz, 1000 samples and $(F_\perp(0), \rho_0(0)) = (1, 0.5)$. The simulated evolution of the expectation values of $F_\perp$ and $2\rho_0 - 1$ is displayed in **(a)** and **(b)**. These quantities exhibit anti-correlated oscillations with frequency around ~ 3.5 Hz which damp within ~ 15 s. In order to understand this damping, we plot the individual samples (orange points) in spin-nematic spheres **(c)** for representative times $\{0, 0.8, 5.1, 18\}$s together with the corresponding phase space trajectories (solid lines). The initial condition exhibits small fluctuations compatible with a coherent spin state. As the time progresses, the individual runs oscillate with different frequencies due to the introduced noise and the underlying non-linear equations of motion and start to shear along the corresponding mean field trajectory. At long-times around ~ 18 s, the state fully *dephases* and delocalizes along the corresponding trajectory. This results in stationary expectation values for $F_\perp$ and $2\rho_0 - 1$ and explains the observed damping.

4.2. Examining $F_\perp$ Oscillations

Once we have developed tools to experimentally probe and simulate our system, we can examine whether coherent spin dynamics takes place. This type of evolution has already been studied in detail for both ferromagnetic ($\lambda_1 < 0$) [Cha05] and antiferromagnetic ($\lambda_1 > 0$) [Bla07] spin-1 condensates. These studies mainly focus on probing population oscillations between the individual magnetic sub-levels such as ρ_0, since these quantities are readily accessible by means of state selective imaging. In order to complement these studies, we focus here rather on probing the transverse magnetization and examine short-time $F_\perp$ oscillations within $t_{\text{evo}} \leq 1$s. We prepare non-equilibrium initial conditions away from the mean field fixpoint by adjusting the initial transverse spin length. The F_x-F_y readout is here essential in order to directly extract the transverse spin.

Throughout this section we work in the waveguide trap with $N \approx 40000$ atoms ($\lambda_1 \approx -2\pi \times 2.1$ Hz) and set $q \approx 2\pi \times 3.7$ Hz. The condensate confined in the waveguide trap is in principle a multi-mode system, since its longitudinal extension $\sim 200\,\mu$m is significantly larger than the spin healing length which is on the order of few microns. However, we have experimentally observed that F_x and F_y do not develop significant spatial structures within the first second of evolution for $F_\perp(0) > 0$. We further restrict the evaluation to a central region of $\lesssim 40\,\mu$m where the relative variation of the total density is on the order of $\Delta n/n \lesssim 5\%$ in accordance with a local-density approximation. In this way we seek to minimize the role of potential spatial spin excitations since we want to compare the observed dynamics to a single-mode theoretical picture. The mean field parameters q and λ_1 are estimated by minimizing the deviation between theoretical and experimental ρ_0 oscillations. This procedure is explained in section in A.5 in the appendix.

Here, we want to probe the phase space for a representative mean field ratio $q/|\lambda_1| = 1.75$. To this end, we prepare states with different initial transverse spin lengths by adjusting the duration of RF preparation pulse as described in Eq.(3.2). We measure the two directions of the transverse magnetization after variable evolution time t_{evo} using the F_x-F_y readout scheme and quadratically add them to obtain $F_\perp = \sqrt{F_x^2 + F_y^2}$. The extracted transverse spin is positive[2] by construction $F_\perp > 0$.

In Fig.4.2 (a)-(c) we plot the experimental oscillations of the average transverse spin (blue points) for different initial conditions $\langle F_\perp(0) \rangle \approx \{0.25, 0.53, 0.91\}$ within $t_{\text{evo}} \leq 1$s. We compute the expectation values by averaging over ~ 10 independent realizations. For the smallest displayed initial $F_\perp$ value, we observe clear oscillations with amplitude ~ 0.2. As the initial spin length is increased (b), the oscillations are significantly suppressed. This is expected, since we initialize the system close to the fixpoint $F_\perp^{\text{FP}} \approx 0.48$ of the mean field dynamics as we also see in the spin-nematic spheres plotted in Fig.4.2(d). If we further increase the initial spin length to $\langle F_\perp(0) \rangle \approx 0.91$ (c), we observe oscillations exploring a wide range of transverse

---

[2]This experimental value is proportional to $F_\perp \propto |\cos\left(\frac{\theta_s}{2}\right)|$ (see Eq.(2.20)). In order to assess the sign of $F_\perp$, we would need to extract the actual value of the spinor phase θ_s. This quantity can be inferred after simultaneously probing F_x and Q_{yz}, which is possible after minimal modifications of the readout scheme but beyond the scope of this thesis.

magnetizations as the system is initialized in an open trajectory.

Since damping does not seem to substantially affect the dynamics within the first second of evolution, we compare the experimental results to theory predictions obtained after solving the mean field equations of motion numerically for $(q, \lambda_1) = 2\pi \times (3.7, -2.1)$Hz (solid black lines in Fig.4.2). Especially for small evolution times, we observe qualitative agreement between theory and experiment. The data in (a) and (c) exhibits more outliers at lager evolution times $t_{\text{evo}} \geq 0.6$s. Moreover, if the system is initialized close to the fixpoint (b) the experimental data seems to be affected by fluctuations limiting the compatibility with the theoretical predictions.

A more systematic comparison to mean field theory is displayed in Fig.4.3. We tune a wide range of initial spin lengths for fixed mean field ratio $q/|\lambda_1| \approx 1.75$ and compare the amplitude of the experimental and theoretical $F_\perp$-oscillations. We estimate the experimental amplitudes by fitting a sine (or its absolute value) in the case of closed (open) trajectories and extract the theoretical values from the numerics as half of the peak-to-peak amplitude. We observe reasonable agreement between theory and experiment as nearly all points are consistent within 3σ's of the fit errors. The behavior of the oscillation amplitude can be explained relying on the trajectories on the spin-nematic sphere displayed in Fig.4.2(d): As $\langle F_\perp(0) \rangle$ is increased, the oscillation amplitude first decreases since we approach the fixpoint of the dynamics $\langle F_\perp(0) \rangle \approx 0.48$ and then increases again as we depart from this point. Crossing the separatrix around $\langle F_\perp(0) \rangle \approx 0.66$ modifies the growth rate of the oscillation amplitudes, since we enter the region of open trajectories.

We have also assessed the agreement of the short-time $F_\perp$-oscillations with the theoretical predictions for further mean field ratios $q/|\lambda_1| \approx 0.25$ and $q/|\lambda_1| \approx 0.6$ and comparable initial conditions.

Conclusions

In this chapter, we experimentally studied the short-time dynamics within $t_{\text{evo}} \leq 1$s for states with finite initial transverse spin $\langle F_\perp(0) \rangle > 0$. We specifically concentrate on mean field parameters for which we expect spin-mixing dynamics $q/|\lambda_1| = 1.75 < 2$ and therefore also coherent oscillations of both populations (e.g ρ_0) and coherences (e.g $F_\perp$). The short-time oscillations of the transverse spin $\langle F_\perp \rangle$ are compatible with the theoretical mean field predictions for different initial conditions.

In the next chapters, we shift our focus to considerably larger evolution on the order of $t_{\text{evo}} \approx 10$ s where the comparability with mean field and even with Truncated Wigner approaches breaks down. We observe then not only damping of the oscillations but also a decay of the transverse spin $\langle F_\perp \rangle \to 0$ indicating long-time decoherence in our system.
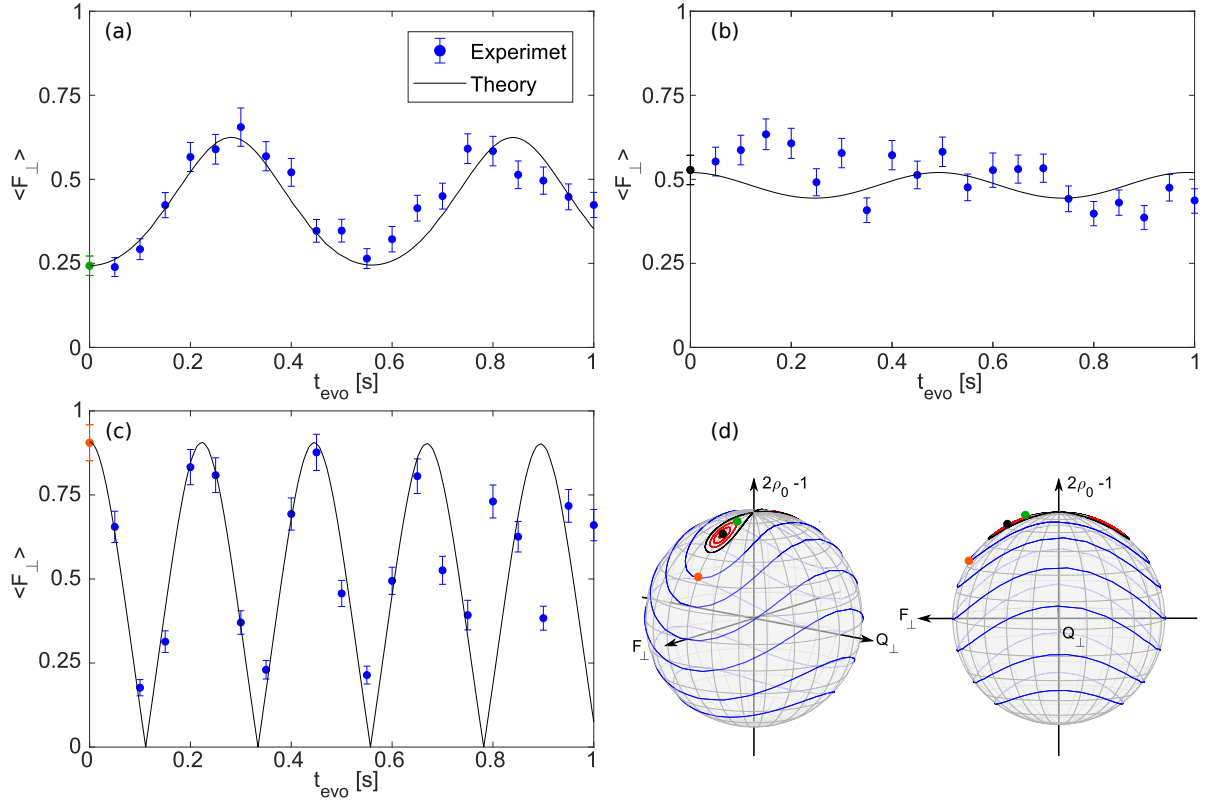
Figure 4.2.: **Experimental oscillations of the transverse spin for different initial conditions and mean field predictions.** We average over $\sim$ 10 realizations and plot the evolution of $\langle F_\perp \rangle$ (blue points) for initial spin lengths $\langle F_\perp(0)\rangle \approx \{0.25, 0.53, 0.91\}$ **(a)-(c)**. The error bars correspond to the standard error of the mean (SEM). For the smallest initial value examined (a) we observe clear oscillations. As we increase the initial spin length, they are first nearly suppressed (b) and then increase significantly (c). This can be explained relying on the trajectories on spin-nematic sphere **(d)**: While the first initial condition (green circle) evolves within a closed trajectory (red curves), the second one (black circle) is initialized close to the fixpoint and exhibits therefore minimal oscillations. Moreover, the last one (orange circle) is initialized in the region of open trajectories (blue lines) and samples therefore a broad range of $F_\perp$ values. We observe reasonable agreement between the experimental observations and the mean field predictions for $(q, \lambda_1) = 2\pi \times (3.7, -2.1)$Hz (solid black lines), especially for $t_{\mathrm{evo}} \lesssim 0.6$ s and away from the fixpoint.
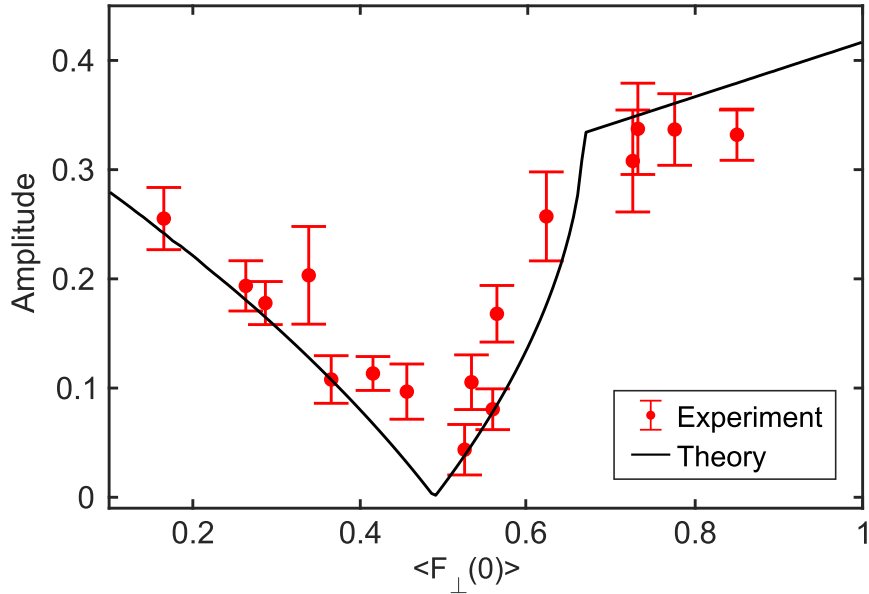
Figure 4.3.: **Comparison of the amplitude of experimental and mean field $F_\perp$ oscillations for different initial conditions.** The experimental amplitudes (red points) for different initial spin lengths $\langle F_\perp(0) \rangle$ are estimated by fitting a sine (or its magnitude) for closed (open) trajectories. The error bars reflect 1σ fit errors. Meanwhile, the theoretical values (solid black line) are directly extracted from the numerics for $q/|\lambda_1| = 1.75$. We observe a compatible trend for theory and experiment and that the majority of values coincide within 3σ's. The observed behavior can be explained in a mean field picture: The oscillation amplitude is minimized close to the fixpoint at $\langle F_\perp(0) \rangle \approx 0.48$, while the growth rate of the amplitude changes as we cross the separatrix around $\langle F_\perp(0) \rangle \approx 0.66$.

5. Decoherence and Heating

After examining the short-time spin oscillations, we go one step further and probe the dynamics in our system after long evolution times on the order of $\sim 10\,\text{s}$. This timescales are large compared to the internal one introduced by spin-spin interactions ($\sim 2\,\text{Hz}$). We observe that the transverse magnetization decays towards zero indicating the progressive decoherence in the system. In this context, we examine the influence of different experimental parameters on this process: First, we study the impact of the detuning q and realize that the transverse spin survives significantly longer within the q regime exhibiting spin-mixing. Afterwards, we concentrate on finite temperature effects. We experimentally control the heating of the condensate density by adjusting the power of the waveguide trapping beam. After examining different settings, we observe a clear correlation between the heating of the condensate and the long-time behavior of the transverse spin $F_\perp$. The latter survives considerably longer ($t_\text{evo} \gtrsim 15\,\text{s}$) if we mitigate the impact of heating.

5.1. Long-Time Decoherence

From now on we restrict our studies to condensates prepared in the tightly confining *crossed beam dipole trap* (see Fig.3.2(a)) since we want to concentrate on studying the internal spin dynamics. Even for comparably tightly confined condensates, spin-mixing dynamics can exhibit multiple resonances as q is tuned [Kle09] and excite higher trapping modes [Sch10] giving rise to spatially dependent spin-patterns. In our crossed-beam dipole trap, this behavior is also observable after parametric quenches of an initial polar state ($\rho_0 = 1$) across the phase transition towards the easy-plane ferromagnetic phase $q_0 > 2|\lambda_1| \rightarrow q_1 < 2|\lambda_1|$. Excitations of higher trapping modes are visible for $N \gtrsim 20000$ atoms and small detuning values $q \lesssim 0$ as modulations of the density profiles of the individual magnetic sub-levels. Since we want to stay in the single-mode regime, we restrict our studies to atom numbers $N < 20000$ and positive detuning values $q > 0$. If not specified otherwise, we operate with trapping frequencies on the order of $(\omega_{||}, \omega_\perp) \approx 2\pi \times (46, 220)\text{Hz}$.

We prepare states with $N \approx 14000$ atoms and initial spin $\langle F_\perp(0) \rangle = 0.8$ and monitor the dynamics for $(q, \lambda_1) \approx 2\pi \times (1, -2.75)\text{Hz}$. We plot the temporal evolution of the average transverse spin in Fig.5.1 for both short (a) and long times (b). We extract $\langle F_\perp \rangle$ as in the previous chapter after averaging over ~ 15 realizations. Within the first second of evolution, we observe clear oscillations with a frequency around $\sim 4.5\,\text{Hz}$. However, the dynamics is remarkably different to the one predicted by mean field theory and $\langle F_\perp \rangle$ exhibits a decaying trend already within the first second of evolution.

We plot also the long-time evolution of the transverse spin up to $t_\text{evo} \leq 14\,\text{s}$ in

5. Decoherence and Heating

Fig.5.1(b) and observe a constant *decay* towards zero. This trend indicates long-term *decoherence* in the system as $F_\perp$ is determined by the relative phases between the central and side modes as we see in Eq.(3.5). We estimate the associated timescale using an exponential fit (red line) with fixed amplitude and offset[1] and obtain the $\frac{1}{e}$ life-time $T_{LT} = (11.77 \pm 0.33)$s. Moreover, $\langle F_\perp \rangle$ does not discernibly oscillate after $2\,\mathrm{s}$ of evolution most likely due to the combined influence of dephasing and decoherence.
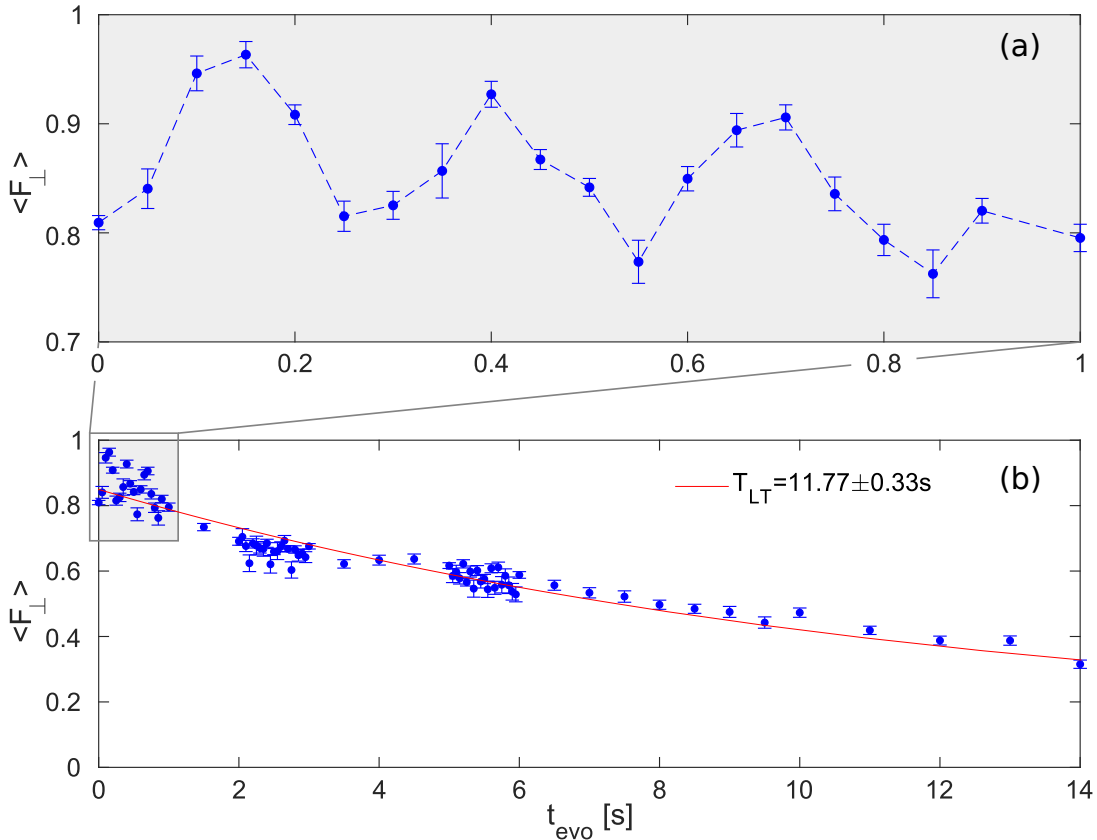

Figure 5.1.: **Short and long-time evolution of the mean transverse magnetization.** We prepare states with $N \approx 14000$ atoms, $\langle F_\perp(0) \rangle = 0.8$ and $(q, \lambda_1) \approx 2\pi \times (1, -2.75)$Hz and plot the mean transverse spin $\langle F_\perp \rangle$ within $t_{evo} \leq 1\,\mathrm{s}$ **(a)** and $t_{evo} \leq 14\,\mathrm{s}$ **(b)**. The experimental data (blue points) is averaged over ~ 15 realizations and the error bars are the SEM. Examining the short-time dynamics, we observe that $\langle F_\perp \rangle$ oscillates with frequency $f \approx 4.5\,\mathrm{Hz}$ and also exhibits a decaying trend. This trend becomes more evident in the long-term evolution as $\langle F_\perp \rangle$ decays towards zero. The $\frac{1}{e}$ life-time $T_{LT} \approx 12\,\mathrm{s}$ is estimated from an exponential fit (red line). This decay indicates the progressive loss of coherences in the system. Moreover, the oscillations are suppressed after $t_{evo} > 2$s which is attributed to the combined influence of dephasing and decoherence.

---

[1]We use the fit function $\langle F_\perp \rangle = 0.75 \exp(-t/T_{LT}) + 0.1$. The offset approximately corresponds to the experimental $F_\perp$ value for a polar state with zero transverse spin. The amplitude is selected to match the average spin of the system $\langle F_\perp \rangle = 0.85$ within the first second of evolution.

5.2. The Role of the Detuning q

We explore now the impact of different experimental parameters on the long-time decay of the transverse spin. First, we examine the role of the detuning q which we experimentally adjust using our microwave dressing setup. We prepare initial states with spin-length $\langle F_\perp(0)\rangle \approx 0.85$, $N \approx 19000$ atoms and probe the evolution of the transverse spin after $t_{\mathrm{evo}} \leq 10\,\mathrm{s}$. We estimate the $1/e$ life-time T_{LT} of $\langle F_\perp\rangle$ using exponential fits with fixed offsets and amplitudes. We exclude the point at $t_{\mathrm{evo}} = 1\,\mathrm{s}$ from the fitting routines since $\langle F_\perp\rangle$ is expected to oscillate at small evolution times.

We plot the spin life-time vs. q in Fig.5.2 and observe that it is maximized within the q regime exhibiting spin-changing collisions. We independently probe this region using a *spin-mixing spectroscopy*: We prepare initial polar states, adjust q and monitor the side mode population after a fixed evolution time of $t_{\mathrm{evo}} = 4\,\mathrm{s}$. The highlighted region in Fig.5.2 corresponds to the q regime with non-negligible side mode population. We show the corresponding spectroscopy in Fig.A.3 in the appendix. The displayed q-axis is shifted with respect to the experimental parameters q_{exp} such that the right border of the spectroscopy matches the expectation $2|\lambda_1| \approx 2\pi \times 6.6\,\mathrm{Hz}$.

The spin life-time peaks around $q = 2\pi \times 0.4\,\mathrm{Hz}$ at $T_{\mathrm{LT}} \approx 14.5\,\mathrm{s}$ ($q/|\lambda_1| \approx 0.125$), whereas it is drastically reduced as we depart from the maximum to values on the order of $T_{\mathrm{LT}} \approx 3.5\,\mathrm{s}$ and $1.5\,\mathrm{s}$ for $q = 2\pi \times 9.4\,\mathrm{Hz}$ and $-4.6\,\mathrm{Hz}$. This signalizes a faster loss of phase coherence in the system. This is further stressed in the inset, where we plot the evolution of $\langle F_\perp\rangle$ for representative values $q = 2\pi \times \{0.4, 2.4, 7.4\}\mathrm{Hz}$ together with the corresponding fits. There, we observe that the transverse spin fully vanishes already after $5\,\mathrm{s}$ of evolution for the largest displayed q-value.

This trends seems plausible, since spin-changing collisions enable population redistribution between the central and the side modes and facilitate mean field ground states with finite transverse spin for $|q|/|\lambda_1| < 2$. This is directly noticeable after solving for the fixpoint $(\dot\rho_0, \dot\theta_0) = (0,0)$ of the equations of motion in Eq.(2.17), which yields $(\rho_0^{\mathrm{FP}}, \theta_s^{\mathrm{FP}}) = (\frac{1+q/2|\lambda_1|}{2}, 0)$ for $|q| < 2|\lambda_1|$. This corresponds to a ground state with finite transverse spin length:

$$\langle F_\perp^{\mathrm{FP}}\rangle = \begin{cases} 2\sqrt{\rho_0^{\mathrm{FP}}(1-\rho_0^{\mathrm{FP}})}\cos(\frac{\theta_s^{\mathrm{FP}}}{2}) = \sqrt{(1+\frac{q}{2|\lambda_1|})(1-\frac{q}{2|\lambda_1|})} & , \ |q| < 2|\lambda_1| \\ 0 & , \ |q| > 2|\lambda_1| \end{cases} \tag{5.1}$$

The ground state spin length is maximized at $\langle F_\perp^{\mathrm{FP}}\rangle = 1$ for $q = 0$. Hence, it seems plausible that close to this value spin-changing collisions dynamically build up coherences and compete with the processes driving the decoherence in the system.

Additionally, we have studied the evolution of the transverse spin for different initial atom numbers ranging from $N \approx 10000$ to 30000 and observed comparable maximal life-times around $T_{\mathrm{LT}} \approx 14\,\mathrm{s}$ close to $q \approx 0$. For these measurements, we adjusted the initial atom number by transferring different fractions $|1, -1\rangle \to |1, 0\rangle$ during the preparation and cleaning the remaining atoms in $|1, -1\rangle$ using a Stern-Gerlach pulse rather than tuning the evaporation threshold. Thereby we intend to keep the initial condensate fractions comparable.
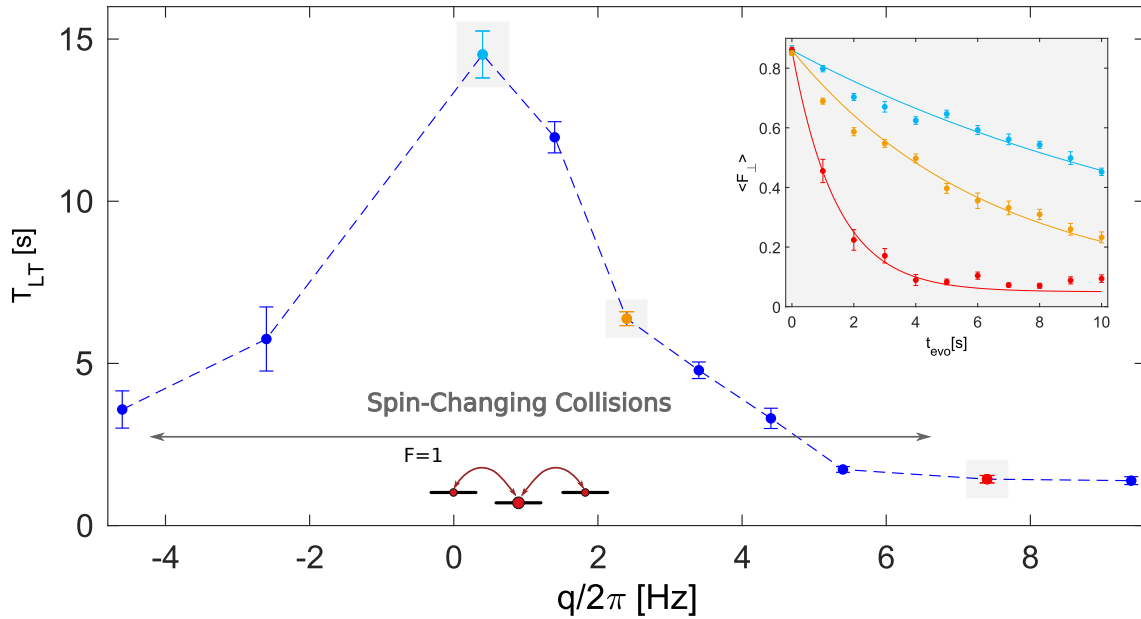
Figure 5.2.: **Life-time of the average transverse magnetization $\langle F_\perp \rangle$ for different values of q.** We prepare states with $\langle F_\perp(0) \rangle = 0.85$, N$\approx 19000$ atoms and use exponential fits to estimate the $\frac{1}{e}$ life-time T_{LT} of $\langle F_\perp \rangle$. We plot T_{LT} (blue points) for different values of the detuning q. The error bars represent the 1σ fit error. We observe that the life-time is maximized around $q = 2\pi \times 0.4$ Hz within the q regime displaying spin-changing collisions and drastically reduced for both larger and smaller values. The inset displays representative $\langle F_\perp \rangle$ evolutions for $q = 2\pi \times \{0.4, 2.4, 7.4\}$ Hz with the corresponding exponential fits (solid lines). While a significant spin survives after ~ 10 s for $q = 2\pi \times 0.4$ Hz, it fully vanishes already after 5 s for $q = 2\pi \times 7.4$ Hz indicating a faster decoherence. This seems plausible, since spin-mixing might dynamically build up coherences and compete with the processes responsible for the decoherence.

5.3. Controlling and Diagnosing Heating

So far, we have assumed that atom loss and finite temperature effects do not significantly affect the spin dynamics in BEC even after long evolution times on the order of $\sim 10\,$s. Here, we want to take a closer look at the latter and study the interplay between heating of the condensate density and the long-time spin dynamics. We start this section by presenting analysis tools to assess and compare heating in our system. Afterwards, we examine the heating for different trapping configurations and find experimental settings where it is substantially reduced.

5.3.1. Heating Analysis

In order to quantify the heating in our system, we resort to the theoretical framework for interacting condensates at finite temperature presented in section 2.3. Within this approach, the thermal cloud is displaced towards the flanks of the trap due to repulsive interactions with the denser condensate which predominantly occupies the central region of the trap.

We can not accurately assess the condensate and thermal fractions in-situ since the spatial extension of the condensate is small: The typical longitudinal Thomas-Fermi radii $R_{||} \approx 10\,\mu$m are not even an order of magnitude larger than the $\sim 1.2\,\mu$m imaging resolution. Moreover, we can not perform proper time of flight measurements with the current imaging setup since already after $t_{\exp} \approx 5\,$ms of free expansion a significant part of the cloud falls out of the field of view of the camera, especially after Stern-Gerlach separation of the individual magnetic sub-levels. Therefore, we settle for an intermediate approach and rapidly switch off the transverse confinement such that the atomic cloud expands in the remaining potential of the waveguide trap $(\omega_\perp, \omega_{||}) = (220, 46)$Hz $\rightarrow (220, 2.2)$Hz for short expansion times $t_{\exp} = 10\,$ms in comparison to $2\pi/\omega_{||}(t > 0) \approx 450\,$ms.

We expect the condensate cloud to expand in a self-similar fashion after this confinement quench, if the Thomas-Fermi approximation is still valid and if the trapping potential remains harmonic. The condensate retains a 3D parabolic shape and the relevant length scales of the system, such as the Thomas-Fermi Radii $R_j(t) = \lambda_j(t)R_j(0)$, are scaled by time dependent factors $\lambda_j(t)$ which fulfill coupled differential equations [Cas96]:

$$\ddot{\lambda}_j(t) = \frac{\omega_j(0)}{\lambda_j(t)\prod_k \lambda_k(t)} - \omega_j^2(t)\lambda_j(t) \tag{5.2}$$

with $j, k \in \{x, y, z\}$. Inserting the relevant parameters for the quench of the trapping potential $(\omega_{||}(0), \omega_{||}(t > 0)) = (46, 2.2)$Hz and $\omega_\perp(t > 0) = \omega_\perp(0) = 220\,$Hz , we obtain a longitudinal scaling factor around $\lambda_{||}(10\text{ms}) \approx 4$ after solving the equations of motion numerically. This is compatible with the observations in Fig.5.3.

In the case of the thermal component, it is not clear a priori how it exactly expands after we quench the transverse trapping potential and whether it significantly affects the dynamics of an expanding condensate at finite temperatures and short expansion

5. Decoherence and Heating

times[2].

We are primarily interested in *assessing and comparing the heating* in our system for different experimental settings rather than performing precise thermometry of our system. Hence, we make the simplifying assumption that both the thermal and condensate clouds *expand self-similarly* for small expansion times retaining the form of the corresponding in-situ density profiles. This assumption seems sensible at least for $T \leq 100\,\mathrm{nK}$ and typical longitudinal Thomas-Fermi Radius $R_{||} \approx 12\,\mu\mathrm{m}$: The self-similar expansion of the condensate $\Delta R_{\mathrm{ss}} = [\lambda_{||}(t_{\mathrm{exp}}) - 1]R_{||} \approx 40\,\mu\mathrm{m}$ exceeds the estimated thermal expansion $\Delta R_{\mathrm{T}} = \sigma_v(T)t_{\mathrm{exp}} \leq 15\,\mu\mathrm{m}$ after $t_{\mathrm{exp}} = 10\,\mathrm{ms}$. For the thermal expansion, we assume a Maxwell-Boltzmann velocity distribution with standard deviation $\sigma_v(T) = \sqrt{k_B T/m}$. Moreover, the potential energy dominates over the kinetic energy of the BEC with $E_{\mathrm{int}}/E_{\mathrm{kin}} \approx Na/[\lambda_{||}(t_{\mathrm{exp}})a_{\mathrm{HO}}] \approx 10$ for $N \approx$ 12000 atoms even after the expansion process supporting also the Thomas-Fermi approximation. We use $\lambda_{||}(10\mathrm{ms}) \approx 4$.

Experimentally, we record 1D density profiles $n(x)$ which are integrated along the two transverse directions of tight confinement $\omega_\perp$, either indirectly by the absorption imaging or explicitly during the evaluation. We cast the profiles for the thermal and condensate 1D density in Eqs.(2.29) and (2.28) into a *bimodal fit* of the form $n^{\mathrm{fit}}(x) = n_{\mathrm{C}}^{\mathrm{fit}}(x) + n_{\mathrm{T}}^{\mathrm{fit}}(x)$:

$$
n_{\mathrm{T}}^{\mathrm{fit}}(x) = B' \begin{cases} \sum_{k=1}^{8} \exp\left(-C'[(x-x_0')^2 - R'^2]\right)/k^{5/2} & \text{if } |x - x_0'| > R' \\ \\ \sum_{k=1}^{8}\{2 - \exp\left(-C'[R'^2 - (x-x_0')^2]\right)\}/k^{5/2} & \text{if } |x - x_0'| < R' \end{cases}
$$

$$(5.3)$$

$$
n_{\mathrm{C}}^{\mathrm{fit}}(x) = \begin{cases} 0 & \text{if } |x - x_0'| > R' \\ A'\left[1 - \left(\frac{x-x_0'}{R'}\right)^2\right]^2 & \text{if } |x - x_0'| < R' \end{cases}
$$

where $\{A', B', C', R', x_0'\}$ are independent fit parameters. The two last ones reflect the Thomas-Fermi Radius after the expansion and the central position of the condensate respectively. We use the first eight terms of the series expansion in order to fit the thermal part and estimate the condensate fraction in our system as $N_C/N \approx \sum_x n_{\mathrm{C}}^{\mathrm{fit}}(x) / \sum_x \left[n_{\mathrm{C}}^{\mathrm{fit}}(x) + \sum_x n_{\mathrm{T}}^{\mathrm{fit}}(x)\right]$.

We also take a closer look at the *statistical uncertainty* of this fitting procedure. The scaling of fluctuations of the estimated condensate fraction with the number of images averaged beforehand suggests that the method is limited by white-noise affecting the density profiles. Moreover, the statistical uncertainty of the estimated condensate fraction is reduced to values on the order $\sigma \leq 1\%$ by averaging over ≥ 20 identical realizations before fitting the mean density profiles. More details concerning this analysis can be found in Fig.A.5 in the appendix. At this stage we can not assess the impact of systematic errors since we have not yet computed theoretical expectations for the heating in our condensate.

---

[2]There is experimental evidence that the expansion rate of a condensate in free space decreases at higher temperatures as the increasingly large thermal cloud might dynamically compress the condensate while expanding [Zaw08].

5.3.2. Heating For Different Trapping Configurations

Once we have developed a method to assess the heating by examining the density profiles, we turn to relevant experimental configurations. Specifically, we adjust the power of the waveguide trapping beam and expect the heating rates to increase for higher powers as the scattering rate of trap photons also increases.

Both the maximal trapping depth V and the transverse trapping frequency $f_\perp$ depend on the beam power, which we tune to obtain the operating frequencies $f_\perp \approx \{150, 170, 220, 260\}$Hz [3]. Taking into account the gravitational sag and assuming a focused beam, these frequencies correspond to maximal trap depths on the order of $V = h \times \{56, 62, 84, 107\}$kHz in vertical direction. We extract these values from a previous calibration presented in [Str16]. The smallest confining trap depth in the presence of gravity is approximately $V_{\min} \approx h \times 50$ kHz.

As previously mentioned, higher trapping powers give rise to larger spontaneous scattering rates $\Gamma_{\rm sc}$ of trap photons. We can estimate the associated heating rate from $\Gamma_{\rm sc}$ and the recoil temperature $T_{\rm rec}$ [Gri00]:

$$\dot{T} = \frac{2}{3}T_{\rm rec}\Gamma_{\rm sc} = \frac{2}{3}\left(\frac{4\pi^2\hbar^2}{2mk_B\lambda^2}\right)\left(\frac{\Gamma V}{\hbar\Delta_{\rm eff}}\right) \tag{5.4}$$

The wavelength of the waveguide beam is $\lambda = 1030$ nm and the spontaneous decay rate of the excited state for the D-line transition is $\Gamma \approx 2\pi \times 6$ MHz. The effective detuning $\frac{1}{\Delta_{\rm eff}^2} = \frac{2}{\Delta_1^2} + \frac{1}{\Delta_2^2}$ is determined by the detuning $\Delta_{1,2}$ of the waveguide beam with respect to the $D_{1,2}$ line. For the studied trapping depths $V = h \times \{56, 62, 84, 107\}$Hz, we estimate heating rates on the order of $\dot{T} = \{1.3,\ 1.4,\ 1.9,\ 2.5\}\frac{\rm nK}{\rm s}$.

We prepare condensates of $N \approx 12000$ atoms and estimate the condensate fraction for the different trapping configurations $f_\perp \approx \{150, 170, 220, 260\}$Hz within $t_{\rm evo} \leq 15$s of evolution using the bimodal fits introduced in Eq.(5.4). We average over ~ 50 independent realizations and present the experimental mean density profiles together with the bimodal fits in Fig.5.3. We observe substantial differences between the different settings: For the two shallower trapping configurations $f_\perp = \{150, 170\}$Hz in (a) and (b), the density profiles develop only minimal thermal wings after long evolution times and seem to be primarily affected by atom loss. This behavior is further stressed by the individual fits of the thermal and condensate fractions for $t_{\rm evo} = 0$ and 15 s. By contrast, the density profiles for the tighter confinements $f_\perp = \{220, 260\}$Hz in (c) and (d) exhibit substantial heating and develop a significant thermal component within the same window of evolution times.

We perform now a more systematic comparison of the heating for the different trapping configurations. We extract the condensate fractions from the respective fits and plot them in Fig.5.1(a) for different transverse confinements $f_\perp$. The two shallower trap settings $f_\perp = \{150, 170\}$Hz exhibit only *minimal heating* as the estimated condensate fraction minimally changes $N_{\rm C}/N \approx 0.95 \rightarrow 0.86\text{-}0.9$. By contrast, the tighter configurations exhibit *substantially larger heating* as the condensate fraction is reduced to $N_{\rm C}/N \approx \{0.53, 0.09\}$ after 15 s for $f_\perp = \{220, 260\}$Hz.

---

[3]These values are experimentally calibrated by displacing the cloud from the trap center and monitoring the subsequent oscillations of the BEC center of mass.
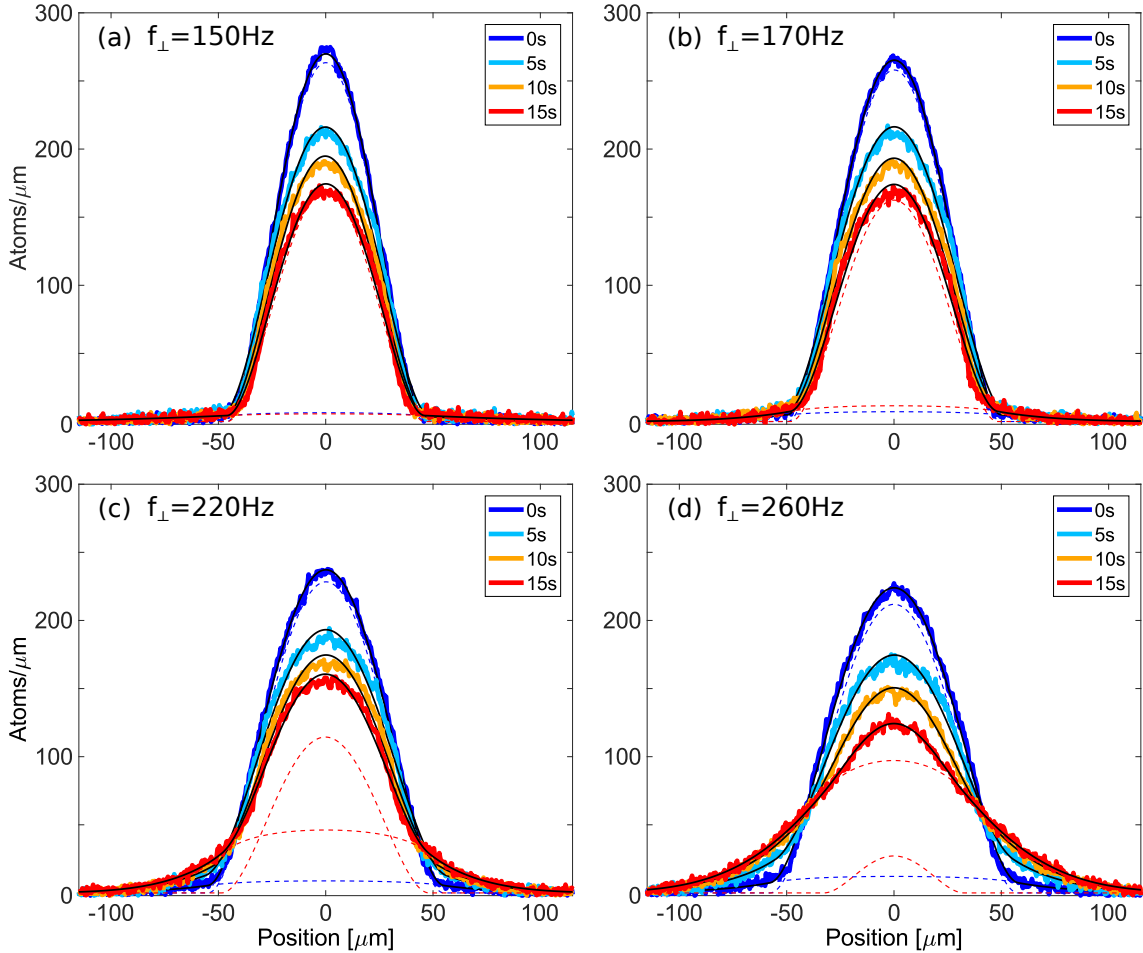
Figure 5.3.: **Evolution of 1D density profiles for different trapping configurations**. We average over ~ 50 realizations and plot the mean 1D integrated density profiles for $t_{\mathrm{evo}} \leq 15\,\mathrm{s}$ and transverse trapping frequencies $f_\perp \approx \{150, 170, 220, 260\}\mathrm{Hz}$ **(a)-(d)** after $t_{\mathrm{exp}} = 10\,\mathrm{ms}$ of expansion in the waveguide trap. For the two shallower confinements (a,b), we observe that the profiles (colored lines) develop only minimal thermal wings within $t_{\mathrm{evo}} \leq 15\,\mathrm{s}$. This is also captured in the bimodal fits (black lines) and the individual fits of the thermal and condensate fractions (dashed lines) at 0 and 15 s. By contrast, the tighter trapping configurations (c,d) seem to be considerably affected by heating as we directly observe in the late-time profiles. The trapping frequencies are tuned by adjusting the power of the waveguide beam.
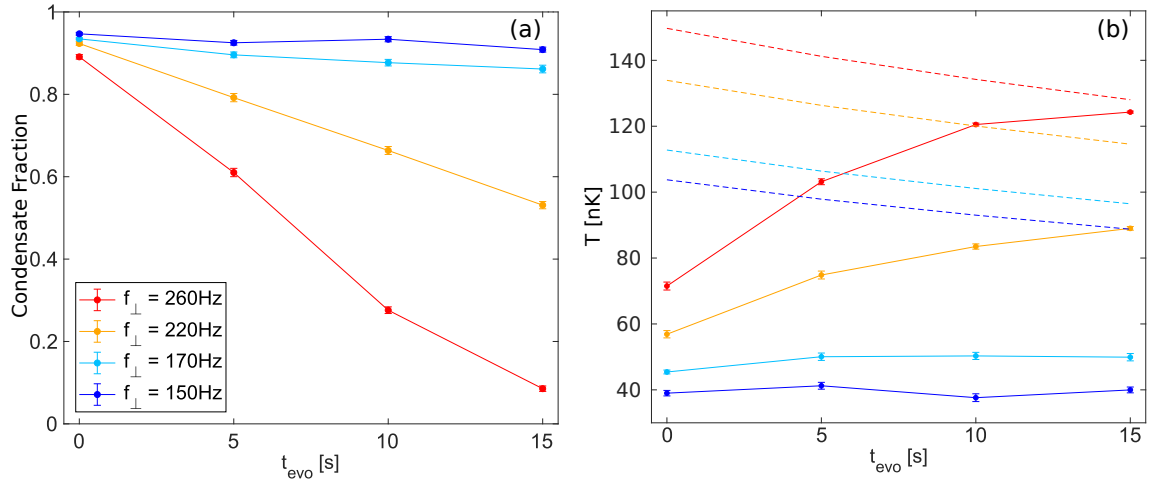
Figure 5.4.: **Heating for different trapping configurations**. We plot the evolution of the condensate fraction for settings with different transverse trapping frequencies $f_\perp$ **(a)**, which is estimated using the fits displayed in Fig.5.4. The error bars reflect the 1σ fit error. For the two shallower trapping configurations (blue tones), we prepare a nearly pure condensate with $N_C/N \approx 0.95$ and the condensate fraction is only minimally reduced to $N_C/N \approx 0.86$-0.9 within 15 s. Meanwhile, the condensate fraction is substantially reduced in the same time window for tighter confinements (orange, red). We estimate the evolution of the temperature **(b)**, where we take into account that the critical temperature T_c (dashed lines) is reduced dynamically due to atom loss. We conclude that heating of the BEC density is minimal for the two shallower trap settings with $\Delta T \lesssim 5\,\text{nK}/15\,\text{s}$, but considerably larger for the tighter ones.

For the sake of completeness, we also estimate the temperature evolution from the condensate fractions using Eq.(2.27) and plot the results in Fig.5.4(b). We take into account that the critical temperature is larger for the tighter trapping configurations and also dynamically reduced due to atom loss (dashed lines). We observe that the two shallower trapping settings exhibit only minimal heating around $\dot{T} \leq 4\,\text{nK}/15\text{s}$, while the two tighter ones substantially heat with 32nK/15s ($f_\perp = 220\,\text{Hz}$) and 53nK/15s ($f_\perp = 260\,\text{Hz}$).

The negligible heating for shallower trapping configurations is probably due residual evaporation of hot atoms during evolution. This is plausible, since the estimated trapping depths $V \approx h \times \{56, 62\}\text{kHz}$ are close to the minimal one $V_{\min} = h \times 50\,\text{kHz}$ required vertically confine the atoms [Str16]. This is further supported by the larger atom loss rates shown in Fig.A.4 in the appendix. For the tighter trapping settings $f_\perp \approx \{220, 260\}\text{Hz}$, the experimental heating rates estimated within the first 5 s of evolution are around $\dot{T} \approx \{3.6, 6.3\}\frac{\text{nK}}{\text{s}}$. While these values are larger than the heating rates associated to incoherent scattering of trap photons $\dot{T} = \{1.9, 2.5\}\frac{\text{nK}}{\text{s}}$, the orders of magnitude coincide indicating that this is most likely the foremost heating mechanism. Additional heating might arise due to scattering of photons from the vertical trap beam or due to spatial and temporal power

fluctuations corresponding lasers. However, we can not exclude that our fitting routine systematically underestimates the condensate fraction.

5.4. Impact of Heating on the Long-Time Spin Dynamics

Once we have examined the heating in our system and observed a dependence on the trapping configuration, we can return to the spin dynamics and examine whether the long-term decoherence is correlated to the heating rate in our system.

We use exactly the same dataset as in the previous section with $N(0) \approx 12000$ atoms and $\langle F_\perp(0) \rangle \approx 1$. The detuning q is adjusted to a small value $q \approx 2\pi \times 0.5\,\mathrm{Hz}$ in order to ensure maximally large transverse spin life-times. This roughly corresponds to mean field ratios in the range $q/|\lambda_1| \approx 0.15$ - 0.25 depending on the particular trapping configuration.

We examine the evolution of the mean and standard deviation (error bars) of the transverse spin within $t_{\mathrm{evo}} \leq 15\mathrm{s}$ in Fig.5.5(a). We concentrate first on the evolution of the mean transverse spin $\langle F_\perp \rangle$ and observe a clear qualitative trend. For the shallower trapping configurations a significant transverse magnetization survives even after $15\,\mathrm{s}$ of evolution with $\langle F_\perp(15\,\mathrm{s}) \rangle \approx 0.56$ for $f_\perp = 150\,\mathrm{Hz}$, whereas in the case of tighter confinement we observe rather small values around $\langle F_\perp(15\,\mathrm{s}) \rangle \approx 0.11$ for $f_\perp = 260\,\mathrm{Hz}$. The latter is compatible with zero average transverse spin since applying the F_x-F_y readout to a polar state yields $\langle F_\perp \rangle \approx 0.10 \pm 0.02$.

While the initial fluctuations are comparably small for all settings $\sigma_{F_\perp}(0) \approx 0.02$, they clearly differ at later times. For the settings exhibiting minimal heating with $f_\perp = \{150, 170\}\mathrm{Hz}$, the fluctuations steadily increase with t_{evo} and reach rather large late-time values around $\sigma_{F_\perp}(15s) \approx 0.17$ for $f_\perp = 150\mathrm{Hz}$. On the contrary, for the settings displaying larger heating with $f_\perp = \{220, 260\}\mathrm{Hz}$ the standard deviation peaks within the first $5\,\mathrm{s}$ of evolution and is significantly reduced afterwards to values around $\sigma_{F_\perp}(15s) \approx 0.04 - 0.08$.

Due to this qualitative difference, we take a closer look at the late-time fluctuations and plot the average transverse spin after $15\,\mathrm{s}$ (circles) together with the individual realizations (squares) for the corresponding trapping frequencies in Fig.5.5(b). For the setting with the largest heating rate $f_\perp = 260\,\mathrm{Hz}$ the individual realizations explore only a small range of transverse spins $F_\perp \in \{0, 0.22\}$. As not only the mean transverse spin but also the single realization values nearly vanish, this further stresses that the system undergoes late-time *decoherence*. If we reduce the trapping frequencies to $f_\perp = \{150, 170\}\mathrm{Hz}$ and mitigate thereby the heating, the spread of individual realizations is considerably larger. We conclude, that the decoherence is significantly reduced at comparable timescales as single realizations explore also large spin length values up to $F_\perp \leq 0.9$ for $f_\perp = 150\,\mathrm{Hz}$. The large spread originates most likely from the *dephasing* of the spin dynamics due to the combined influence of quantum and experimental fluctuations. This will be studied both theoretically and experimentally in the next chapter.
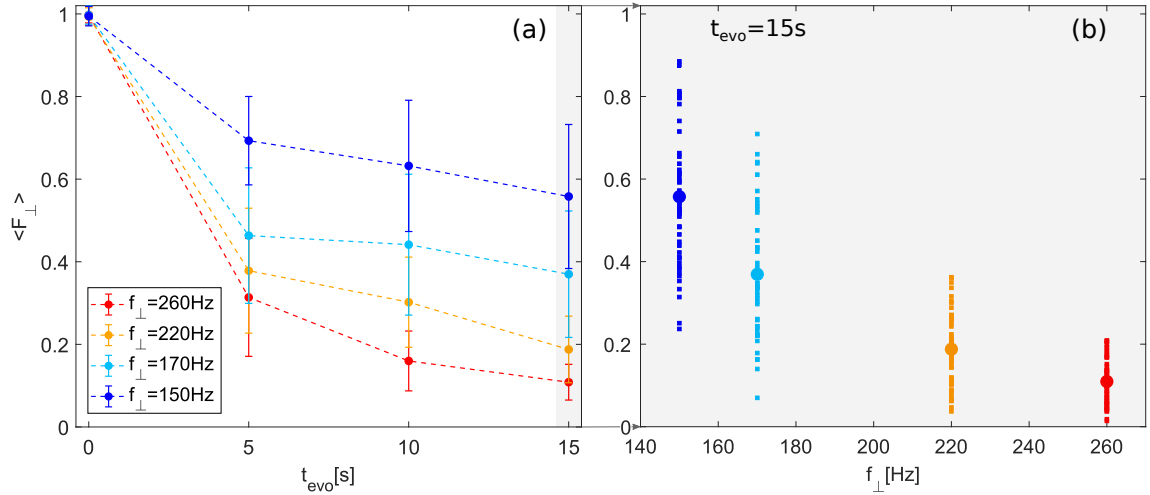
Figure 5.5.: **Evolution of transverse spin for different trapping configurations.** We prepare initial states with $N \approx 12000$ atoms and $\langle F_\perp(0) \rangle = 1$. We average over ~ 50 realizations and plot the evolution of $\langle F_\perp \rangle$ with the corresponding standard deviations (error bars) for settings with different transverse trapping frequencies $f_\perp$ **(a)**. We observe a faster decay of $\langle F_\perp \rangle$ for the tighter trapping settings. The fluctuations are initially comparably small but clearly differ at later times: For the shallower confinements (light blue and blue), they steadily increase, while for the remaining cases (red and orange bars) they are maximized within $\leq 5\,\mathrm{s}$ and decrease afterwards. Additionally, we plot $\langle F_\perp \rangle$ (circles) together with the individual realizations (squares) after $15\,\mathrm{s}$. The tightest trapping configuration exhibits only small fluctuations around $\langle F_\perp \rangle \approx 0.11$, indicating that the system loses coherence. By contrast, for shallower settings the spread is considerable and individual realization reach large values up to $F_\perp \leq 0.9$. Hence, the system retains long-term coherence for these configurations which also exhibit minimal heating.

Summary and Conclusions

We observe a long-time decay of the average transverse magnetization indicating the progressive loss of coherences in our system. Afterwards, we examine the impact of the detuning q on this process and observe the following behavior:

- The life-time of the transverse spin is maximized within the q-regime exhibiting spin-changing collisions and is on the order of $T_{\text{LT}} \approx 14\,\text{s}$ for $\frac{q}{2\pi} \approx 0.5\,\text{Hz}$ and $\frac{\lambda_1}{2\pi} \approx -3\,\text{Hz}$. The transverse trapping frequency is here $f_\perp = 220\,\text{Hz}$.

- The life-time is substantially reduced for both larger and smaller q values, indicating that the decoherence is accelerated in the system.

Small q values on the order $|q| < 2|\lambda_1|$ give rise to spin-changing collisions which favor mean field ground states with finite transverse magnetization. Hence, it seems plausible that spin-mixing also coherently builds up transverse magnetization during the evolution and partially counteracts the processes driving the decoherence. Additionally, we systematically study how heating of cloud the density impacts the late-time evolution of the transverse spin. For this purpose, we adjust the waveguide trap power and thereby the transverse trapping frequency $f_\perp$. We assess the heating for different configurations using bimodal fits to estimate the evolution of the condensate fraction:

- Shallower trapping settings $f_\perp = \{150, 170\}\text{Hz}$ exhibit only minimal heating as the extracted condensate fractions minimally change in a time scale of $15\,\text{s}$ $\frac{N_{\text{C}}}{N} = 0.95 \rightarrow 0.86\text{-}0.9$, most likely due to residual evaporation during evolution.

- By contrast, tighter trapping configurations with $f_\perp = \{220, 260\}\text{Hz}$ display substantially larger heating within the same time window as $\frac{N_{\text{C}}}{N} = \{0.95, 0.9\} \rightarrow \{0.53, 0.09\}$. The higher heating rates primarily originate from larger spontaneous scattering rates of trap photons.

These two types of settings exhibit a disparate late-time spin dynamics:

- For configurations with larger heating, the average transverse spin significantly decays within $15\,\text{s}$ and the fluctuations of individual realizations are small, indicating the progressive loss of coherences in the system.

- By contrast, for settings with minimal heating a significant mean transverse magnetization survives even after $15\,\text{s}$ of evolution. Together with the larger spread of individual realizations, this behavior indicates that the system retains long-time coherence.

In conclusion, we observe a correlation between the late-time internal spin dynamics and the temperature of motional degrees of freedom as the observed heating affects the density profiles. Moreover, we also realize that we should not restrict ourselves to the evaluation of expectation values but also examine fluctuations, individual realizations and the underlying distributions in order to appropriately characterize state of the system at late times. Having this in mind, we can proceed to the last chapter.

6. Long-Time Spin-1 States

In this final chapter, we want to further characterize late-time spin dynamics and the underlying spin-1 states for settings displaying different heating rates, in order to disentangle the role of finite temperature effects. We concentrate again on evolution times up to $t_{\mathrm{evo}} \sim 10\,\mathrm{s}$ which are large in comparison to the timescales associated with the internal spin dynamics $|q|$ and $|\lambda_1| \sim 2\pi \times 2\,\mathrm{Hz}$. Within these long evolution times, we lose $\sim 30\%$ of the atoms and the condensate significantly heats depending on the specific trapping configuration.

Throughout this section we examine a complementary observable, the normalized population ρ_0 in the central mode $|1, 0\rangle$. We extract this quantity at shot-noise limit [Mue13] by means of state selective absorption imaging. This observable is suitable to characterize late-time spin states since the extraction of ρ_0 is not affected by long-term B-field fluctuations as in the case of the F_x-F_y readout.

We start this chapter by discussing potential mechanisms influencing the spin dynamics at these timescales. In this context, we emphasize the role of dephasing relying on Truncated Wigner simulations and discuss also a qualitatively distinct dissipative relaxation of the spin dynamics. Afterwards, we turn to experimental settings exhibiting minimal and substantially larger heating and study the associated spin dynamics. We examine first the oscillations of the mean central mode population and the characterize the observed damping. Later, we focus on longer timescales around $\sim 10\,\mathrm{s}$, investigate also the evolution of fluctuations and observe contrasting long-term behaviors for both settings. In order to further assess the relevant processes affecting the dynamics, we investigate the impact of different initial conditions on the late-time fluctuations and the underlying distribution functions.

6.1. Relevant Processes and Long-Time Scenarios

Before presenting experimental results, we want to elucidate potential processes influencing the spin dynamics and determining the long-time behavior of the system. First, we discuss the *dephasing* of the internal dynamics due to quantum and experimental fluctuations relying on our Truncated Wigner simulations. In this context, we introduce a procedure to additionally incorporate experimental q fluctuations on our simulations. Moreover, we also qualitatively consider a disparate long-time *dissipative relaxation* in the presence of decoherence. We identify distinctive signatures of these two scenarios related to the late-time fluctuations of ρ_0.

Dephasing

In accordance to the *Truncated Wigner simulations* (TW) presented in chapter 4, we expect the spin dynamics to experience dephasing because of the intrinsic quantum
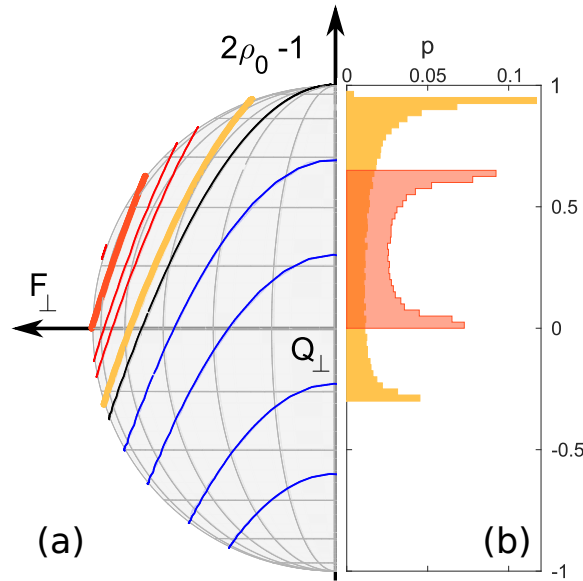
Figure 6.1.: **Dephasing: Impact of initial oscillations on long-time fluctuations (sketch)**. In accordance to our TW simulations, we expect the late-time states to fully spread along the associated trajectories (orange lines) on the spin-nematic sphere **(a)** due to the influence of dephasing. Projecting the associated state into the $2\rho_0 - 1$ axis **(b)** results in double-peaked distributions. We expect the width of these histograms (late-time fluctuations) to increase with the amplitude of the initial oscillations. We identify this as a distinctive signature of dephasing.

fluctuations: The fluctuating spin-1 state spreads and eventually fully delocalizes along the corresponding mean field trajectory in the spin-nematic sphere due to the underlying non-linear equations of motion as we see in Fig.4.1. For typical experimental parameters, this results in damped oscillations of the mean central mode population $\langle \rho_0 \rangle$ in a timescale on the order of $\sim 15\,\mathrm{s}$ (see Fig.4.1).

In such a dephasing dominated scenario, we expect also distinctive signatures for *late-time fluctuations* and the underlying ρ_0 *distributions*. The expected behavior is schematically represented in the spin-nematic sphere for two representative trajectories n Fig.6.1(a): As the state spreads along the corresponding trajectories (orange lines), we expect ρ_0 fluctuations to increase and eventually saturate. By measuring ρ_0, we project these delocalized states into the vertical axis of the sphere obtaining characteristic double-peaked histograms in (b). This particular shape arises from the fact that ρ_0 is more likely to be measured close to extremal values as the population dynamics is decelerated nearby. In particular, we expect also that the spread of the late-time distributions increases with the size of the phase space region sampled by the initial dynamics or equivalently with the amplitude of the short-time oscillations, as schematically represented in Fig.6.1 for two initial conditions.

As previously mentioned, we expect the spin dynamics to exhibit significant dephasing only after $\sim 15\,\mathrm{s}$, if the evolution is subjected solely to quantum fluctuations. However, we observe a significant damping of the oscillations within few seconds of
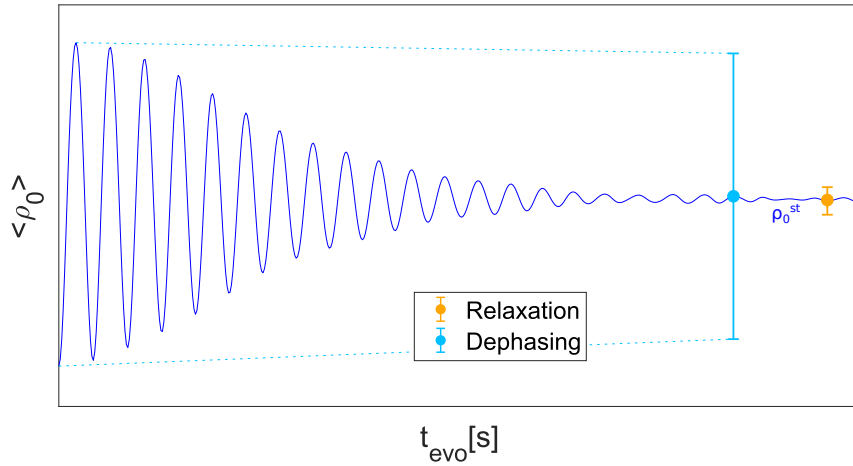
Figure 6.2.: **Expected late-time fluctuations for dephasing and dissipative relaxation of the spin dynamics (schematic representation)**. In both scenarios, we expect that average values of observables like $\langle \rho_0 \rangle$ (blue line) oscillate and damp to a stationary value ρ_0^{st}. Nevertheless, we expect distinctive signatures when probing the late-time fluctuations: In the case of a dissipative relaxation (orange error bar) we expect the individual realizations to minimally fluctuate around ρ_0^{st} independently of the particular initial condition. By contrast, in the case of dephasing (light blue error bar) we expect the fluctuations to be larger and directly depend on the amplitude of the initial oscillations.

evolution even for minimal heating as later shown in Fig.6.3(a). Since this setting retains long-term coherence, we attribute the accelerated damping to additional fluctuations of experimental parameters. Throughout this chapter, we explicitly incorporate fluctuations of the detuning q to our simulations: For each run of the simulation, we sample additional Gaussian noise δq from a normal distribution with standard deviation Δq and solve the equations of motion for a different detuning value $q + \delta q$. We expect them to primarily originate from the power stabilized microwave dressing with $\Delta q \approx 2\pi \times 0.2\,\text{Hz}$ [Kun18b]. The fluctuations associated with the estimated B-field stability are an order of magnitude smaller $\Delta q_B \approx 2\pi \times 0.01\,\text{Hz}$ and therefore negligible.

Dissipative Relaxation

In the previous chapter, we observed a steady decay of the transverse spin for settings exhibiting larger heating of the BEC density. This indicates the progressive loss of coherences in the system. In such a scenario, we expect additional processes to impact the spin dynamics. An exact theoretical treatment requires to consider the interactions between a growing thermal fraction and the condensate atoms occupying each one of the magnetic sub-levels [End11]. Here, we provide only a phenomenological picture for the expected behavior.

The progressive loss of coherences in the system obliterates the phase relation between the central and side modes. As quantities such as the spinor phase θ_s

become 'ill defined', coherent spin-mixing can not further take place in the system. Thus, we expect individual realizations of ρ_0 to display a *dissipative relaxation* and approach a stationary value ρ_0^{st}. As individual realizations relax, the oscillations of the mean $\langle \rho_0 \rangle$ automatically damp and converge towards ρ_0^{st}. Hence, we can not properly distinguish this process from dephasing solely by examining the late-time evolution of $\langle \rho_0 \rangle$.

Nevertheless, we expect late-time fluctuations of ρ_0 to behave distinctly in the presence of decoherence: Since in this case individual realizations are expected to relax, we expect late-time fluctuations to be reduced in comparison to an unimpaired dephasing scenario and not to appreciably depend on the particular choice for the initial condition $\rho_0(0)$. As schematically depicted in Fig.6.2, we expect the late-time fluctuations (orange) to be significantly smaller than in the case of dephasing (light blue error bar) and not directly depend on the amplitude of the initial oscillations.

6.2. Examining ρ_0 Dynamics

We characterize the late-time behavior by experimentally studying the evolution of the average and the fluctuations of ρ_0. In this context, we also compare the experimental observations with Truncated Wigner simulations in order to assess a potential dephasing scenario.

Specifically, we concentrate on studying the dynamics for settings with transverse trapping frequencies $f_\perp = 170\,\mathrm{Hz}$ and $f_\perp = 220\,\mathrm{Hz}$, since they exhibit significantly different heating rates as observed in Fig.5.4. Moreover, the atom-loss rates and cloud densities are closer than for the remaining settings examined in the previous chapter. We label them as *setting A* and *setting B* respectively and summarize the relevant experimental parameters in Tab.6.1. The temperature related values are retrieved from Fig.5.4 and the mean field parameters q and λ_1 are estimated by minimizing the deviation between experimental and theoretical ρ_0 oscillations. More details concerning this estimation are provided in Fig.A.6 in the appendix. The larger spin-spin interactions λ_1 for $f_\perp = 220\,\mathrm{Hz}$ are attributed to the larger peak density $n(0)$ of the BEC for comparable atom numbers N due to the tighter confinement.

Features	Setting A 'minimal heating'	Setting B 'substantial heating'
Transverse trapping frequency $f_\perp$ [Hz]	170	220
$(q, \lambda_1)/2\pi$ [Hz]	$(0.92, -1.91)$	$(1.5, -2.45)$
Fixpoint population ρ_0^{FP}	0.62	0.65
Initial atom number	12000	12000
Life-time in trap [s]	35.6 ± 0.5	45.2 ± 0.6
Heating rate [nK/15 s]	4	32
Initial temperature [nK]	45.5	57.5

Table 6.1.: **Experimental settings used for investigating the impact of heating on the spin dynamics.**
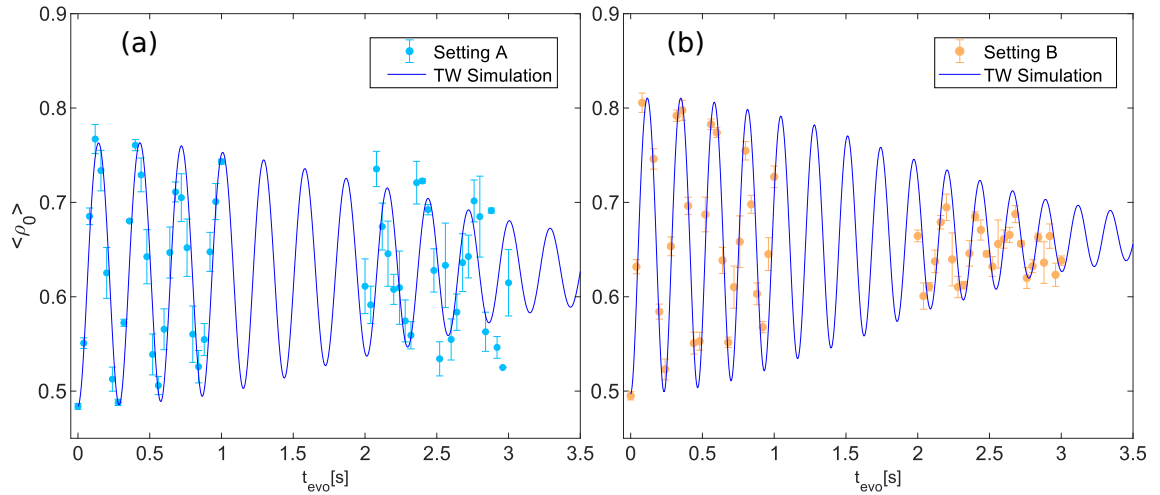
Figure 6.3.: **Mean ρ_0 oscillations for setting A, B and TW simulations**. We prepare initial states with $\rho_0(0) \approx 0.5$ and plot the evolution of $\langle \rho_0 \rangle$ within $t_{\text{evo}} \leq 3\,\text{s}$ for setting A **(a)** and B **(b)**. We average over 4 realizations and the error bars are the SEM. We observe observe oscillations for both settings with a slower damping for setting A. This setting also displays larger fluctuations after $t_{\text{evo}} > 2\,\text{s}$. Additionally, we plot the oscillations obtained from TW simulation (blue lines) incorporating shot-to-shot q fluctuations around $\frac{\Delta q}{2\pi} = 0.11\,\text{Hz}$. They reasonably reproduce the experimental oscillations and timescale of the damping.

6.2.1. Damping of Population Oscillations

We prepare initial conditions with $\rho_0(0) \approx 0.5$, average over ~ 4 realizations and plot the mean central mode population $\langle \rho_0 \rangle$ within $t_{\text{evo}} \leq 3\,\text{s}$ for setting A and B in Fig.6.3(a) and (b) respectively. For setting A, the mean central mode population oscillates with moderate amplitude ~ 0.12 and frequency $\sim 3.5\,\text{Hz}$. Moreover, the oscillations appreciably damp within the examined timescale and exhibit increasing fluctuations after $2\,\text{s}$. This is evidenced by the larger error bars and the increasing amount of outliers. Meanwhile, for setting B the average central mode population oscillates with slightly larger frequency $\sim 4.2\,\text{Hz}$ and amplitude ~ 0.15. This is attributed to the larger q and $|\lambda_1|$ values and to the system being initialized further away from the fixpoint (see Tab.6.1). Moreover, the oscillations seem to damp faster than for setting A and exhibit smaller fluctuations after $t_{\text{evo}} > 2\,\text{s}$. The smaller fluctuations at these intermediate timescales already suggest that this setting might be affected by additional dissipative processes.

At least for setting A the observed damping of $\langle \rho_0 \rangle$ is expected to primarily arise from dephasing, since in this case the system was observed to retain long-term coherence in the previous chapter (see Fig.5.5). In order to provide a theoretical reference, we carry out Truncated Wigner simulations with additional experimental noise Δq as described in section 6.1. We use the parameters listed in Tab.6.1, $S = 2500$ samples[1] and adjust the fluctuations to $\Delta q = 2\pi \times 0.11\,\text{Hz}$ in order

---

[1]Due to the enhanced fluctuations, we require larger sample sets to ensure numerical stability.

to appropriately capture the experimental damping time for setting A. The order of magnitude of the incorporated q fluctuations coincides with the independent estimation $\Delta q = 2\pi \times 0.2\,\mathrm{Hz}$ in [Kun18b]. The simulated ρ_0 oscillations (blue lines) are also plotted in Fig.6.3 and reasonably reproduce the experimental oscillations and damping times for both settings. In particular, we observe also a faster damping for the simulations for setting B. In this case, the system is initialized further away from the fixpoint and the individual mean field parameters q and $|\lambda_1|$ are larger (see Tab.6.1). This in turn results in more pronounced anharmonicieties and overall faster oscillations of the individual samples, which together accelerate the dephasing in the system. Additional measurements for q and λ_1 values closer to the ones for setting A are required in order to investigate if decoherence accelerates the damping time for setting B.

6.2.2. Long-Time Evolution

Evolution of Fluctuations of ρ_0

In this section, we want to shift our focus to larger evolution times on the order of $\sim 10\,\mathrm{s}$. After studying the evolution of $\langle\rho_0\rangle$ oscillations in Fig.6.3, we expect them to be to be fully suppressed within these longer timescales. Hence, the analysis of expectation values is not sufficient to characterize the late-time evolution of the system. Therefore, we focus on examining the evolution of ρ_0 fluctuations for settings with minimal and substantially larger heating. Additionally, we compare again the results to Truncated Wigner simulations in order to determine whether dephasing appreciably affects the dynamics.

As before, we prepare initial states with $\rho_0(0)\approx0.5$ and $\langle F_\perp(0)\rangle=1$ and plot the evolution of the variance σ^2 for setting A (a) and B (b) in Fig.6.4. Its statistical uncertainty is estimated using a jackknife resampling method [Mil74]. The fluctuations of the initial condition coincide for both settings and are on the order $\sigma^2 \sim 1/N$, whereas they clearly differ at later times. For setting A the variance increases significantly faster and is larger by an order of magnitude than for setting B already after 4 s of evolution. Moreover, the fluctuations exhibit different trends at later times. For setting B the fluctuations slowly increase up to 12 s but remain nearly an order of magnitude smaller, while they moderately decrease for setting A.

Additionally, we carry out TW simulations with $S = 2500$ samples and experimental noise $\frac{\Delta q}{2\pi} = 0.11\,\mathrm{Hz}$ and plot the corresponding evolution of the variance σ^2 also in Fig.6.4 (blue curves). The initial fluctuations are small and compatible with both experimental settings. At later times, the variances rapidly increase and saturates around $t_{\mathrm{evo}} \leq 5\,\mathrm{s}$. This saturation and the observed short-time variance oscillations in the simulations can be understood relying on the spin-nematic sphere: The individual samples spread along the corresponding mean field trajectories while oscillating at different frequencies due to the non-linear equations of motion. Hence, σ^2 oscillates approximately twice faster than $\langle\rho_0\rangle$ and exhibits local minima when the mean is extremal. This is also visible in the spin-nematic spheres discussed in Fig.4.1(c) in chapter 4. Moreover, the variance saturates after the individual samples fully dephase and delocalize on phase space. The residual late-time oscillations are attributed
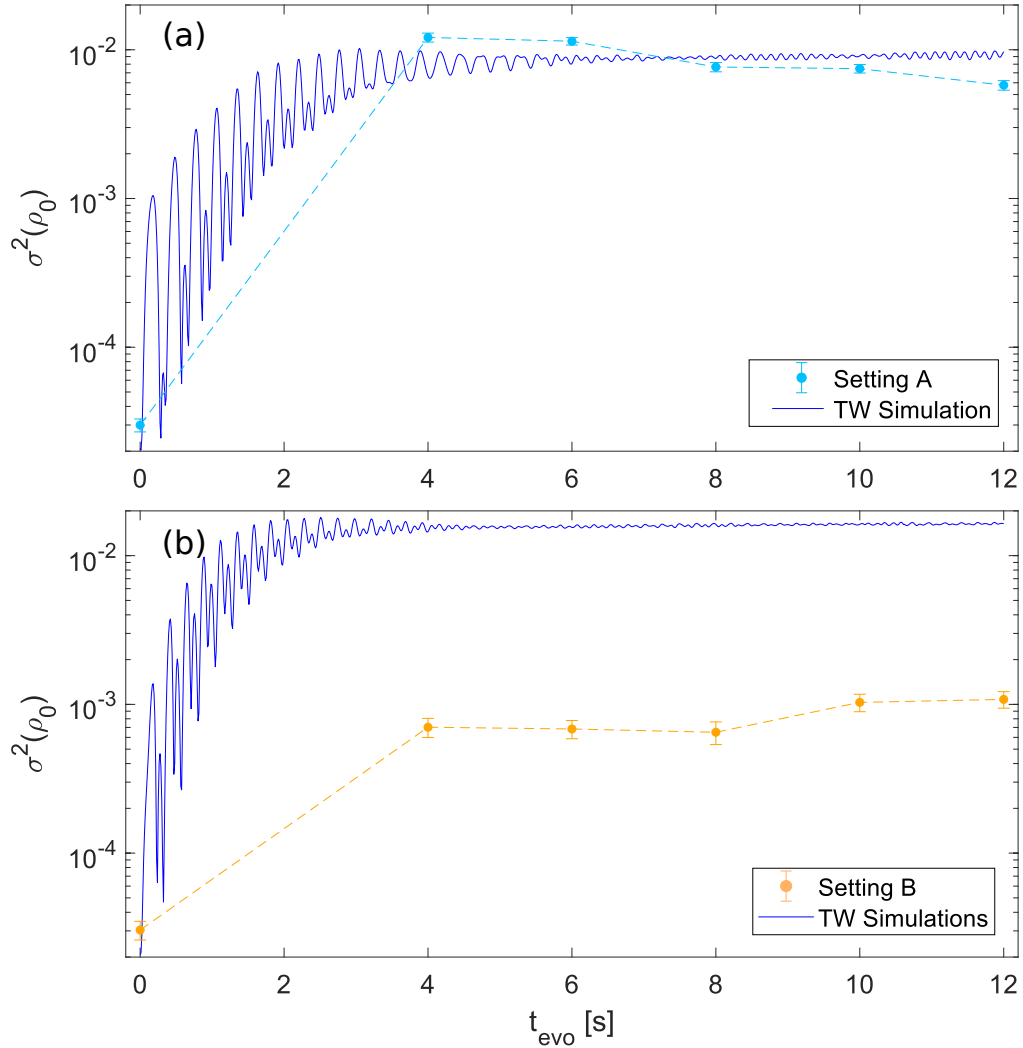
Figure 6.4.: **Evolution of ρ_0 variance for setting A, B and corresponding TW simulations.** We prepare initial states with $\rho_0(0) \approx 0.5$ and plot the variance evolution in a semi logarithmic scale suitable for comparing orders of magnitude. The error bars are obtained using a resampling method on the ~ 150 realizations per point [Mil74]. For setting A **(a)** the variance peaks within $t_{evo} \leq 4\,s$ and is slightly reduced afterwards. On the contrary, for setting B **(b)** it slowly increases within $t_{evo} \leq 12\,s$ but remains approximately one order of magnitude smaller. We also plot the variance evolution obtained from Truncated Wigner simulations (blue lines) incorporating shot-to-shot q fluctuations with $\frac{\Delta q}{2\pi} = 0.11\,Hz$. Due to the accelerated dephasing induced by these fluctuations, the variances saturate already after $\leq 5\,s$ of evolution. The corresponding stationary value is comparable to setting A especially for $t_{evo} \leq 8\,s$, but an order of magnitude larger than the late-time results for setting B.
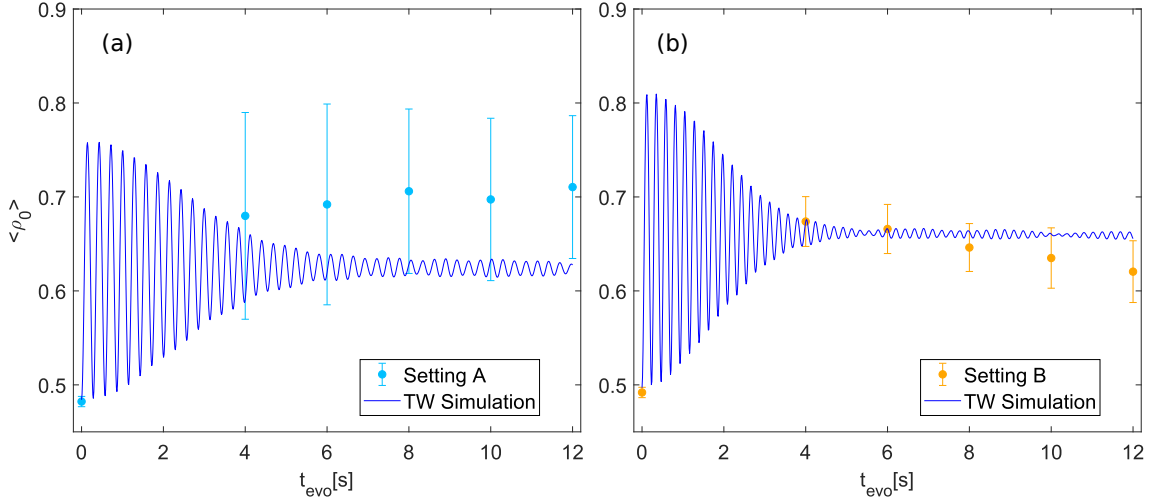
Figure 6.5.: **Late-Time evolution of $\langle \rho_0 \rangle$ for setting A, B and corresponding TW simulations (blue lines).** We prepare initial states with $\rho_0(0) \approx 0.5$ and plot the evolution of the mean central mode population $\langle \rho_0 \rangle$ within $t_{\text{evo}} = 12\,\text{s}$. The error bars reflect the standard deviation as previously discussed in Fig.6.4. For setting A **(a)**, $\langle \rho_0 \rangle$ drifts towards values larger than the corresponding TW simulation (blue lines), which can be partially accounted by the shift of the fixpoint position due to atom loss. By contrast, setting B **(b)** displays a late-time drift in the opposite direction contradicting a single-mode dephasing scenario.

numerical artifacts as the amplitude is smaller and the frequency fluctuates in time.

For setting A, the stationary variance obtained from these simulations is around $\sigma^2 \approx 0.01$ and comparable to the late-time fluctuations especially for $t_{\text{evo}} \leq 8\,\text{s}$. For later times, the experimental variance slightly decreases below the simulation results which is attributed to dissipative processes such as minimal heating and atom loss. Additional experimental points for $0 < t_{\text{evo}} < 4\,\text{s}$ are required in order to assess the short-time agreement. By contrast, for setting B the late-time variances are consistently an order of magnitude smaller than the saturated simulation value $\sigma^2 \approx 0.016$. It is important to emphasize, that reducing the q fluctuations in an attempt to better capture the timescale of the σ^2 increase would result in $\langle \rho_0 \rangle$ oscillations damping substantially slower. This would contradict the experimental observations in Fig.6.3(b). Moreover, since the q fluctuations primarily originate from the microwave dressing we expect them to be equal for setting A and B.

Evolution of $\langle \rho_0 \rangle$

For the sake of completeness, we plot also the corresponding late-time evolution of the average central mode population $\langle \rho_0 \rangle$ for both setting A (a) and B (b) together with the corresponding Truncated Wigner simulations (blue lines) in Fig.6.5. The error bars correspond to the standard deviation and directly capture the previously discussed fluctuations.

For setting A, we observe that $\langle \rho_0 \rangle$ constantly drifts towards larger values reach-

ing $\rho_0^{\mathrm{exp}} \approx 0.7$ for the largest examined evolution time $t_{\mathrm{evo}} = 12\,\mathrm{s}$. This value is significantly larger than the stationary value predicted by the simulations (blue line) which is around $\rho_0^{\mathrm{st}} \approx 0.62$. The observed difference can be partially accounted by assuming the mean field phase space to be dynamically modified by atom loss. As previously discussed, spin-spin interactions scale as $\lambda_1 \propto N^{2/5}$ with atom number N [Ger13]. Using the life-time listed in Tab.6.1, we estimate $\lambda_1 \approx \lambda_1(0)(\exp(-12/35.6))^{2/5} \approx 2\pi \times 1.65\,\mathrm{Hz}$. We use this value to compute the associated change of the fixpoint position $\rho_0^{\mathrm{FP}} \approx 0.62 \rightarrow 0.65$ following Eq.(5.1). This value is closer to ρ_0^{exp}, but still differs significantly.

For setting B, the mean central mode population $\langle\rho_0\rangle$ exhibits an opposite late-time trend and drifts towards smaller values reaching $\rho_0^{\mathrm{exp}} \approx 0.62$ for $t_{\mathrm{evo}} = 12\,\mathrm{s}$. This value is in turn significantly smaller than stationary expectation $\rho_0^{\mathrm{st}} \approx 0.66$ estimated from the corresponding simulation (blue line). In direct contrast to setting A, the direction of the drift can not be accounted by atom loss since the associated reduction of the spin-spin interactions would shift the fixpoint towards larger values. This is an additional indication that in this case the late-time evolution can not be captured within the theoretical framework of the simulation.

It is important to emphasize, that we can not expect the TW simulations to capture all features of the spin dynamics at late times. These simulations rely on the validity of the single-mode approximation, namely that all atoms share the same spatial wave function and that the coupling between spin and motional degrees of freedom is suppressed. This assumption is particularly fragile for setting B, since in this case an important thermal fraction around $\sim 35\%$ develops after $10\,\mathrm{s}$ of evolution as shown in Fig.5.4. For spin-1 systems, the thermal atoms in the individual magnetic sub-levels have been observed to lose coherence and relax towards equipartition $\rho_0 = \rho_{\pm 1} = \frac{1}{3}$ in comparable timescales [Erh04]. This might partially account for the observed population drift towards smaller values in Fig.6.5(b), but requires further investigation.

In conclusion, we observe a qualitatively distinct late-time evolution for settings with minimal (A) and considerably larger heating (B), especially while examining the fluctuations. For setting A the trend and order of magnitude of the fluctuations agree with TW simulations, indicating that the long-term behavior arises from dephasing of the internal spin dynamics. By contrast, the fluctuations for setting B are significantly smaller suggesting that the late-time dynamics might be affected by an additional relaxation process. We investigate this disparate behavior in more detail in the next section by examining the impact of different initial conditions.

6.3. Exploring Different Initial Conditions

Here, we want to study the impact of different initial conditions on the late-time spin dynamics in order to identify the relevant processes leading to the observed behavior. In a dephasing dominated scenario, we expect the long-term fluctuations to increase with the amplitude of the initial ρ_0 oscillations as sketched in Fig.6.1. By contrast, we expect the fluctuations to be smaller and not correlated with the amplitude of the initial oscillations if the system is substantially impacted by decoherence (see Fig.6.2).

In order to assess these potential late-time scenarios, we examine the long-term ρ_0 distributions for different initial conditions.

6.3.1. Setting with Minimal Heating

We focus first on *setting A* and prepare initial conditions with $\rho_0(0) \approx \{0.9, 0.63, 0.5\}$. These are obtained after $\phi_{RF} = \{0.12, 0.2, 0.25\}\pi$ RF-rotations during the preparation sequence. We plot the initial ρ_0 oscillations within $t_{evo} \leq 1\,\mathrm{s}$ in Fig.6.6(a) and fit a damped sine of the form $\rho_0(t) = A\sin(2\pi f t)\exp(-t/T) + b$ (red lines). We estimate thereby significantly different oscillation amplitudes A for these initial conditions. In the case of $\rho_0(0) = 0.63$ the oscillations are suppressed since the system is initialized close to the fixpoint $\rho_0^{FP} \approx 0.62$ of the mean field dynamics.

In order to investigate the late-time behavior, we additionally record large samples of ~ 150 runs per setting after $t_{evo} = 12\,\mathrm{s}$ of evolution and generate normalized ρ_0-histograms for the different initial conditions in Fig.6.6(b). We observe a clear correlation, namely that the late-time variances $\sigma^2 \approx \{1.3 \times 10^{-2}, 5.3 \times 10^{-4}, 7.3 \times 10^{-3}\}$ increase with the initial oscillation amplitudes $A \approx \{0.28, 0.02, 0.16\}$. Moreover, the ρ_0-distribution is qualitatively different if the system is prepared close to the fixpoint: In this case the histogram exhibits only a narrow single peak, in contrast to the double-peaked shapes for the remaining initial conditions.

Comparison To Simulations

We compare these findings to the histograms obtained from Truncated Wigner simulations after $12\,\mathrm{s}$ of evolution which are displayed in Fig.6.6(c). As before, we incorporate $\Delta q = 2\pi \times 0.11\,\mathrm{Hz}$ fluctuations in order to ensure saturated variances after $12\,\mathrm{s}$. The overall behavior is compatible to the experimental observations: We observe higher fluctuations for the settings with larger initial oscillations. Moreover, we can also qualitatively reproduce the single and double-peaked histograms for initial conditions prepared close and further away from the fixpoint. The single-peaked histograms in (b_2, c_2) are probably due to additional Gaussian noise of the fixpoint position because of q fluctuations, which 'blur' narrow double-peak features. This is plausible, since the error propagated variance of the fixpoint position $\sigma_{FP}^2 \approx (0.25\Delta q/|\lambda_1|)^2 \approx 2 \times 10^{-4}$ is in the same order of magnitude as the observed late-time variances in Fig.6.6(b_2, c_2). Asymmetric features in the theoretical histograms are also attributed to q fluctuations as these effectively modify the phase space and result in a spread along different mean field trajectories.

We observe qualitative agreement between the experimental observations for the setting with minimal heating and the simulations for different initial conditions. This is a clear indication that in this case the long-time spin state is significantly affected by *dephasing* of the internal dynamics. However, the widths of the experimental histograms are systematically smaller and the mean values are consistently larger than the theoretical results indicating that the simulations do not capture the full extent of the dynamics. Additional dissipative processes such as atom-loss and minimal heating can induce decoherence and potentially reduce the late-time fluctuations.
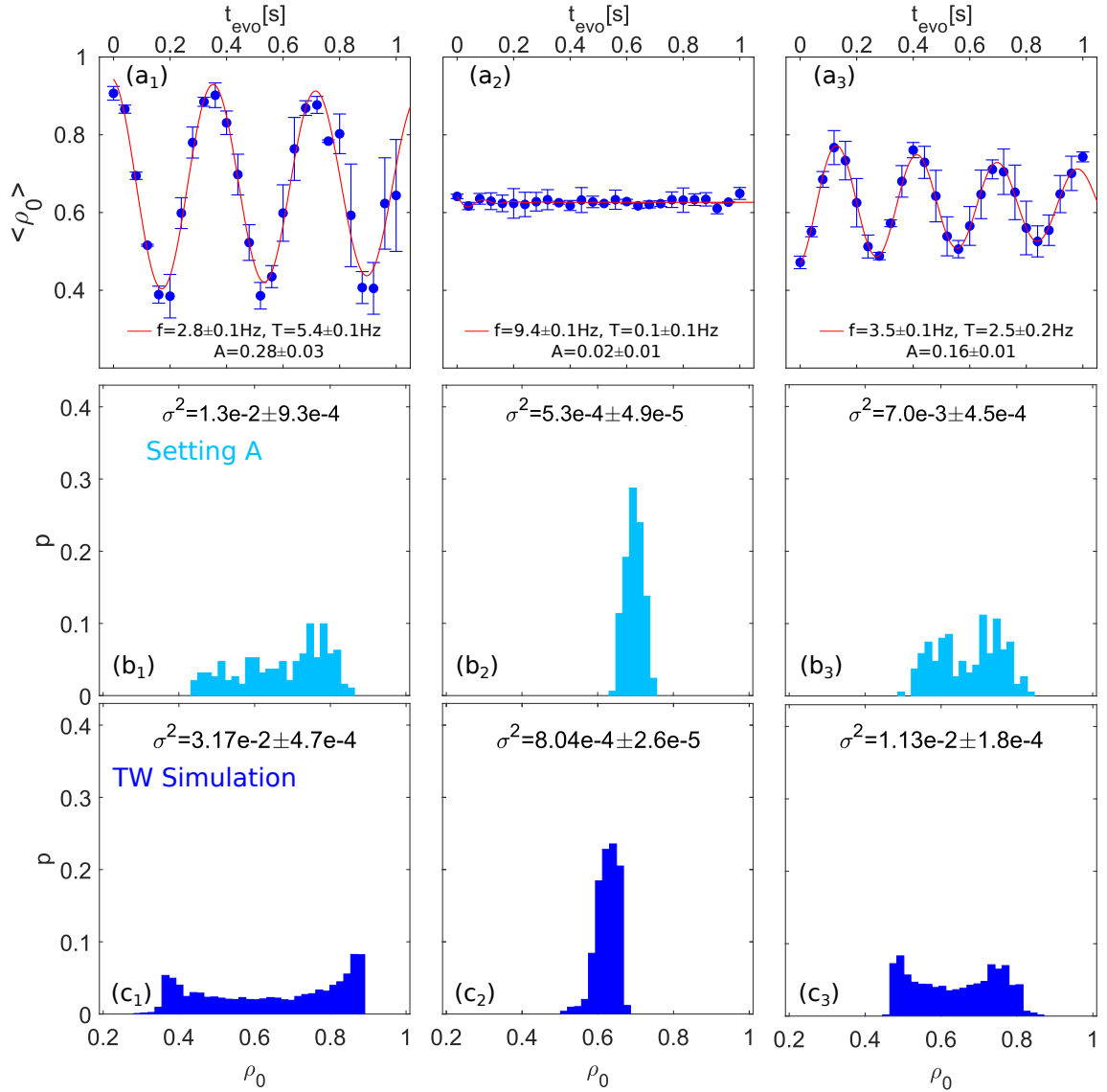
Figure 6.6.: **Initial ρ_0-oscillations, long-time distributions for setting A and TW simulations for different initial conditions.** We plot the experimental ρ_0-oscillations **(a)** for initial conditions with $\langle \rho_0(0) \rangle = \{0.91, 0.63, 0.5\}$ (blue points). We average over ~ 3 realizations and the error bars are the SEM. The amplitude A, frequency f and damping time T of the oscillations are estimated using damped sinusoidal fits (red curves). We plot normalized ρ_0-histograms after $12\,\mathrm{s}$ **(b)** for the corresponding initial conditions (~ 150 realizations). The late-time variance σ^2 increases with the initial oscillation amplitude. Moreover, we observe a narrow single-peaked histogram close to the fixpoint (b_2) and broader double-peaked distributions for the remaining cases. Additionally, we plot the corresponding histograms obtained from TW simulations **(c)** using 2500 samples and $\frac{\Delta q}{2\pi} = 0.11\,\mathrm{Hz}$. As for the experimental results, σ^2 increases with the initial oscillation amplitude. While the fluctuations are larger, these histograms capture the overall shape and initial condition dependence of the experimental results.

6.3.2. Impact of Heating

We turn now to *setting B* which exhibits a larger heating rate and examine also the short-time ρ_0 oscillations for comparable initial conditions with $\langle\rho_0(0)\rangle \approx \{0.9, 0.63, 0.5\}$ in Fig.6.7(a). As before, we estimate the frequency f, $1/e$ damping time T and amplitude $A \approx \{0.20, 0.03, 0.25\}$ of the initial oscillations using damped sinusoidal fits (red lines). The different amplitudes and higher frequencies in comparison to setting A are attributed to the larger values for the q and λ_1 listed in Tab.6.1. Additional measurements at comparable mean field parameters are required to assess, whether the tendentially faster damping of the oscillations in comparison to setting A can be attributed to the influence of decoherence.

We examine also the late-time behavior after $12\,\text{s}$ of evolution and plot the corresponding ρ_0 histograms in Fig.6.7(b), which are also extracted from ~ 150 experimental realizations. In direct contrast to the corresponding TW simulations in Fig.6.7(c), the experimental variances σ^2 are appreciably smaller and not apparently correlated with the amplitudes of the initial oscillations. Additionally, the experimental histograms consistently exhibit only a single narrow peak centered around $\rho_0^{\text{st}} \approx 0.61$ for all examined initial conditions $\rho_0(0)$ in contrast to the broader double-peaked histograms for setting A. This points to a late-time evolution which to some extent 'loses memory' of the initial configuration and is independent of the particular choice $\rho_0(0)$.

Combining these observations with the decay of the transverse spin at comparable evolution times (see section 5.4), we find indications that the long-time spin dynamics is significantly affected by heating of the motional degrees of freedom. In direct to settings with minimal heating, dephasing does not seem to be the primary factor determining long-term spin dynamics. On the contrary, the late-time behavior seems to be dominated by a dissipative *relaxation* towards a *quasi-steady state* characterized by the progressive loss of phase coherence as $F_\perp \to 0$ and by populations relaxing towards a single value $\rho_0^{\text{st}}(t)$ independently of the choice of initial conditions $\rho_0(t) \to \rho_0^{\text{st}}(t)$. The latter is evidenced by the small fluctuations around this value for the examined initial conditions.

The long-time state $\rho_0^{\text{st}}(t)$ is labeled as 'quasi-steady', since in Fig.6.5(b) we observe a slow drift of the mean central mode population on the order of $\frac{d}{dt}\langle\rho_0\rangle \approx -0.006\,\frac{1}{\text{s}}$. Additional measurements at even larger timescales are required to assess whether the average central mode population eventually converges towards a stationary value. This might prove difficult, as we lose a significant fraction of atoms at these large evolution times. Moreover, it is also important to further experimentally assess whether the particular choice of mean field parameters q and λ_1 affects the observed relaxation.
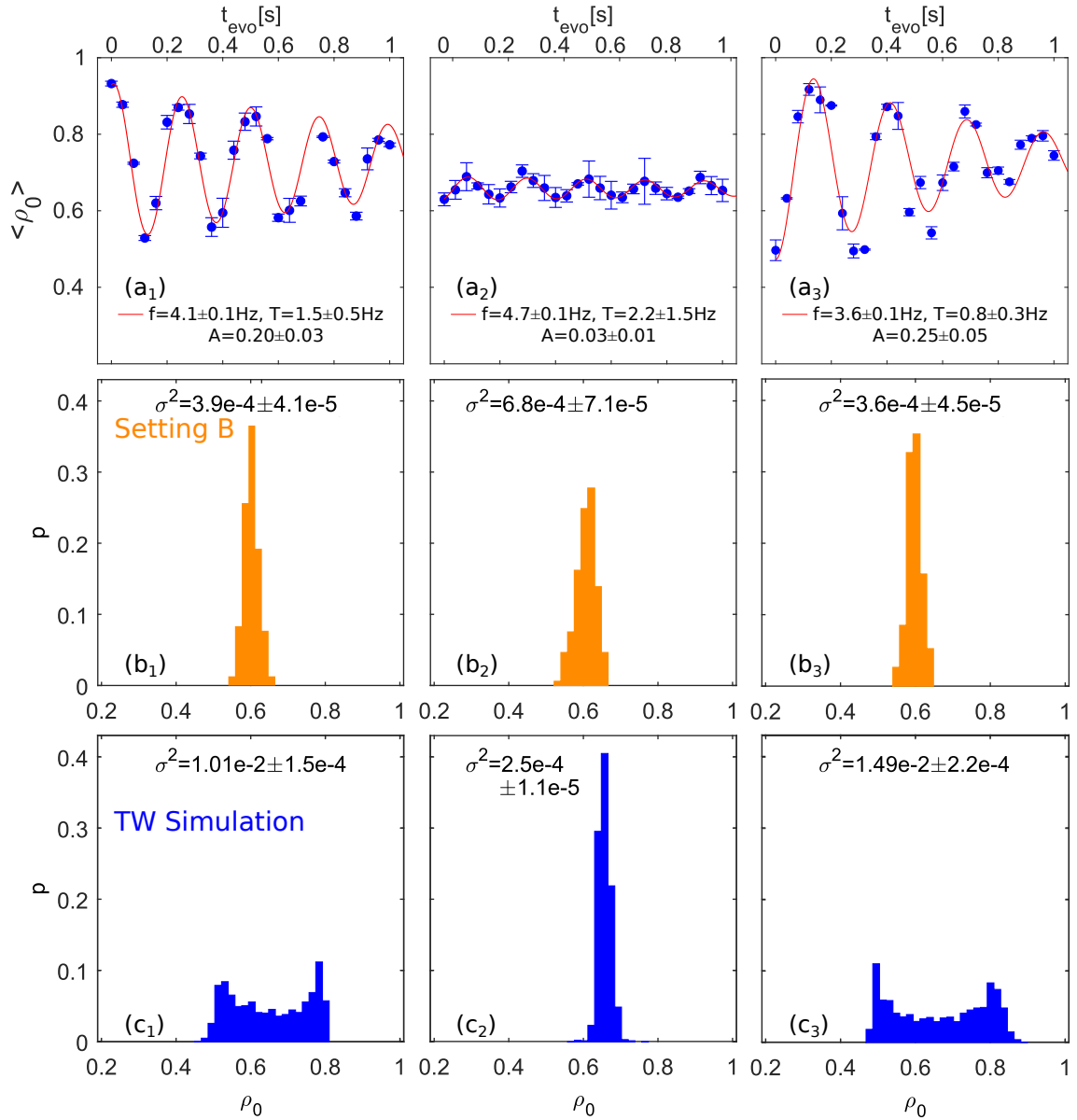
Figure 6.7.: **Initial ρ_0 oscillations, long-time fluctuations for setting B and TW simulations for different initial conditions.** We plot the short-time ρ_0-oscillations **(a)** for initial conditions with $\langle\rho_0(0)\rangle = \{0.9, 0.63, 0.5\}$ (blue points). We average over ~ 3 realizations and the error bars are the SEM. We employ damped sinusoidal fits (red lines) and extract the frequency f, damping time T and amplitude of the oscillations A. The corresponding normalized ρ_0-histograms after $12\,\text{s}$ are constructed from ~ 150 realizations and plotted in **(b)**. We also plot the histograms obtained from TW simulations **(c)** with $\frac{\Delta q}{2\pi} = 0.11\,\text{Hz}$. In direct contrast to the simulations and to setting A, there is no apparent correlation between the experimental variances σ^2 after $12\,\text{s}$ and the initial oscillation amplitudes A. Moreover, we observe narrow single-peaked histograms centered around $\rho_0 \approx 0.61$ for all examined initial conditions. This indicates that the late-time dynamics is not primarily determined by dephasing, but rather by a dissipative relaxation.

Conclusions

In this final chapter, we examine the evolution of the central mode population ρ_0 in order to further characterize the nature of long-time spin states. Even for settings with minimal heating, $\langle \rho_0 \rangle$ oscillations damp within $\sim 5\,\mathrm{s}$. This accelerated dephasing is attributed to additional fluctuations of experimental parameters such as q. Moreover, we observe distinct trends for the fluctuations for configurations exhibiting minimal (*setting A*) and substantially larger heating (*setting B*).

- For setting A the fluctuations of ρ_0 significantly increase and peak within the first $4\,\mathrm{s}$ of evolution. The timescale and order of magnitude of the fluctuations are compatible with Truncated Wigner (TW) simulations. The incorporated q fluctuations induce significantly faster dephasing of the spin dynamics within $\sim 5\,\mathrm{s}$ in comparison to $\sim 15\,\mathrm{s}$ expected solely from quantum fluctuations.

- Meanwhile, the fluctuations for setting B are initially compatible but increase significantly slower within the $12\,\mathrm{s}$ examined time window. They remain approximately an order of magnitude smaller than for setting A and for the corresponding TW simulation even after $12\,\mathrm{s}$ of evolution.

We take a closer look at this disparate behavior and study the dynamics for different initial conditions $\rho_0(0)$. In a dephasing dominated scenario, we expect that initial conditions with larger oscillation amplitudes also exhibit higher late-time fluctuations. This is captured within our TW simulations, which predict broad double-peaked histograms. We assess this by examining different initial conditions:

- For setting A we observe indeed increasingly broader double-peaked ρ_0 histograms after $12\,\mathrm{s}$ for initial conditions displaying oscillations with larger amplitudes. While smaller in magnitude, the trend of the fluctuations and overall shape of the distributions is compatible with the simulation results.

- On the contrary, for setting B we observe no apparent correlation between the amplitude of the initial oscillations and the width of the late-time distributions. Moreover, we consistently obtain single-peaked ρ_0 histograms centered around the same average value for all examined initial conditions.

If we collect the findings of the last two chapters, we can conclude that heating of the cloud density seems to appreciably affect the evolution and overall behavior of long-time spin states: For the setting with minimal heating, a significant transverse spin $F_\perp$ survives at late times signalizing that the system retains long-term coherence. Moreover, the large late-time ρ_0 fluctuations and qualitative agreement with the simulations for different initial conditions indicates that the corresponding spin states primarily arise from *dephasing* of the internal spin dynamics. The accelerated dephasing is attributed to experimental q fluctuations. By contrast, for the setting exhibiting larger heating we observe narrow late-time ρ_0 distributions centered around the same value $\rho_0^{\mathrm{st}}(t)$ for different initial conditions and a constant decay of $F_\perp$. This points to a long-time evolution governed by *decoherence* and a qualitatively distinct dissipative *relaxation* of population dynamics towards $(F_\perp(t), \rho_0(t)) \to (0, \rho_0^{\mathrm{st}}(t))$.

7. Conclusion and Outlook

During the course of this master thesis, we develop new probing techniques and use them to examine the internal spin dynamics within the $F=1$ ground state hyperfine manifold of our ^{87}Rb Bose-Einstein condensate. Specifically, we focus on studying and understanding the long-time evolution of this spin-1 system.

We present and characterize a newly developed *readout scheme* which allows us to extract two orthogonal directions (F_x, F_y) of the transverse spin $F_\perp$ in a single experimental run employing our state selective absorption imaging setup. This technique relies on mapping one of the spin directions into population differences in magnetic sub-levels, using the $F=2$ manifold as a storage platform for the relevant populations and measuring the remaining direction in $F=1$ accordingly. As a first application, we employ this scheme to probe the *short-time spin dynamics* in our system. We concentrate on evolution times $t_{\mathrm{evo}} \leq 1\,\mathrm{s}$ which are comparable with the internal timescale associated with spin-mixing $|\lambda_1| \sim 2\pi \times 2\,\mathrm{Hz}$. We observe coherent oscillations of the mean transverse magnetization driven by spin-changing collisions, which are captured by the mean field predictions for different initial conditions.

Afterwards, we concentrate on studying the *long-time dynamics* for evolution times up to $\lesssim 15\,\mathrm{s}$. For the typical trapping configurations with $(\omega_\perp, \omega_{||}) \approx 2\pi \times (220, 46)\,\mathrm{Hz}$, we observe a decaying transverse spin indicating long-term decoherence. Moreover, we observe that the life-time of the transverse spin is maximized in a q-regime exhibiting spin-mixing. This is plausible, since spin-changing collisions build up coherences and might partially counteract the processes driving the decoherence. Additionally, we examine the *impact of heating* of the motional degrees of freedom on the spin dynamics, which we experimentally control by adjusting the power of the waveguide trap. Indeed, we find settings with minimal and substantially larger heating rates for shallower and tighter confinement. We attribute this mainly to residual evaporation in the former and to larger scattering rates of trap photons in the latter case. Moreover, we observe a clear connection between heating and the long-term spin dynamics: For settings with larger heating, the average transverse magnetization clearly decays and the fluctuations are suppressed. On the contrary, for settings with minimal heating a significant spin survives even after 15 s of evolution accompanied by a large spread of individual realizations. This indicates that the system retains long-term coherence.

Finally, we probe the long-time dynamics of the central mode population ρ_0 in order to further assess the impact of finite temperature effects. For settings with minimal heating, the late-time fluctuations are nearly an order of magnitude larger. Moreover, we prepare different initial conditions and examine the ρ_0-distributions after 12 s of evolution. For the setting with *minimal heating* we observe distinctive broad double-peaked histograms if the system is initialized away from the fixpoint. We can capture their overall shape and the initial condition dependence with Truncated

Wigner simulations incorporating additional q fluctuations. This is a clear indication that the long-time spin state primarily arises from the predicted *dephasing* of the internal dynamics. By contrast, the setting with *larger heating* exhibits narrower single-peaked distributions centered around the same value for all examined initial conditions. Together with the observed $F_\perp$ decay, this indicates a disparate late-time state governed by *decoherence* and a *dissipative relaxation* of population dynamics.

Outlook

On the theory side, one relevant open question is to determine the actual *microscopic mechanism* driving the observed late-time decoherence for settings with larger heating. In this scenario, the single-mode approximation is manifestly violated since a significant thermal component develops within $\sim 10\,\text{s}$ which in turn can interact with the condensate. There have been theoretical efforts in this direction for spin-1 systems [End11] which model the evolution of coupled thermal and condensate fields relying on kinetic gas theory. The associated collisional terms enable spin-mixing involving both thermal and condensate atoms. Moreover, for thermal spin-1 gases the populations within individual magnetic sub-levels are expected to dissipatively relax towards equipartition near $q \approx 0$[End09, Erh04]. It seems feasible, that as the cloud heats and the thermal fraction increases it might constitute an effective bath which rapidly losses coherences and drives an analogous process within the condensate via spin-changing collisions. Such a mechanism would resemble the *spin locking* between thermal and condensate atoms observed for spin-$\frac{1}{2}$ systems [McG03].

Additionally, it is important to develop diagnostic tools and measurement schemes to further characterize late-time spin states in our system. In the context of the Eigenstate Thermalization Hypothesis [Kho15], it is relevant to assess if our spin-1 system can experience thermal relaxation under its own dynamics and to examine whether the late-time behavior for settings with appreciable heating is compatible with a *thermal spin state*. We have taken first steps in this direction by performing small controlled spinor phase rotations after long periods of evolution and monitoring the subsequent dynamics. This linear response measurement can be complemented by an analysis of fluctuations and used in principle to probe the (non-)thermal nature of the system relying on the fluctuation-dissipation theorem.

On a more experimental level, it is essential to diversify our preparation and probing techniques. In this context, a direct extension F_x-F_y readout scheme presented in this thesis allows to *simultaneously measure all spin directions* F_x, F_y, F_z in a single experimental run [Kun18a]. This extended scheme relies on using the larger $F = 2$ manifold also as a storage platform for the atomic populations required to access F_z. It constitutes a powerful tool to experimentally investigate non-equilibrium spin dynamics following parametric quenches, especially for elongated quasi-1D BECs confined in the waveguide trap. In particular, we can employ this scheme to study scaling dynamics of different spin-1 observables for quenches of an initial polar state into phases exhibiting spin-mixing following the observations in [Prü18]. Building on the results presented here, a first step could be to operate with trapping configurations exhibiting minimal heating and to investigate whether the observed long-term survival of coherences facilitates scaling dynamics at even larger timescales.

A. Supplementary Analysis

A.1. Exemplary RF-Rabis in $F{=}1$ and $F{=}2$

As discussed in the main text, we prepare balanced superpositions of the form $|1, -1\rangle + |2, -2\rangle$ and address them with the linearly polarized radio frequency fields originating from two nearly orthogonal coils. We tune the relative phase between these fields ϕ_c and examine the Rabi oscillations of the magnetization along the quantization axis $\langle \hat{F}_z \rangle$ for atoms in $F{=}1$ and $F{=}2$. Here, we present the results for representative relative phases $\phi_c = 0.69\pi$ (Fig.A.1) and $\phi_c = -0.44\pi$ (Fig.A.2) which suppress the Rabi oscillations in $F{=}2$ and $F{=}1$ respectively.
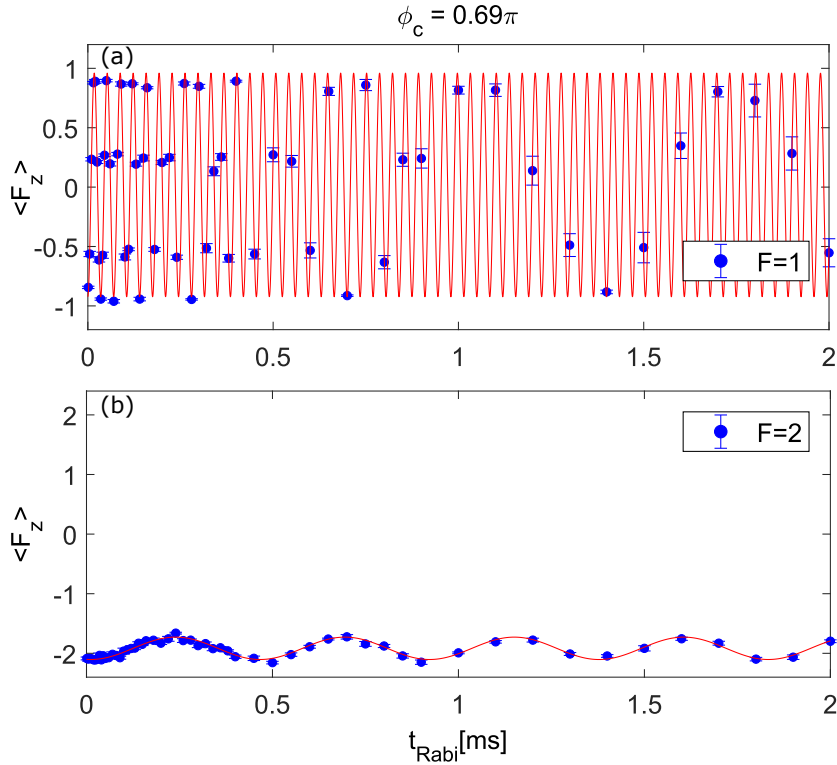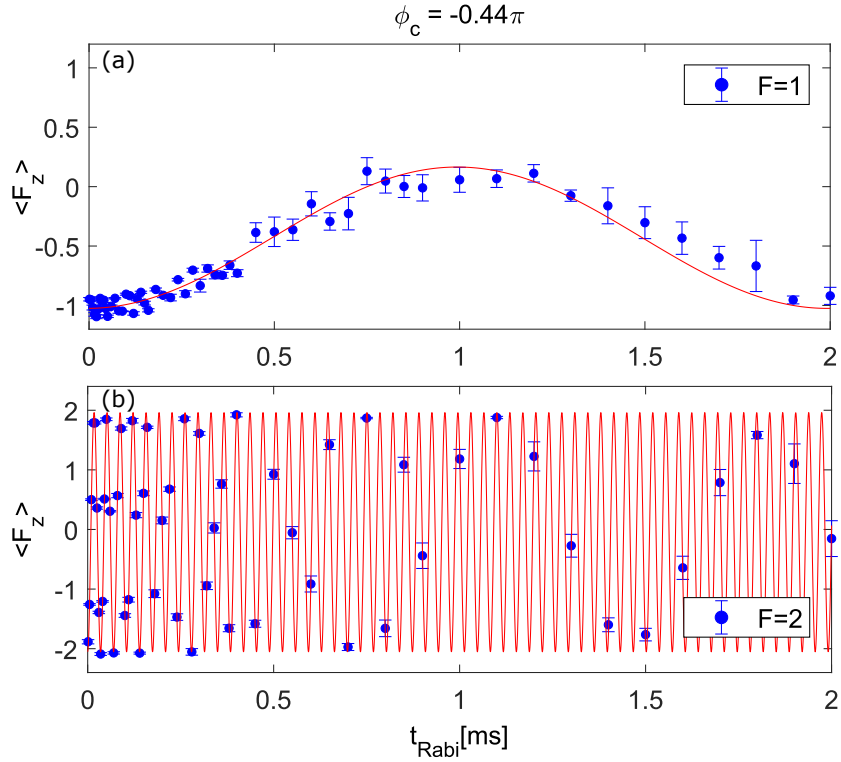

Figure A.1.: **Radio frequency Rabis in $F{=}1$ (a) and $F{=}2$ (b) for $\phi_c = 0.69\pi$.** We measure the Rabi oscillations of $\langle \hat{F}_z \rangle$ (blue points) after averaging over ~ 10 realizations. For this particular choice of ϕ_c, the oscillations in $F = 2$ are significantly suppressed which is reflected in the smaller values for the amplitude and the Rabi frequency Ω_{RF}. Fitting sinusoidal functions (red lines), we obtain $\frac{\Omega_{\mathrm{RF,fit}}}{2\pi} \approx \{29, 2.2\}$kHz for $F = \{1, 2\}$.

Figure A.2.: **Radio frequency Rabis in $F{=}1$ (a) and $F{=}2$ (b) for $\phi_{\mathrm{c}} = -0.44\pi$.** We measure the Rabi oscillations of $\langle \hat{F}_z \rangle$ (blue points) after averaging over ~ 10 realizations. For this particular value of the relative phase, the oscillations in $F = 1$ are appreciably suppressed which is reflected in the smaller values for the Rabi frequency Ω_{RF}. Fitting a sinusoidal function (red lines), we obtain $\frac{\Omega_{\mathrm{RF,fit}}}{2\pi} \approx \{0.5, 29\}$kHz for $F = \{1, 2\}$.

A.2. Spin-Mixing Spectroscopy

Here, we present the results of an exemplary *spin-mixing spectroscopy* for $N(0) \approx$ 19000 atoms and $(\omega_\perp, \omega_{||}) = 2\pi \times (220, 46)$Hz in order to determine the q-regime exhibiting spin-changing collisions. We prepare an initial polar state, tune q by adjusting the MW dressing and monitor the side mode population after $t_{\text{evo}} = 4\,$s of evolution. In Fig.A.3 we plot the normalized side mode population $\rho_1 + \rho_{-1}$ for different detuning values q. We observe non-negligible side mode populations for $-4\,\text{Hz} \lesssim \frac{q}{2\pi} \lesssim 6\,\text{Hz}$ signalizing spin-mixing.

Additionally, we plot absorption images of the individual magnetic sub-levels for representative q values in the insets. They are recorded after $t_{\text{exp}} = 10\,$ms of expansion in the waveguide trap and a subsequent Stern-Gerlach separation. Spin-mixing is also directly visible in the individual realizations as finite atomic population in $|1, \pm 1\rangle$. For the q regime examined here we observe homogeneous single-peaked density profiles up to noise speckles. Hence, spin-mixing for this particular choice of parameters does not seem to excite higher trapping modes supporting the validity of the single-mode approximation.
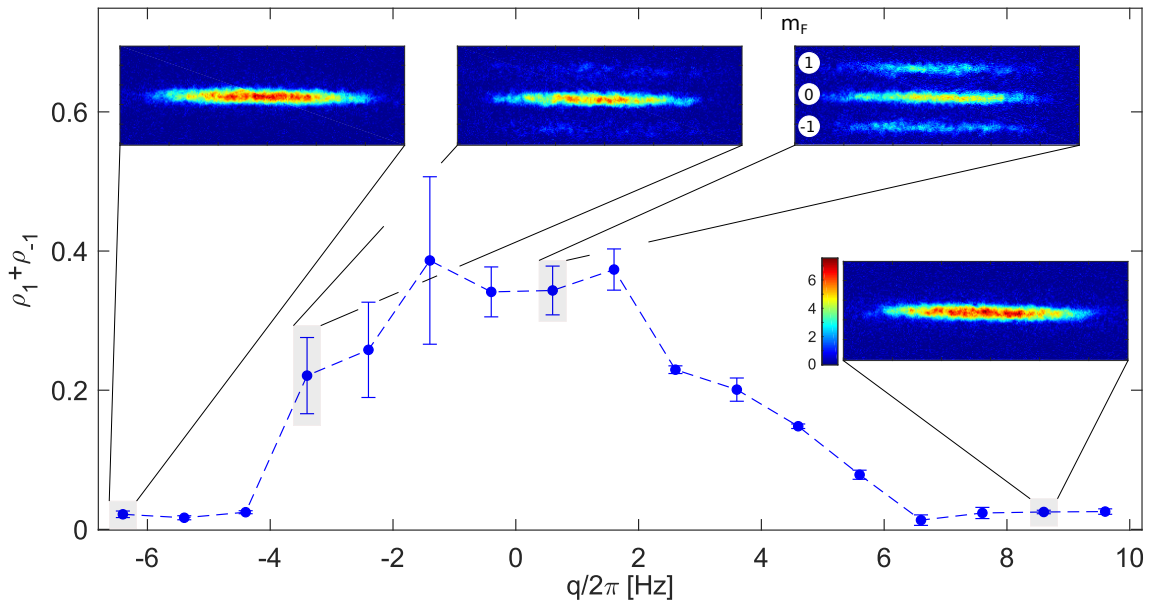

Figure A.3.: **Spin-mixing spectroscopy ($N(0) \approx 19000$ atoms).** We average over ~ 3 realizations and plot the normalized mean side mode population $\rho_1 + \rho_{-1}$ vs. q after $4\,$s of evolution from an initial polar state. We observe non-negligible side mode populations for $-4\,\text{Hz} \lesssim \frac{q}{2\pi} \lesssim 6\,\text{Hz}$ signalizing spin changing collisions. Moreover, the larger errors in the rising flank of the spectroscopy around $-2\,$Hz are attributed to larger fluctuations of the spin-changing collisions rate. We plot absorption images for representative q values in the insets. The color scale corresponds to the number of atoms per pixel of $(0.42\,\mu\text{m})^2$. We observe single-peaked profiles in the individual magnetic sub-levels for the examined q regime, supporting the single-mode approximation.

A.3. Atom Loss for Different Trapping Configurations

In this section, we examine the atom loss rate for the different trapping configurations employed during the heating analysis in section 5.3.2. We prepare states with $N \approx 12000$ atoms and monitor the atom loss for settings with transverse trapping frequencies $f_\perp = \{260, 220, 170, 150\}$Hz. We plot the results in Fig.A.4. The $1/e$ life-time of the condensate is estimated using exponential fits of the form $N = N_0 \exp(-t/T_{\mathrm{LT}})$ (red lines). The fit goodness is not optimal as only four data points are used to estimate two fit parameter.

We observe a clear trend: The life-time of the condensate is largest for the tightest trapping setting ($T_{\mathrm{LT}} \approx 50\,\mathrm{s}$). This is plausible, since we expect residual evaporation during evolution for the two shallower trapping configurations (see main text). Moreover, a significant thermal fraction develops within $15\,\mathrm{s}$ for the two tighter trapping settings effectively reducing the average density n of the atomic cloud and thereby also the rate of three-body collisions ($\propto n^2$).
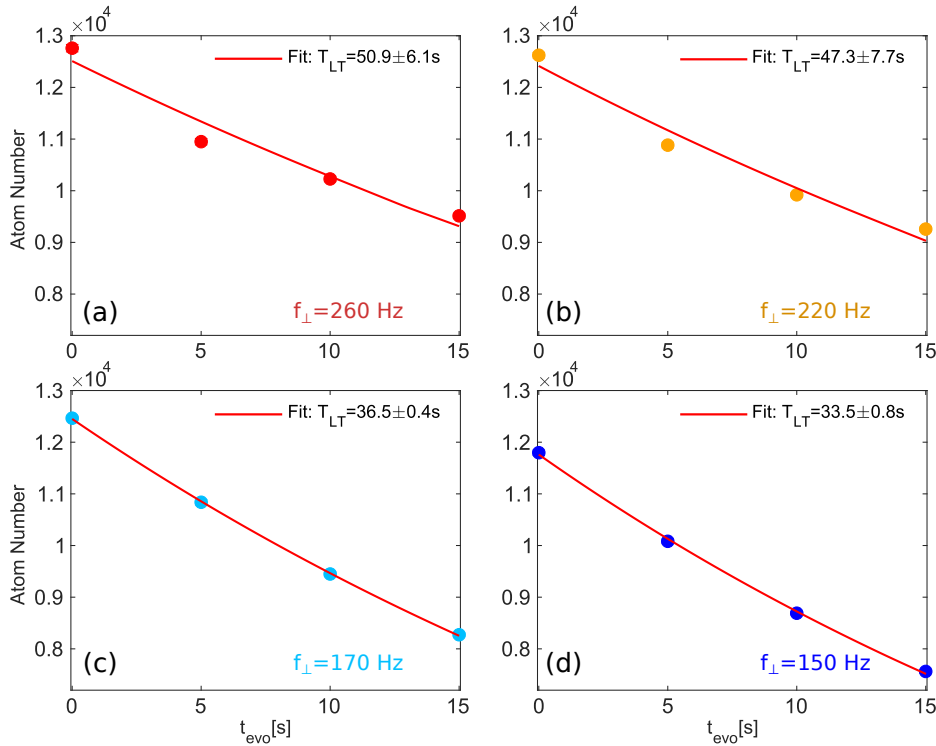

Figure A.4.: **Atom loss for different trapping configurations with $f_\perp = \{260, 220, 270, 150\}$Hz in (a)-(d).** We examine the atom loss for states with $N \approx 12000$ atoms and estimate the $1/e$ life-time of the condensate using exponential fits (red lines). For comparable atom numbers, the life-time is significantly larger for the tighter trapping configurations (a,b) which also exhibit substantially larger heating rates. This observation supports our working hypothesis that the BEC experiences residual evaporation in the shallower trapping settings (c,d).

A.4. Statistical Uncertainty of Heating Analysis

Here, we take a closer look at the statistical uncertainty of condensate fraction estimation using the bimodal fits in Eq.(5.4). We record $S=396$ realizations with $N=12000$ atoms and moderate thermal fractions ($\frac{N_{\mathrm{C}}}{N} \approx 0.73$). We average together within subsets of size s and construct mean density profiles before fitting $\frac{N_{\mathrm{C}}}{N}$. Afterwards, we compute the standard deviation $\sigma_{\mathrm{CF}}(s)$ of $\frac{N_{\mathrm{C}}}{N}$ within the different subsets and plot them in Fig.A.5 in a double logarithmic scale (blue data points). The error of σ_{CF} is obtained using a resampling method [Mil74]. The standard deviation decreases as $\sigma_{\mathrm{CF}} \propto \frac{1}{\sqrt{s}}$ (red guideline to the eye). This is plausible, since averaging over increasingly more realizations suppresses noise features of the density profiles enabling a preciser condensate fraction estimation, as we can see in the profiles in the insets for $s=2$ and $s=64$. We can reduce the statistical uncertainty below $\sigma_{\mathrm{CF}} \approx 0.01$ if we average over $\gtrsim 30$ realizations before applying the bimodal fits.

We can draw a parallel between our analysis and the Allan deviation $\sigma_{\mathrm{A}}(\tau)$. For the latter, white-noise in the frequency regime scales as $\sigma_{\mathrm{A}}(\tau) \propto \frac{1}{\sqrt{\tau}}$ with the integration time of the signal τ [Bar70] suggesting that the statistical uncertainty in our method is similar in nature.
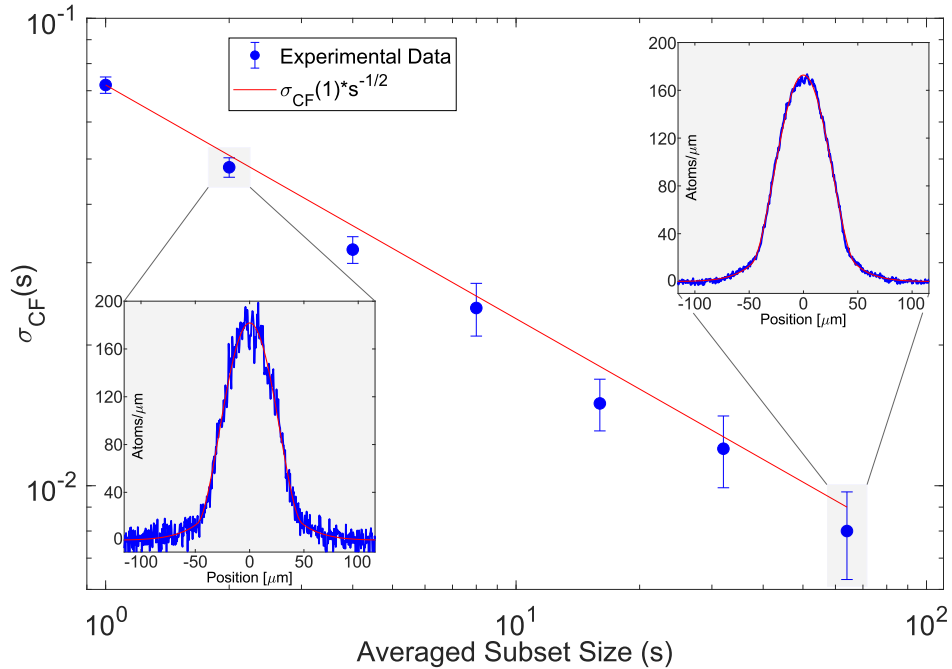

Figure A.5.: **Statistical uncertainty of condensate fraction analysis**. We record $S = 396$ realizations. We average the profiles within subsets of size $s < S$, fit the condensate fraction using bimodal fits and plot the standard deviation between the subsets $\sigma_{\mathrm{CF}}(s)$ (blue points). We observe a clear $1/\sqrt{s}$ decay (red guideline) suggesting that the condensate fraction estimation is limited by uncorrelated white-noise affecting the fitted profiles. This is visible in insets, where we plot representative mean profiles (blue curves) averaged over $s=2$ and 64 realizations and the corresponding fits (red lines).

A.5. Comparison of Experimental and Mean Field Population Oscillations

In this section, we compare the experimentally observed short-time oscillations of the central mode population $\rho_0^{\mathrm{exp}}(t)$ with mean field predictions $\rho_0^{\mathrm{MF}}(t)$ which we obtain after numerically solving the equations of motion in Eqs.(2.17). We optimize the agreement between theory and experiment in order to estimate the detuning q and the spin-spin interactions λ_1: To this end, we initialize $\rho_0^{\mathrm{MF}}(0) = \rho_0^{\mathrm{exp}}(0)$ and estimate the mean field parameters by minimizing the absolute deviation between the theoretical and experimental values $D(q, \lambda_1) = \langle |\rho_0^{\mathrm{exp}}(t) - \rho_0^{\mathrm{MF}}(t)|_{(q,\lambda_1)}| \rangle$. Here, $\langle \rangle$ denotes an average over all experimentally measured times t.

We plot exemplary results in Fig.A.6 for a state with $\langle \rho_0(0) \rangle = 0.48$ and $N = 12000$. We plot the mean deviation $D(q, \lambda_1)$ in (a) and observe a minimum at $(q, \lambda_1) = 2\pi \times (0.92, -1.91)\mathrm{Hz}$. We also scan a significantly wider range of parameters in order to ensure that this is indeed a global minimum. The corresponding mean field oscillations of ρ_0 (solid black lines) for these optimal parameters (b) are compatible with the experimental observations (blue points).
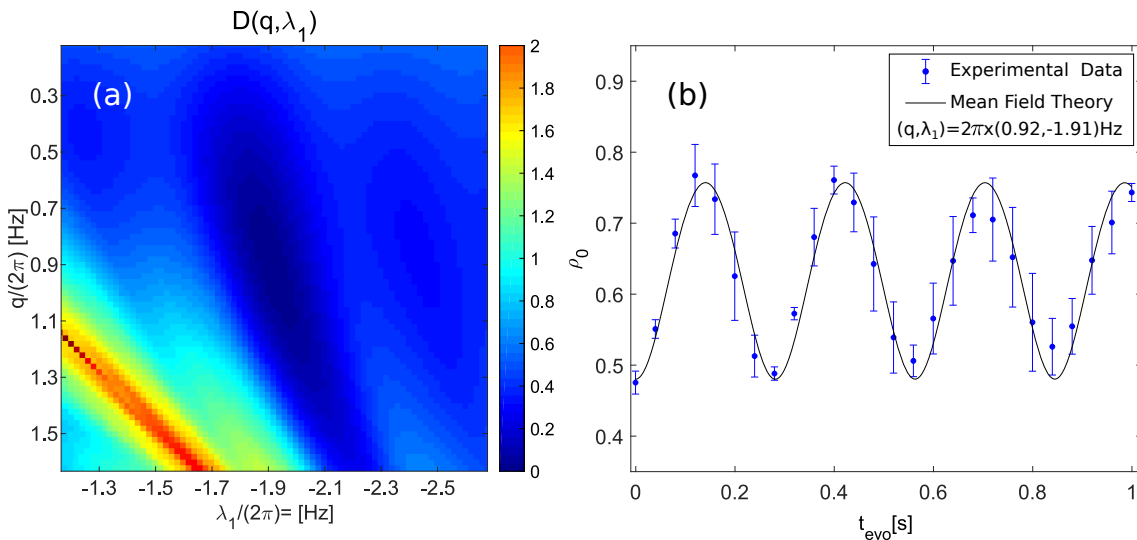

Figure A.6.: **Comparison between experimental and mean field ρ_0.** We solve the mean field equations of motion numerically for different combinations of q and λ_1 and plot the average absolute deviation between the theoretical and experimental populations $D(q, \lambda_1)$ in **(a)**. The agreement is assumed to be optimal if $D(q, \lambda_1)$ is minimal. We also scan over a wider parameter range to ensure that the observed minimum is indeed a global one. Additionally, we plot the theoretical ρ_0 oscillations for the optimal mean field parameters (black line) together with the experimental results (blue points) in **(b)** and observe reasonable agreement.

Bibliography

[And95]   M. H. Anderson, J. R. Ensher, M. R. Matthews, C. E. Wieman, E. A. Cornell, *Observation of Bose-Einstein condensation in a dilute atomic vapor*, science **269**(5221), 198–201 (1995).

[Bar70]   J. Barnes, A. Chi, L. Cutler, D. Healey, D. Leeson, T. McGunigal, J. Mullen, W. Smith, R. Sydnor, R. Vessot, *et al.*, *Characterization of frequency stability, NBS Tech*, Technischer Bericht, Note 394, 48 pp (1970).

[Ber14]   J. Berges, K. Boguslavski, S. Schlichting, R. Venugopalan, *Turbulent thermalization process in heavy-ion collisions at ultrarelativistic energies*, Physical Review D **89**(7), 074011 (2014).

[Bla07]   A. T. Black, E. Gomez, L. Turner, S. Jung, P. D. Lett, *Spinor dynamics in an antiferromagnetic spin-1 condensate*, Physical review letters **99**(7), 070403 (2007).

[Bla08]   P. Blakie, A. Bradley, M. Davis, R. Ballagh, C. Gardiner, *Dynamics and statistical mechanics of ultra-cold Bose gases using c-field techniques*, Advances in Physics **57**(5), 363–455 (2008).

[Blo12]   I. Bloch, J. Dalibard, S. Nascimbene, *Quantum simulations with ultracold quantum gases*, Nature Physics **8**(4), 267 (2012).

[Cas96]   Y. Castin, R. Dum, *Bose-Einstein condensates in time dependent traps*, Physical Review Letters **77**(27), 5315 (1996).

[Cha05]   M.-S. Chang, Q. Qin, W. Zhang, L. You, M. S. Chapman, *Coherent spinor dynamics in a spin-1 Bose condensate*, Nature physics **1**(2), 111 (2005).

[D'A16]   L. D'Alessio, Y. Kafri, A. Polkovnikov, M. Rigol, *From quantum chaos and eigenstate thermalization to statistical mechanics and thermodynamics*, Advances in Physics **65**(3), 239–362 (2016).

[Dal99]   F. Dalfovo, S. Giorgini, L. P. Pitaevskii, S. Stringari, *Theory of Bose-Einstein condensation in trapped gases*, Reviews of Modern Physics **71**(3), 463 (1999).

[End09]   Y. Endo, T. Nikuni, *Population Dynamics of a Spin-1 Bose Gas above the Bose–Einstein Transition Temperature*, Journal of the Physical Society of Japan **78**(9), 094005–094005 (2009).

Bibliography

[End11] Y. Endo, T. Nikuni, *Kinetic theory of a spin-1 Bose condensed gas at finite temperatures*, Journal of Low Temperature Physics **163**(3-4), 92–121 (2011).

[Erh04] M. Erhard, H. Schmaljohann, J. Kronjäger, K. Bongs, K. Sengstock, *Bose-Einstein condensation at constant temperature*, Physical Review A **70**(3), 031602 (2004).

[Ger06] F. Gerbier, A. Widera, S. Fölling, O. Mandel, I. Bloch, *Resonant control of spin dynamics in ultracold quantum gases by microwave dressing*, Physical Review A **73**(4), 041602 (2006).

[Ger13] C. Gerving, *Dynamics of a quantum inverted pendulum explored in a Spin-1 BEC*, Dissertation, Georgia Institute of Technology (2013).

[Gio96] S. Giorgini, L. Pitaevskii, S. Stringari, *Condensate fraction and critical temperature of a trapped interacting Bose gas*, Physical Review A **54**(6), R4633 (1996).

[Gri00] R. Grimm, M. Weidemüller, Y. B. Ovchinnikov, *Optical dipole traps for neutral atoms*, in *Advances in atomic, molecular, and optical physics*, Vol. 42, 95–170 (Elsevier, 2000).

[Hal12] R. Hale, *Diagonalization techniques for sparse Matrices (Technical Report, University of Washington)* (May 2012).

[Ham12] C. D. Hamley, *Spin-nematic squeezing in a spin-1 Bose-Einstein condensate*, Dissertation, Georgia Institute of Technology (2012).

[Hoa13] T. M. Hoang, *Quantum control of a many-body system in a spin-1 Bose-Einstein condensate*, Dissertation, Georgia Institute of Technology (2013).

[Kaw12] Y. Kawaguchi, M. Ueda, *Spinor Bose–Einstein condensates*, Physics Reports **520**(5), 253–381 (2012).

[Ket99] W. Ketterle, D. S. Durfee, D. Stamper-Kurn, *Making, probing and understanding Bose-Einstein condensates*, arXiv preprint cond-mat/9904034 (1999).

[Kho15] A. Khodja, R. Steinigeweg, J. Gemmer, *Relevance of the eigenstate thermalization hypothesis for thermal relaxation*, Physical Review E **91**(1), 012120 (2015).

[Kit93] M. Kitagawa, M. Ueda, *Squeezed spin states*, Physical Review A **47**(6), 5138 (1993).

[Kle09] C. Klempt, G. Gebreyesus, M. Scherer, T. Henninger, P. Hyllus, W. Ertmer, L. Santos, J. Arlt, *et al.*, *Multiresonant spinor dynamics in a Bose-Einstein condensate*, Physical review letters **103**(19), 195302 (2009).

[Kun18a] P. Kunkel, M. Prüfer, S. Lannig, R. Rosa-Medina Pimentel, M. Gärt-
tner, A. Bonnin, H. Strobel, M. K. Obethaler, *Simultaneous read-out of
orthogonal spin directions*, In preparation (september 2018).

[Kun18b] P. Kunkel, M. Prüfer, H. Strobel, D. Linnemann, A. Frölian, T. Gasen-
zer, M. Gärttner, M. K. Oberthaler, *Spatially distributed multipartite
entanglement enables EPR steering of atomic clouds*, Science **360**(6387),
413–416 (2018).

[Lan16] T. Langen, T. Gasenzer, J. Schmiedmayer, *Prethermalization and univer-
sal dynamics in near-integrable quantum systems*, Journal of Statistical
Mechanics: Theory and Experiment **2016**(6), 064009 (2016).

[Lan18] S. Lannig, *Experimental control of a spin-1 Bose-Einstein Condensate*,
Masters Thesis, University of Heidelberg (2018).

[Les09] S. Leslie, J. Guzman, M. Vengalattore, J. D. Sau, M. L. Cohen, D. Stamper-
Kurn, *Amplification of fluctuations in a spinor Bose-Einstein condensate*,
Physical Review A **79**(4), 043631 (2009).

[Lin17] D. Linnemann, *Quantum-Enhanced Sensing Based on Time Reversal of
Nonlinear Dynamics*, Dissertation, University of Heidelberg (2017).

[Mar16] G. E. Marti, D. Stamper-Kurn, *Spinor Bose-Einstein gases*, Quantum
Matter at Ultralow Temperatures **191**, 221 (2016).

[McG03] J. McGuirk, D. Harber, H. Lewandowski, E. A. Cornell, *Normal-superfluid
interaction dynamics in a spinor Bose gas*, Physical review letters **91**(15),
150402 (2003).

[Mil74] R. G. Miller, *The jackknife-a review*, Biometrika **61**(1), 1–15 (1974).

[Mue13] W. Muessel, H. Strobel, M. Joos, E. Nicklas, I. Stroescu, J. Tomkovič, D. B.
Hume, M. K. Oberthaler, *Optimized absorption imaging of mesoscopic
atomic clouds*, Applied Physics B **113**(1), 69–73 (2013).

[Mü14] W. Müssel, *Scalable spin squeezing for quantum-enhanced magnetometry
with Bose-Einstein Condensates*, Dissertation, University of Heidelberg
(2014).

[Nol13] W. Nolting, *Grundkurs Theoretische Physik 5 Quantenmechanik: Teil 2:
Methoden und Anwendungen* (Springer-Verlag, 2013).

[Per13] H. Perrin, *Adiabatic potentials for RF-dressed atoms: spin And fields
(Lecture 1)*, Lecture Notes of Les Houches School of Physics (September
2013).

[Pit03] L. Pitaevskii, S. Stringari, *Bose-Einstein condensation* (Oxford University
Press, USA, 2003).

Bibliography

[Prü16]   M. Prüfer, *Structure formation in a quenched antiferromagnetic spinor Bose-Einstein condensate*, Masters Thesis, University of Heidelberg (2016).

[Prü18]   M. Prüfer, P. Kunkel, H. Strobel, S. Lannig, D. Linnemann, C.-M. Schmied, J. Berges, T. Gasenzer, M. K. Oberthaler, *Observation of universal quantum dynamics far from equilibrium*, arXiv preprint arXiv:1805.11881 (2018).

[Sak95]   J. J. Sakurai, E. D. Commins, *Modern quantum mechanics, Revised Edition* (AAPT, 1995).

[Sch10]   M. Scherer, B. Lücke, G. Gebreyesus, F. Deuretzbacher, W. Ertmer, L. Santos, J. Arlt, C. Klempt, *et al.*, *Spontaneous breaking of spatial and spin symmetry in spinor condensates*, Physical review letters **105**(13), 135302 (2010).

[Sin02]   A. Sinatra, C. Lobo, Y. Castin, *The truncated Wigner method for Bose-condensed gases: limits of validity and applications1*, Journal of Physics B: Atomic, Molecular and Optical Physics **35**(17), 3599 (2002).

[SK13]   D. M. Stamper-Kurn, M. Ueda, *Spinor Bose gases: symmetries, magnetism, and quantum dynamics*, Reviews of Modern Physics **85**(3), 1191 (2013).

[Ste01]   D. A. Steck, *Rubidium 87 D-Line Data* (2001).

[Str16]   H. Strobel, *Fisher Information and entanglement of non-Gaussian spin states*, Dissertation, University of Heidelberg (2016).

[Wid06]   A. Widera, F. Gerbier, S. Fölling, T. Gericke, O. Mandel, I. Bloch, *Precision measurement of spin-dependent interaction strengths for spin-1 and spin-2 87Rb atoms*, New Journal of Physics **8**(8), 152 (2006).

[Wil16]   L. A. Williamson, P. Blakie, *Universal coarsening dynamics of a quenched ferromagnetic spin-1 condensate*, Physical review letters **116**(2), 025301 (2016).

[Zaw08]   M. Zawada, R. Abdoul, J. Chwedeńczuk, R. Gartman, J. Szczepkowski, M. Witkowski, W. Gawlik, *et al.*, *Free-fall expansion of finite-temperature Bose-Einstein condensed gas in the non-Thomas–Fermi regime*, Journal of Physics B: Atomic, Molecular and Optical Physics **41**(24), 241001 (2008).

Acknowledgments

Here, I would like to thank everyone who made this thesis possible.

First and foremost, I want to thank Markus Oberthaler for giving me the opportunity to join the group and be part of very exciting projects. Your scientific input and guidance has been invaluable to me.

I also want to thank Selim Jochim for kindly accepting to be the second corrector of this thesis.

Many thanks to the BEC team for providing a very welcoming the enriching work environment. Particular thanks to:

- Alexis, for the close and open work rapport and meticulous supervision. I've learned a lot from the way you approach data analysis. Thank you for thoughtfully proofreading this thesis and providing very insightful remarks.

- Helmut, for always being open to share your vast 'technical know-how' on the experiment and spinor Bose-Einstein condensates. Our discussions have helped me develop a deeper understanding of this field.

- Martin, for the invaluable theory support, the insightful discussions and for patiently teaching me the fundamentals of Truncated Wigner simulations.

- Max, for explaining the underlying physics of the experiment to me every time I asked and for the various tips and tricks. Thank you for carefully proofreading this thesis and for your rapid and precise feedback in the last days.

- Philipp, for patiently teaching me how to operate the 'BEC machine'. Thank you also for the uncountable short and long explanations, the helpful feedback on how to make better presentations and for proofreading this thesis.

- Stefan, for the fruitful discussions about spin dynamics and the many nice hours working together in the lab. Also, thank you for helping me improve my understanding of electronics when I first joined the group.

I also want to thank the complete SYNQS group, no only for the interesting discussions about physics but also for the nice moments we spent together: I really enjoyed breakfast on Friday mornings, the BBQs and paper-parties!

Muchas gracias a Leti por comprenderme, acompañarme y el apoyarme, incluso en los momentos de desesperación. Muchas gracias a mis padres José Luis y Gisela por la cercanía en la distancia, por el apoyo y cariño incondicional.

Erklärung

Ich versichere, dass ich diese Arbeit selbstständig verfasst und keine anderen als die angegebenen Quellen und Hilfsmittel benutzt habe.

Heidelberg, den 26.09.2018.

....

Rodrigo F. Rosa-Medina Pimentel